FAKULTÄT FÜR INFORMATIK

DER TECHNISCHEN UNIVERSITÄT MÜNCHEN

Master's Thesis in Biomedical Computing

A General Reconstruction Framework for Constrained Optimisation Problems in Hyperpolarised ^{13}C Metabolic MR Imaging

Elena Nasonova

FAKULTÄT FÜR INFORMATIK

DER TECHNISCHEN UNIVERSITÄT MÜNCHEN

Master's Thesis in Biomedical Computing

A General Reconstruction Framework for Constrained Optimisation Problems in Hyperpolarised ^{13}C Metabolic MR Imaging

Eine allgemeine Rekonstruktionsumgebung für Optimierungsprobleme mit Nebenbedingungen für hyperpolarisierte ^{13}C Bildgebung

Author:	Elena Nasonova
Supervisors:	Prof. Dr. Michael Friebe Prof. Dr. Axel Haase
Advisors:	Dipl.-Phys. Markus Durst Dr. Rolf F. Schulte
Date:	November 11, 2013

I assure the single handed composition of this master's thesis is only supported by declared resources.

The work was done under the guidance of Prof. Dr. Michael Friebe (Chair of Computer Aided Medical Procedures, Technische Universität München, Munich, Germany), Prof. Dr. Axel Haase (Zentralinstitut für Medizintechnik, Munich, Germany) and with support of my advisors: Dr. Rolf F. Schulte and Dipl.-Phys. Markus Durst at the GE Global Research Europe.

München, November 11, 2013 Elena Nasonova

Acknowledgments

This work is a result of the joint collaborative research led by Zentralinstitut für Medizintechnik (IMETUM) and General Electric Global Research Center and I am grateful to the members of the both teams and in particular would like to acknowledge:

My colleagues from GE Global Research, in particular, Markus Durst, Ph.D. candidate and my advisor, who facilitated my learning, was attentive and provided assistance whenever I got stuck in my computations or lacked ideas;

Dr. Rolf F. Schulte for leading our 13C group and being prototype of thoughtful experienced young scientist;

My supevisors Prof. Dr. Michael Friebe and Prof. Dr. Axel Haase for their constructive inspiring feedback.

My studies here would be impossible without support of German Academic Exchange Service (DAAD) and here I acknowledge this organisation and wish it further success and prosperity.

I appreciate support, patience, love from my parents Larissa and Alexandr, my brother Oleg and my boyfriend Ljubo. They are always willing to listen and share both my worries and victories. Thank you.

List of Acronyms

ART Algebraic Reconstruction Technique

AUC Area Under the Curve

AWGN Additive White Gaussian Noise

CG Conjugate Gradient

CSI Chemical Shift Imaging

DNP Dynamic Nuclear Polarisation

FID Free Induction Decay

FOC First Order Correction

FOV Field of View

GRE Gradient Echo

IDEAL Iterative Decomposition of Water and Fat with Echo Asymmetry and the Least-Squares Estimation

LSCSI Least Squares Chemical Shift Imaging

LSQR Least Squares

MRSI Magnetic Resonance Spectroscopic Imaging

NMR Nuclear Magnetic Resonance

NUFFT Non-Uniform Fast Fourier Transform

PET Positron Emission Tomography

PINV Pseudo Inverse

RF Radio Frequency

RMSE Root Mean Square Error

SE Spin Echo

SNR Signal-to-Noise Ratio

SVD Singular Value Decomposition

TE Echo Time

TGV Total Generalised Variation

TR Repetition Time

TSVD Truncated Singular Value Decomposition

TV Total Variation

Abstract

Magnetic resonance spectroscopic imaging with hyperpolarised ^{13}C agents is a novel technique that examines the cellular metabolic reactions and therefore it excels other functional modalities like PET/SPECT, which can quantify the diffusion of a tracer but not metabolism. Besides, MR completely excludes hazards of radioisotope-based imaging procedures. However, the sensitivity of the method is limited by very low Boltzmann polarisation of nuclear spin states in thermal equilibrium. Method of dynamic nuclear polarisation (DNP) allowed for a dramatic increase of signal intensities in MR experiments. Yet there are still a number of unresolved issues. The increased spin population difference is a temporarily induced state and the average T_1 relaxation time for pyruvate is 30 s *in vivo*. Being acquired under the challenging conditions of such rapidly decaying signal, difficult experimental settings and not always valid model assumptions, reconstructed images exhibit low signal-to-noise ratio (SNR) and artifacts. The goal of this work is to enhance the quality of images by means of iterative reconstruction with included *a priori* knowledge in a form of additional constraints and to propose a valid extension to the physical model of signal acquisition.

The first goal is addressed by reformulating the problem as a regularised least-squares problem, where the solution is chosen to be one that minimises a user-defined objective function consisting of a fidelity term, ensuring that the proposed solution is consistent with the measured data, and a regularisation term, usually aiming at penalising noise and non-smooth changes. For the latter, the total generalised variation and anatomical mask proved to yield the most promising results.

To fulfil the second objective, the forward signal model was extended by including the kinetic equations that express the change of metabolite concentration levels over time. By fitting the metabolic time curves to the measured data, the key kinetic parameters, such as forward conversion constants, effective relaxation rates for substrate and downstream metabolites can be estimated, and concentration levels of associated metabolites reliably modelled for each time point.

All methods were implemented first in simulations and then applied to *in vivo* data. Results in respective cases were evaluated by image quality assessment metrics, such as root-mean-square error and signal-to-noise ratio. To minimise the objective function, conjugate gradient method or Levenberg-Marquardt for nonlinear problem from the class of trust region methods were used.

Considering the high number of potential sources of error, such as invalid model assumptions of the current reconstruction, time critical data acquisition, *in vivo* settings and artifacts in metabolic imaging, an improvement in image quality can be achieved by complementing the computational model with additional information (either image- or physics-based) to discard non-plausible solutions. This idea was realised in the thesis and the performance of iterative reconstruction under selected constraints was evaluated.

Contents

Outline of the Thesis

CHAPTER 1: INTRODUCTION

The first chapter serves an introductory purpose in which I would like to familiarise the reader with the topic of work, present an overview of the thesis, state its objectives and outline the problem.

CHAPTER 2: CURRENT STATE OF RESEARCH

The second chapter oulines the fundamental principles of magnetic resonance imaging (MRI) and magnetic resonance spectroscopy (MRS) with a particular focus on spectroscopic imaging with hyperpolarised ^{13}C agents. It also explains the reconstruction algorithm in general and in detail, including specific approaches to model-based reconstruction that have been developed for the last decade. Therefore, the basics and limitations of state of the art reconstruction techniques will be presented and key factors influencing the resulting image quality as well as requirements to the future reconstruction algorithm will be formulated.

CHAPTER 3: METHODS AND EXPERIMENTAL STRATEGY

In the third part of the work, I will present the chosen methods with theoretic framework, describe experimental design and evaluation tools.

CHAPTER 4: RESULTS AND DISCUSSION

The chapter number four contains the results of mathematical simulations for validation of the proposed techniques, experiments with *in vivo* data and custom-built phantom and discussion of the obtained results.

CHAPTER 5: OUTLOOK AND FUTURE WORK

Reflection on the achieved results, future work and summary in the last fifth chapter will conclude the thesis and give the reader a short outlook.

1. Introduction

1.1. Motivation and Objectives

Among all imaging modalities known and actively employed in clinical practice today, magnetic resonance imaging (MRI) is objectively the safest diagnostic tool which produces images of unsurpassed soft tissue contrast. This allows radiologists to detect suspicious lesions and diagnose cancer at its early stage with a high degree of accuracy. Until recent times, MRI could provide information mainly on morphological structure of the tissue based on the observation of water ^{1}H nuclei, thus leaving the question of essential metabolic processes within a tumour open.

Due to the latest advancements in pulse sequence design, recent hardware improvements and study of magnetic susceptibility for different molecules and substances in human body, MRI is rapidly expanding its applicability from pure anatomical towards functional and metabolic imaging. The most exciting and promising technique in this field uses hyperpolarised molecules of ^{13}C pyruvate to study complex biochemical processes in a non-invasive and non-ionising manner. Dynamic nuclear polarisation (DNP) facilitated the imaging by increasing spin polarisation levels to up to 50 %, opposed to only 0.0005 % (5 ppm) for standard non-hyperpolarised samples [19], therefore allowing *in vivo* experiments with hyperpolarised imaging agents. Pyruvate has been chosen as a primary investigated substance in such studies due to its central role in major metabolic and catabolic pathways in the mammalian cells. Conversion of pyruvate to its products: alanine, lactate or carbonate to a large extent depends on the status of the cells [38], [59].

Despite the sound improvements that have been recently achieved in custom-built hardware, robust pulse sequences [94] and incorporation of parallel imaging techniques [22], the quality of metabolite images remains compromised. Optimising SNR and image quality in ^{13}C metabolic imaging is associated with several challenges, including different MR signal time courses for pyruvate and its metabolic products, short acquisition time (caused by decay of the enhanced signal) and requirements that ^{13}C imaging places on the gradient system of the MRI system due to the low gyromagnetic ratio of ^{13}C (4 times lower than ^{1}H) [98].

One way to enhance the achievable SNR and decrease level of artifacts is to advance existing reconstruction methods. The data processing pipeline, from the raw data to the final image, is as important as the acquisition method itself since all operations at this stage of data processing define the spatial resolution and noise properties of the resulting image. Trade-off between these two parameters constitutes the image quality.

This work focuses on a generalised reconstruction framework for hyperpolarised imaging, which treats the image reconstruction as a constrained optimisation problem with incorporation of prior knowledge.

The research in this thesis has been carried out with the following objectives:

- Analysis of existing reconstruction algorithms for MR spectroscopic imaging and identification of its shortcomings as well as other potential sources of errors in hyperpolarised ^{13}C experiments.
- Mathematical simulation of conventional reconstruction algorithm and quantification of occurring error in comparison with ground truth
- Establishing a theoretical framework of iterative regularised reconstruction for ^{13}C metabolic imaging and evaluation of applicable constraints
- Implementation of a chosen optimisation scheme
- Mathematical simulation of iterative reconstruction for linear/nonlinear objective function under selected constraints
- Application of the developed method to *in vivo* data acquired in a phantom and animal experiments.

1.2. Problem Statement

As for the majority of imaging modalities, forward-inverse problems form the foundation of reconstruction also in magnetic resonance imaging.

The inverse fast Fourier transform (FFT) proved to be an effective and well-established image reconstruction method for *k*-space data with full Cartesian sampling. If non-Cartesian sampling is used, then a non-uniform FFT with appropriate density compensation function is employed.

However, there is a growing demand in more accurate methods which would take into consideration multiple physical and model-related effects. To realise this, measurement model must be carefully specified usually as a finite set of governing equations and solution for a given system of equations is estimated by minimising a predefined cost function and must satisfy certain constraints.

Consider, for example, the reconstruction of MR image. In the forward problem (FP) a given input image $\mathbf{x}$ is transformed into an observable output in a form of numerical measurements $\mathbf{b}$ in the *k*-space of raw data by means of applied forward encoding matrix $\mathbf{A}$, which realises Fourier transform from image domain into frequency domain.

$$\text{FP: } \mathbf{Ax} = \mathbf{b} \simeq \mathbf{Ax} - \mathbf{b} = 0 \tag{1.1}$$

Inverse problem (IP) sets the goal to find an approximation $\widehat{\mathbf{x}}$ of the input $\mathbf{x}$ which leads to a particular output $\mathbf{b}$. In other words, to minimise the difference between signals theoretically predicted by model $\mathbf{A}$ and the signals actually acquired by MRI scanner. In practice such approximation is obtained by inversion of the Fourier transform.

$$\text{IP: } \widehat{\mathbf{x}} = \arg\min_{\mathbf{x}}(f(\mathbf{x})) \ \text{ subject to } \ c_i(\mathbf{x}) \geq 0,\ i = 1, ..., n \tag{1.2a}$$

$$\text{Cost function: } f(\mathbf{x}) = \mathbf{Ax} - \mathbf{b} \tag{1.2b}$$

where $f(\mathbf{x})$ is a cost function to be minimised and $c_i(\mathbf{x})$ are constraints that solution $\widehat{\mathbf{x}}$ must satisfy.

Recovery of the true solution **x** from **b** is not possible due to the fact that 1) the forward model $\mathbf{A}$ is not exact and is only an approximation of the imaging process and 2) the recorded data contains noise $\mathbf{b} = \mathbf{b}^* + \mathbf{n}$. Therefore constraints are helpful in order to penalise non-plausible solutions.

The problem can be solved as a series of unconstrained minimisation problems

$$\widehat{\mathbf{x}} = \arg\min_{\mathbf{x}}(f(\mathbf{x}) + \lambda_k \sum_{i \in I} g(c_i(\mathbf{x}))) \tag{1.3}$$

where

$$g(c_i(\mathbf{x})) = \min(0,\ c_i(\mathbf{x}))^2. \tag{1.4}$$

In the above equations, $g(c_i(\mathbf{x}))$ is the "penalty function", sometimes also called "regularisation term", and λ_k are the "penalty coefficients".

The regularisation term plays an important role in the optimisation problem and must be carefully chosen based on the numerous considerations. The character of the regularisation is also very application-specific in a sense that penalties which it creates can significantly vary depending on the desired image appearance, whether the smoothness of the image is of priority, sharpness of edges, preservation of blob-like structures etc.

For MR spectroscopic imaging, one could think about several potentially useful constraints and they have to be investigated in the current work along with their implementation in an appropriate optimisation algorithm. The underlying nature of *in vivo* spectroscopic imaging does not imply the possibility to obtain the ground truth, which adds further complexity to the underlying reconstruction. Due to this reason, extensive simulations will be required to characterise and validate the proposed methods.

2. Current State of Research

2.1. Principles of Magnetic Resonance Imaging (MRI)

This chapter contains an overview of the fundamental principles of nuclear magnetic resonance imaging (NMRI) assuming the basic knowledge of quantum mechanics and particle physics. Magnetic resonance proton imaging makes use of several phenomena: (I) first is that human tissue contains high percentage of water, hence hydrogen (^{1}H) is the most abundant chemical element of the human body; (II) hydrogen nuclei are subject to external magnetic field; (III) frequency of the precession of bulk magnetisation of nuclei depends on spatially varying magnetic strength of the external field; (IV) the conversion from frequency domain into spatial domain is realised through the inverse Fourier transformation. Non-proton ^{13}C MRI, although has the same core principles, imposes additional requirements on hardware, pulse sequences, measurement protocols and reconstruction methods, which will also be outlined in this part of the thesis.

2.1.1. Basic Physical Notations

Spin and Net Magnetisation Vector

Each atomic nucleus rotates around its own axis and possesses a spin that can be understood as some form of angular momentum and in fact is an intrinsic property of all elementary particles. Under gravitational field only, protons are precessing or ”wobbling” at the Larmor frequency creating magnetic moments which cancel out due to Brownian motion and, as a result, no net magnetisation exists. To induce a net magnetisation clinical scanners use a large static magnetic field B_0 applied along z-axis

$$\vec{B}_0(\vec{r}) = B_0(\vec{r})\vec{k} \tag{2.1}$$

where $\vec{k}$ denotes the unit vectors along z-axis and $\vec{r}$ denotes 3D spatial coordinates.

In practice it has the second spatially variant term, which reflects the nonuniformities inevitably presented due to coil design, field strength inhomogeneity or electron distributions in different molecules affecting the local magnetic environment, a so-called chemical shift effect.

$$B_z(\vec{r}, t) = B_0 + \Delta B_0(\vec{r}) \tag{2.2}$$

Exposed to the applied static magnetic field the atomic nuclear spins tend to align with it (Fig. 2.1). Though there is a preference towards parallel alignment, the alignment is, in fact, not perfect. The ratio in populations between two Zeeman energy eigenstates corresponding to parallel and antiparallel orientations of the spins is given by Boltzmann distribution:

$$\frac{N_{-\frac{1}{2}}}{N_{+\frac{1}{2}}} = e^{-\frac{\gamma \hbar B_0}{k_B T}} \tag{2.3}$$

where N is occupation of a given energy level, γ is the gyromagnetic ratio, k_B is the Boltzmann constant, $\hbar$ is the Planck constant, and T is the temperature. The Boltzmann factor depends on the ratio of thermal to magnetic energy and explicitly shows which factors are influential for nuclear magnetic resonance measurement. The spin excess can be increased either by lowering temperature, which is not practical, or by increasing the field strength or directly influencing the population of high and low energy states with one of existing polarisation techniques. All magnetic moments pointing in the direction of static magnetic field sum up to the net magnetisation vector.

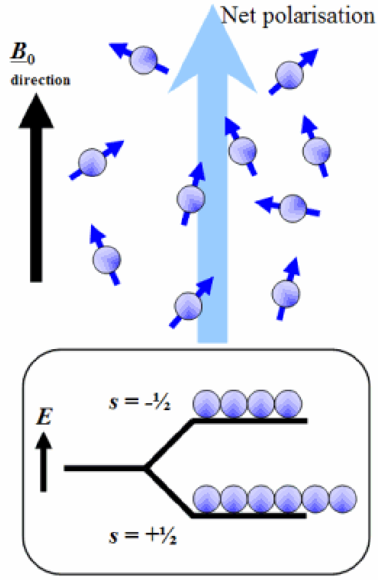

Figure 2.1.: A net magnetisation is produced after an external magnetic field B_0 is applied, which causes a small population bias toward a lower energy state [10]

Resonance and Relaxation

This is the net magnetisation vector, or simply magnetisation, that is manipulated in MRI experiment. During excitation stage magnetisation is tipped away from the equilibrium by applying a radio frequency (RF) pulse, which is orthogonal to the main magnetic field and oscillates at exact frequency of natural precession of nuclear spins. It allows to reorient them so that they have two magnetisation components: longitudinal (M_z) and transverse magnetisation (M_{xy}). The transverse magnetisation starts precessing around the axis of the applied field at the Larmor frequency inducing an oscillating voltage that can be then picked up by a receiver coil [5].

The Larmor frequency is directly proportional to the strength of the external magnetic field with the constant of proportionality being determined by the gyromagnetic ratio γ

[Hz/T] of the atomic species.

$$\omega(\vec{r}, t) = \gamma B_z(\vec{r}, t) \tag{2.4}$$

Hydrogen atoms have the gyromagnetic ratio of approximately 42 MHz per Tesla, for carbon atoms this value is around 10 MHz per Tesla.

When the RF generator is turned off, spins gradually return to their equilibrium state, in which the net magnetisation vector becomes realigned with the static magnetic field. This recovery is characterised by T_1 (time of longitudinal component recovery, also known as spin-lattice relaxation [5]) and T_2 and T_2^* (decay time of transverse component caused by interaction of individual magnetic spins and magnetic field inhomogeneities, respectively) and governed by differential equations known as the Bloch equations for nuclear induction [28]:

$$\begin{gathered}\frac{dM_x(t)}{dt} = \gamma(\mathbf{M}(t) \times \mathbf{B}(t))_x - \frac{M_x(t)}{T_2}, \\ \frac{dM_y(t)}{dt} = \gamma(\mathbf{M}(t) \times \mathbf{B}(t))_y - \frac{M_y(t)}{T_2}, \\ \frac{dM_z(t)}{dt} = \gamma(\mathbf{M}(t) \times \mathbf{B}(t))_z - \frac{M_z(t) - M_0}{T_1}\end{gathered} \tag{2.5}$$

Here γ is the gyromagnetic ratio, $\mathbf{B}(t)$ is the magnetic field experienced by the nuclei and M_0 is the steady state nuclear magnetisation.

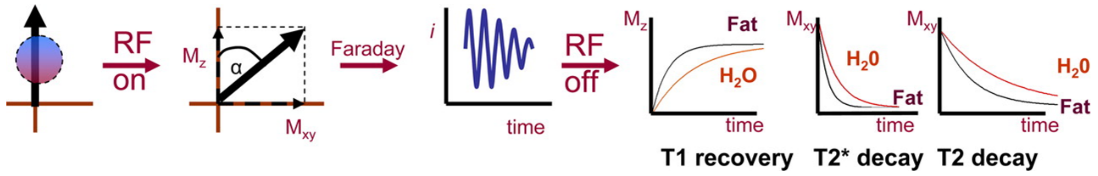

Figure 2.2.: After a RF pulse is applied, the net magnetisation vector is flipped at an angle α, which produces two magnetisation components: longitudinal magnetisation (M_z) and transverse magnetisation (M_{xy}). As the transverse magnetisation precesses around a receiver coil, it induces a current i. When the RF generator is turned off, T_1 recovery and T_2 and T_2^* decay occur [5]

The T_1 and T_2 parameters are tissue-dependent and closely related to echo-time (TE, the time between RF excitation and signal acquisition) and repetition time (TR, the time between subsequent RF excitations). Thus by varying RF pulse sequences and parameter set (TE, TR) it becomes possible to highlight (or suppress) tissue of different types on the final image, in other words - to define the image contrast [61].

2.1.2. Image Formation

Spatial encoding and k-space

How does the MR system know where the signal came from? The idea of spatial encoding or localisation of origin of MR signal in 3D space is to make the magnetic field vary, depending on the position, and for this purpose additional magnets or gradients coils are employed. Three gradient coils correspond to three spatial directions along which we want to measure the signal. It directly follows from the Larmor equation (the precessional frequency of ^{1}H nuclei is changed with variations of the magnetic field strength in a selected region).

Slice encoding, phase encoding and frequency encoding are the names of three gradients which ensure the slightly different spinning behaviour of protons in z, y, x-directions. As a result of such encoding scheme, each of many signals received from any spatial location within an object will have a certain amplitude, phase and frequency, and can be consequently sampled and stored in *k*-space. This term was introduced by Twieg [87] and simply means a two-dimensional matrix of complex numbers, including both phase and frequency information. This raw form of MR image is not very representative in terms of actual diagnostically valid content of image but informative in regards to low and high frequency components of the image: the central part contains information about tissue contrast, while the periphery − information about the spatial resolution.

MR Signal Model

At the readout stage, the applied field strength varies both spatially and temporally and consists of three components:

$$B_z(\vec{r},t) = B_0 + \Delta B_0(\vec{r}) + \vec{G}(t)\cdot\vec{r} \tag{2.6}$$

where $\vec{G}(t) = \vec{G}_x(t)\vec{i} + \vec{G}_y(t)\vec{j} + \vec{G}_z(t)\vec{k}$ is a vector specifying the strength of gradient field.

The Larmor frequency, which we defined before in Eq. 2.4, describes the frequency for a certain point at time in space, the instantaneous frequency at a given location.

$$\omega(\vec{r},t) = \gamma B_z(\vec{r},t) \tag{2.7}$$

Since the net phase is the integral of the instantaneous frequency, spins will accumulate space- and time-varying phase

$$\phi(\vec{r},t) = \int_0^t \gamma\Delta B_0(\vec{r}) + \gamma\vec{G}\cdot\vec{r}\mathrm{d}t \tag{2.8}$$

or equivalently

$$e^{-i\phi(\vec{r},t)} = e^{-i\Delta\omega_0(\vec{r})t}e^{-i2\pi\vec{k}(t)\cdot\vec{r}} \tag{2.9}$$

where $\Delta\omega_0(\vec{r}) \cong \gamma B_0(\vec{r})$ denotes the off-resonance frequency and the *k*-space trajectory is defined as

$$\vec{k}(t) = \frac{1}{2\pi}\int_0^t \gamma\vec{G}(t')\mathrm{d}t' \tag{2.10}$$

The signal acquired in time is a sum of contributions of all individual spins at different positions (having different phase vectors) and represented by integral over the entire volume

$$s(t) = \int \rho(\vec{r})e^{-t/T_2^*(\vec{r})}e^{-i\phi(\vec{r},t)}\mathrm{d}\vec{r} \tag{2.11}$$

where $\rho(\vec{r})$ is the object-dependent local spin density function, T_2^* is a relaxation factor related to exponential decay of transverse magnetisation component due to microscopic variations in the magnetic field.

This a general forward model for the MR signal and in fact a Fourier transformation from real into *k*-space. The signal acquired in *k*-space must be "inverse-Fourier transformed" to bring it back into real space in order to obtain the image.

Pulse Sequences

The concept of traversing the *k*-space is one of the most critical for 2D magnetic resonance image acquisition.

There is versatility of paths to move about in spatial frequency. Since according to Eq. 2.10 the integral over the applied gradient fields derives the trajectory in *k*-space, it is a design of gradient waveforms that in major part defines the outcome of MRI system. Waveforms of the gradients together with associated RF pulses are called pulse sequences and can be depicted in designated diagrams. There are two fundamental types of MR pulse sequences: spin-echo (SE) (Fig. 2.3) and gradient-echo (GRE) (Fig. 2.4), which can be seen as precursors of all others.

While configuring pulse sequences one should always keep in mind how it affects magnetisation, how fast the acquisition is and similar aspects. For example, one of the most pronounced differences between SE and GRE pulse sequences is speed. With only one RF pulse applied in gradient-echo sequence, the echo can be recorded more quickly, resulting in a shorter echo time. Lower flip angles mean that TR can also be shorter since the build-up time for longitudinal magnetisation is reduced. Shorter TR and TE times mean that GRE is preferred for rapid imaging techniques.

k-Space Trajectory

The manner in which *k*-space is filled with data can correspond to Cartesian or non-Cartesian sampling. Although the Cartesian *k*-space trajectories used for signal acquisition are the easiest in terms of applied reconstruction, in this case it is just the inverse FFT, other trajectories such as radial or spiral can be more favourable for certain applications (Fig. 2.5). Later it will be shown that sampling along spirals is used in accelerated imaging applications. The gained benefits come at cost of more complicated reconstruction, from now on requiring *k*-space interpolation schemes [56].

The extent of the *k*-space that is covered determines the image resolution (a larger sampled region gives higher resolution) and the supported field of view (FOV) of the acquired image is defined by the sampling density and must comply with the Nyquist-Shannon theorem that states that sampling frequency satisfies

$$f_s \geq 2f_c \tag{2.12}$$

where f_c is the highest frequency contained in the signal. The violation of this criterion will result in so-called aliasing artifacts, meaning that spatial frequencies cannot be properly resolved any more. The appearance of the aliasing artifacts depends on the character of sampling pattern: for Cartesian trajectory, in case of undersampling, the parts of the image which are outside allowed FOV will get folded back into the maximum FOV. For spiral

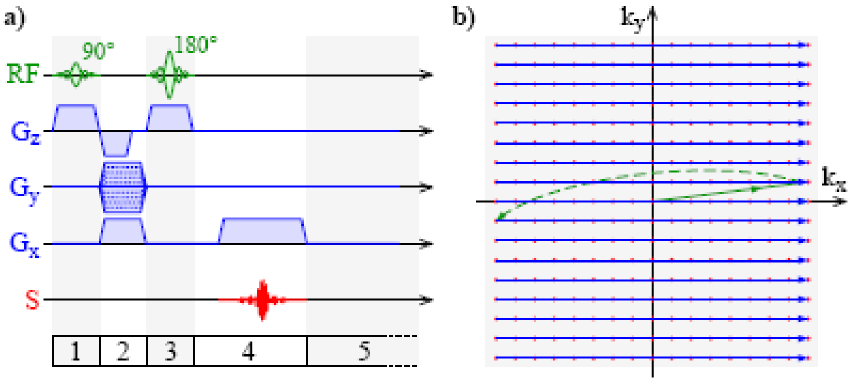

Figure 2.3.: (a) Pulse sequence diagram for one phase encoding step of a spin-echo sequence. The slice is excited in the step 1, the second RF pulse in period 3 that rotates magnetisation at 180° in the xy-plane forms echo in period 4. The 5 channels shown are the transmitted radio frequency (RF), the x-, y- and z-gradients (Gx, Gy, Gz), and the received signal (S) channels. (b) The *k*-space trajectory of the sequence. The signal is acquired along the blue lines at the positions indicated by red dots. The solid green line represents the *k*-space shift that occurs during period 2 and the dashed line shows the effect of the 180° pulse in period 3 [69].

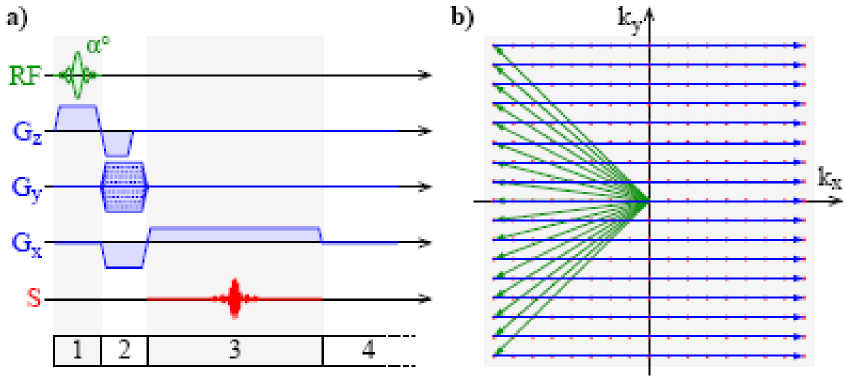

Figure 2.4.: (a) Pulse sequence diagram for one phase encoding step of a gradient echo sequence. The slice is excited during period 1, and the gradients in periods 2 and 3 cause an echo to be formed in period 3. The 5 channels shown are the transmitted radio frequency (RF), the x-, y- and z-gradients (Gx, Gy, Gz), and the received signal (S) channels. (b) The *k*-space trajectory of the sequence. The signal is acquired along the blue lines at the positions indicated by red dots. The *k*-space shift due to the gradients in period 2 is shown in green [69].

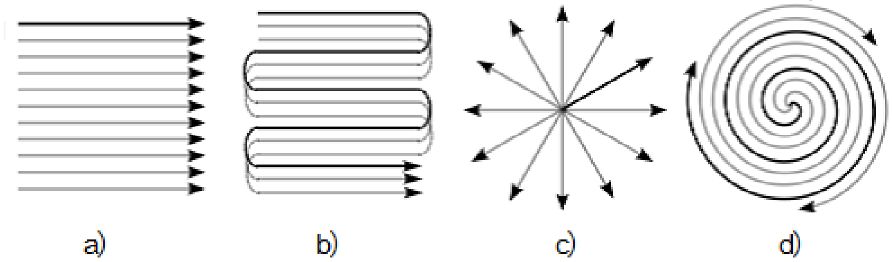

Figure 2.5.: Trajectory commonly used to traverse *k*-space. (a) Cartesian 2D. (b) Cartesian echo-planar. (c) Radial. (d) Spiral [56]

trajectory, some swirl formation can occur and image quality with radial *k*-space sampling can be degraded by characteristic spikes. For a given resolution and FOV a certain number of discrete samples needs to be measured in order to be able to reconstruct the image without artifacts.

2.1.3. Magnetic Resonance Spectroscopy

The principles of nuclear magnetic resonance allows one to explore physical and chemical properties of many atoms such as carbon (^{13}C), nitrogen 8^{15}N), fluorine (^{19}F), sodium (^{23}Na), phosphorus (^{31}P), hydrogen (^{1}H) and molecules, for which these atoms form building blocks. Of particular clinical importance is the investigation of organic molecules containing carbon, which is essential for development of biological organisms. Magnetic resonance spectroscopy (MRS) complements MRI in a way that in addition to structural information it provides biochemical data about metabolic changes in tissues. Therefore, it reflects functional biological processes on the molecular level rather than exclusively distribution of water and fat. MRS implies usage of 1D signals to express the concentrations of metabolites and in order to obtain 2D distribution of corresponding metabolites, longer acquisition and processing times are required. This is known as Magnetic Resonance Spectroscopic Imaging (MRSI) or a two-dimensional Chemical Shift Imaging (CSI).

Chemical Shift (CS) Effect

As was mentioned before in Eq. 2.2, a perfectly homogeneous magnetic field is a rather idealistic notation. In practice the individual chemical environment of the nuclei leads to slight disturbances of the magnetic field and thereby also their observed Larmor frequencies. It happens because electrons themselves produce a small local magnetic field that opposes the external magnetic field and so electrons possess diamagnetic properties and induce ”shielding” effect on the nucleus.

$$B_{local} = B_0 - \delta B \tag{2.13}$$

Resulting Larmor frequency

$$\omega_0 = \gamma B_0 = \gamma(1-\delta)B_0 \Rightarrow \Delta\omega = \gamma\delta B_0 \tag{2.14}$$

where $\Delta\omega$, chemical shift, depends on the applied magnetic field, gyromagnetic ratio γ and $\delta = \frac{\Delta\omega}{\omega_0}$ depends on nucleus, electron density, electronegativity of neighbouring groups etc.

This phenomenon, when for a given molecule a spectrum of resonance frequencies can be observed depending on its chemical environment, is known as chemical shift (CS) effect and constitutes the basis of NMR spectroscopy [8]. It allows the observation and visualisation (peak position along the x-axis) of a spectrum of such chemical shift frequencies for a given molecule and subsequent comparison of observed spectra with known ("fingerprint") spectra, for instance, to probe the tumour behaviour. This is possible due to the fact that each metabolite has a different peak, which appears in the spectrum at a known frequency offset. It is typically expressed in Hz or parts per million (ppm) relative to the standard reference substance (tetramethylsilane (TMS)).

It is preferable to have a relatively sparse spectrum in order to be able to resolve the distinct metabolic peaks, especially in imaging, where overlapping chemical shift frequencies may cause pronounced artifacts. For this, high-strength magnetic fields are desirable to increase the signal-to-noise ratio and spread the resonance peaks over a wider frequency range.

Hyperpolarised MR Imaging

MR spectroscopy features intrinsically low signal intensities due to small difference in the population of nuclei spins in a magnetic field. In proton clinical MR imaging this is compensated by high concentrations of water in the human body but precludes monitoring of other nuclei such as carbon (^{13}C), fluorine (^{19}F) or phosphorus (^{31}P) whose natural concentrations are significantly lower.

Currently several techniques of enhancing the spin-polarisation difference of populations of nuclei are being investigated. A sufficiently high SNR in non-proton NMR can be achieved by a technique called hyperpolarisation, which essentially means an artificially temporarily induced state in which the degree of alignment of the spins of atomic nuclei is increased. There are several routes to hyperpolarisation including dynamic nuclear polarisation (DNP), para-hydrogen induced polarisation (PHIP), optical pumping and several others [75].

Among them the DNP technique is of exceptional interest for metabolic studies. By transferring the polarisation from electrons to the molecules of carbon it achieves polarisation levels of $> 20\,\%$, which is equivalent to $> 10{,}000$-fold signal increase [2]. A more detailed process of DNP will be described in the experimental part but for now it is worth saying that it involves mixing the source of free electrons with MR active sample and irradiation it with microwaves in a high magnetic field (3 T) at low temperatures (1 K).

Although DNP technique can be applied to virtually any MR active nucleus, the most successful studies were conducted with the molecules of [1-13C] pyruvate. These are frequently chosen because they demonstrate high polarisation levels (up to 50 % vs. 0.0005 % of the normal polarisation levels), retain hyperpolarisation for a time span sufficient for measurement (time constant of signal decay is about 30 s) and convert fast enough to provide dynamic metabolic response. Additionally, ^{13}C pyruvate and its downstream metabolites: [1-^{13}C]lactate, [1-^{13}C]alanine and [^{13}C]bicarbonate have a relatively sparse spectrum (Fig. 2.6), which makes them well-suited for chemical based imaging methods such as those often used for water-fat separation.

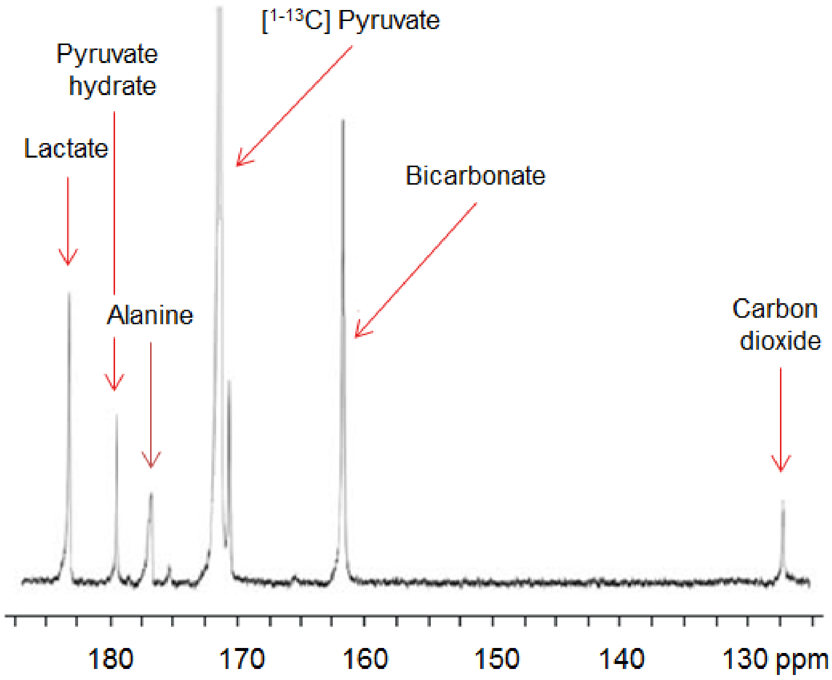

Figure 2.6.: A graphic representation of the spectrum produced by ^{13}C labelled pyruvate and its metabolites (chemical shift frequencies are expressed in ppm) [23]

Clinical Value of ^{13}C Pyruvate as Imaging Agent

A molecule to be used in hyperpolarised studies has to satisfy following criteria:

- Long nuclear relaxation times
- High number of active spins
- Biocompatibility
- Biological interest (molecular imaging)

Carbon is nominally the second most abundant chemical element in the human body after hydrogen, however presented only with insignificant 1.1 %, which results in a very low NMR sensitivity (signal intensity) at the thermal equilibrium. Dynamic nuclear polarisation allows to drastically increase the polarisation level (up to 30 %) [75] which opens up numerous perspectives for *in vivo* metabolic imaging, particularly for oncology applications.

By injection of hyperpolarised [1-13C]pyruvate, it is possible to study the major generating metabolic and catabolic pathways in mammalian cells, since pyruvate plays a central role in metabolic reactions leading to energy production and formation of downstream metabolites: lactate, alanine and carbon dioxide (Fig. 2.7).

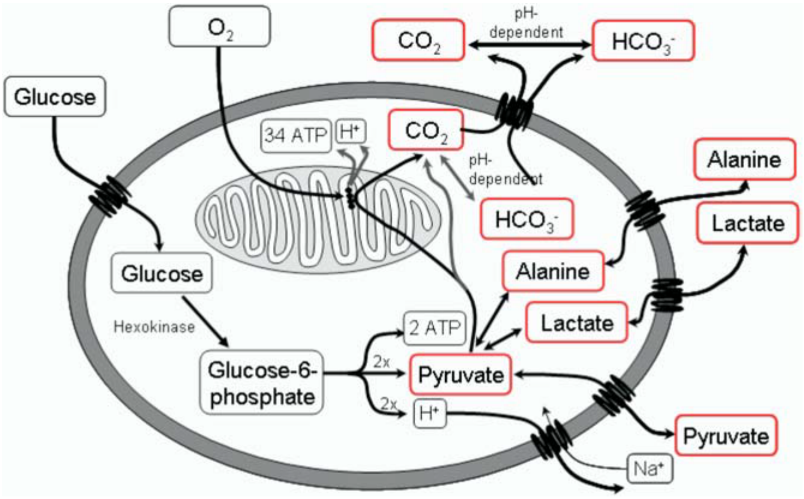

Figure 2.7.: The metabolic pathways in the cells of endogenous glucose and endogenous/injected pyruvate. The metabolic products that can be imaged using the hyperpolarised [1-13C]pyruvate technique are shown in red [37]

The resonance frequencies of the metabolites of interest can be efficiently separated from the pyruvate substrate allowing observation of all products containing the ^{13}C atom in time-resolved manner. The relative concentrations of the produced metabolites will represent the actual condition of the cells and they are usually affected by viability parameters such as pH.

The exceptional diagnostic value of metabolic maps of pyruvate and its downstream metabolites for diagnosis and assessment of cardiovascular disease, characterisation of brain tumours, and the wide range of neurological applications has been already proven in numerous studies [20], [75], [38]. In all cases it was possible to distinguish the cancerous cells from healthy ones by injecting [1-13C]pyruvate and observing its metabolic products. The elevated production of lactate in the process of anaerobic glycolysis is a fundamental property of cancer cells and the most well-observed sign of their altered metabolism. It has a name of Warburg effect [38]. This change in metabolic pattern, compared to normal cells, may be used for detection and staging of tumours.

Another promising directions, enabled by hyperpolarised tracers, include measurements of intracellular and extracellular pH [32]; coronary angiography with infused [1-13C]urea; myocardial perfusion and viability assessment [36]; detection of cell death by necrosis with [1,4-C13] fumarate [33].

2.1.4. Adaptation of Imaging Strategies for Hyperpolarised ^{13}C MR Imaging

Magnetic resonance imaging with hyperpolarised ^{13}C puts certain requirements on data acquisition protocol due to the different resonance frequency of carbon nuclei, inherently low sensitivity, rapid polarisation decay. It makes impossible to use the same methods as for proton imaging and also leaves impact on the spatial/temporal resolution of the resulting images and achievable signal-to-noise ratio (SNR).

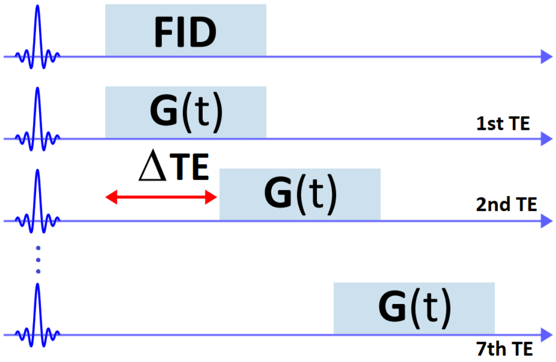

Figure 2.8.: Scheme of IDEAL spiral CSI encoding module: after RF pulse follows a single-shot spiral imaging module, each shifted relative to the previous in terms of echo time. A FID acquisition, performed at the beginning, provides the spectral prior knowledge for reconstruction [21]

Fast Imaging Pulse Sequences

Due to the rapid decay of the temporarily enhanced signal and dynamic fast changing metabolic behaviour, the acquisition times must be preferably short and the sampling trajectory must have a sufficient extent in the *k*-space.

The gold-standard method for imaging the ^{13}C isotopes uses the free induction decay echo-planar spectroscopic imaging (FID EP CSI), which requires the acquisition of large amount of data in order to be able to resolve the spectral peaks. A Fourier transformation is then performed to obtain the spectrum. Since it uses conventional phase encoding for the N spatial dimensions, the sequence is far too slow for hyperpolarised application because $N_x \times N_y \times N_z$ phase encode steps need to be performed with separate excitations.

Recently another method, known as IDEAL (iterative decomposition of water and fat with echo asymmetry and least-squares estimation), has been employed for efficient separation of ^{13}C species [94]. The IDEAL method uses pulse sequences with spiral *k*-space sampling to acquire multiple images at different echo-times (TE) and an iterative linear least-squares approach to separate signal components [72]. The main advantage is that, if the frequencies of imaged species are known in advance, the number of echo-time repetitions can be significantly reduced. This prior information shortens the scan time and allows to devote more repetitions to increase resolution.

Spiral sampling is beneficiary for hyperpolarised ^{13}C application because it allows to fill the *k*-space very fast and offers two orders of magnitude decrease in acquisition times compared to the conventionalecho-planar CSI [31]. This is accomplished by traversing the *k*-space after application of a single RF pulse (a single ”shot”) simultaneously within one TR, rather than using many RF pulses and relaxation periods (Fig. 2.9). Trajectory traversed in the *k*-space in this case is given by:

$$\vec{k}(t) = \begin{bmatrix} r(t)cos(iq(t)) \\ r(t)sin(iq(t)) \\ 0 \end{bmatrix} \tag{2.15}$$

where $r(t)$ is radius of the spiral and $q(t)$ specifies the angular motion.

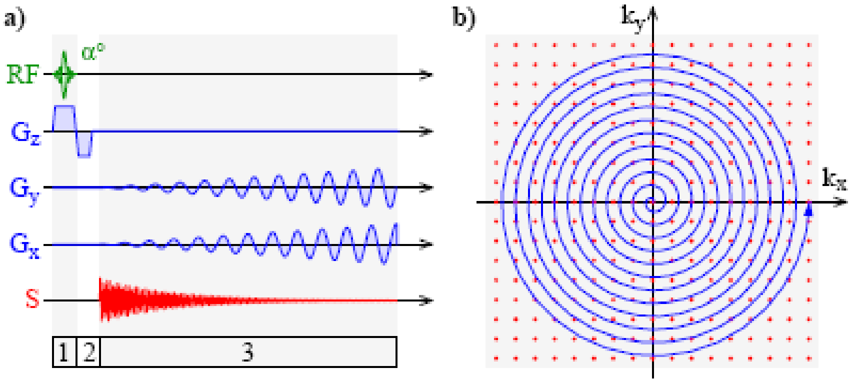

Figure 2.9.: (a) Pulse sequence diagram for a spiral imaging sequence, and (b) *k*-space trajectory. The signal is received in the presence of oscillatory x and y gradients such that *k*-space is traversed in a spiral fashion. Data acquired on the spiral must be interpolated onto a regular grid of points (red dots) [69].

Due to a phase accumulation during the data acquisition in the presence of the spiral readout gradients, a linear phase correction has to be performed to avoid image-blurring artifacts.

Signal-to-Noise Ratio Considerations

SNR of the scanner operating at 1 T can be expressed [37]

$$SNR \propto \gamma P c = \gamma^2 B_0 c \tag{2.16}$$

where γ is the gyromagnetic ratio of the nuclei in question, P is the polarisation and c is the concentration of the nuclei. This expression shows that when polarisation originates from the external source, the achievable SNR values will no longer depend on the main magnetic field of the used imaging system.

On the one hand, it allows to perform imaging at magnetic field strengths, lower than ones typically used in the clinical routine. On the other hand, in order to create images within short T_1, the highest available gradient amplitude must be applied. Such combination of low magnetic field with high gradient amplitudes results in gradient nonlinear components, sometimes named the Maxwell terms, and causing image artifacts. One can numerically compute the phase evolution induced by concomitant gradient field of the read gradient.

$$\phi = t_{samp} \gamma \frac{G_x^2}{2B_0} d^2 \tag{2.17}$$

where t_{samp} is the sampling time, G_x is the readout gradient (along the x-direction), and d is the distance in the z-direction from the isocentre of the scanner. This indicates that hyperpolarised ^{13}C imaging may not be performed in low magnetic field if high gradient amplitudes are required (in fast imaging protocol) [37].

Other common image artifact arises due to a limited *k*-space coverage necessitated by low SNR of metabolite signal and limited scanning time. This is known as Gibbs phenomenon and manifests in form of characteristic circles/ripples or ring-like structures on the image surface. These are caused by a truncation of the data in *k*-space (sampled only to a certain extent) which is equal to the multiplication with a window function ($\mathrm{sinc}(x) = \frac{\sin(x)}{x}$). Multiplying the time domain by a rectangular pulse results in the signal in frequency domain being convolved with a sinc function [81] which yields an oscillating output, particularly pronounced in the image domain around areas with a large signal difference.

Applying filtering to the data at the post-processing step reduces the artifact level to a certain extent but does not eliminate it completely. The most commonly used apodisation functions are Gaussian or Hamming filters. A generalised Hamming filter for the spiral trajectory is given by:

$$f_{Hamming}(\vec{k}_i) = \alpha - (1-\alpha)cos(2\pi(0.5 - \left|\vec{k}_i\right|)) \tag{2.18}$$

where the parameter $\alpha \in [0.5, 1]$ defines the degree of apodisation and $\vec{k}_i$ are the *k*-space points on the spiral trajectory, normalised to 0.5. The disadvantage of this approach is the general smoothing of the spatial domain. Apodisation reduces side-lobes of the point spread function resulting from the truncation of *k*-space. At the same time the main lobe of the point spread function is broadened.

A more drastic reduction of truncation artifacts can be achieved through the variable coverage of *k*-space during the data acquisition [45]. The idea is to sample the central part (low frequency) *k*-space using the highest achievable density for the maximum possible SNR. The rest of the frequency domain is sampled with the minimum sampling density required by the Nyquist criterion [77]. There are more techniques, which have their goal reduction of the truncation artifacts and enhancement of the quality of spectroscopic images, which will be discussed later.

Customised Hardware

In order to perform imaging experiments, using a hyperpolarised ^{13}C substance, MRI scanner system has to be properly adopted for this purpose. First requirement is that the MRI scanner needs to be able to send and receive on the carbon resonance frequency. For instance, at 1.5 T, the proton resonance frequency is 60 MHz while the ^{13}C resonance frequency is 15 MHz. Extension of the system for multiple nuclei is needed in order to operate in a suitable for hyperpolarised imaging frequency range [37].

Dedicated RF coils are needed and there are certain demands that ^{13}C imaging places on the gradient system of the MRI scanner owing to the low gyromagnetic ratio of ^{13}C (4 times lower than 1H).

The encoding procedure differs due to the low gyromagnetic ratio as well. The contribution from a given gradient strength is only around $1/4$ compared to the case when proton imaging is performed. Therefore, echo times (TE) and repetition time (TR) may be prolonged in order to obtain an image of comparable resolution.

2.2. Model-Based Reconstruction in Metabolic MRI

It was shown in Section 2.1.2 that, according to the MR signal model, acquired images are reconstructed from the raw measurements by inverse 2D or 3D fast Fourier transform (FFT). However, in more complicated cases of chemical shift imaging, when more than one metabolic species are examined or when the sampling pattern is non-Cartesian, or physical effects such as field nonlinearities must be accounted for, a simple iFFT is not sufficient any longer. Estimating and compensating for physical effects with consideration of relevant prior information has become the central part of many scientific studies in MR field [1], [7], [84]. In the current chapter, a concept of model-based reconstruction will be explained in application to MR and MRS imaging. The steps comprising the processes of data acquisition and reconstruction will be formulated in mathematical notations and several approaches, proposed for more efficient reconstruction of MR images, will be discussed.

2.2.1. Forward and Inverse Problem in Image Reconstruction

For the sake of completeness the general forward signal model formulated in Section 2.1.2 reads

$$s(t) = \int \rho(\vec{r}) e^{-t/T_2^*(\vec{r})} e^{-i\phi(\vec{r},t)} \mathrm{d}\vec{r} \tag{2.19}$$

where $\rho(\vec{r})$ denotes the object's transverse magnetisation, proportional to the local spin density, and the goal of MRI is to form the image of $\rho(\vec{r})$.

In practice multiple signals are recorded, one for each excitation/readout pair (for each "shot"). In result, the recorded measurements consist of n typically noisy samples of the MR signal

$$y_i = s(t_i) + \varepsilon_i, i = 1, ..., n \tag{2.20}$$

Sampling vector t_i usually has equal spacing and often there are one or more time values where the signal is particularly strong due to alignment of the magnetisationâs phases; these values are called echo times. The measurement errors ε_i are well modelled by complex, zero-mean Gaussian noise [24].

The fundamental problem in MRI is to obtain (∼reconstruct) unknown quantity $\rho(\vec{r})$ provided vector of measurements $\mathbf{y} = (y_1, ..., y_n)$ and the signal model (see Eq. 2.19) are given.

This is an ill-posed problem because the given measurements **y** are discrete whereas the object $\rho(\vec{r})$ is a continuous function. It means the violation at least one of definitions of a "well-posed" problem, namely that the solution depends continuously on **s**. Using a Finite Series Expansion method [13] it is possible to simplify the forward problem to a discrete form

$$s(t_i) = \sum_{j=1}^{N} a_{ij} \rho_j \tag{2.21}$$

where N is equal to the number of voxels (pixels) in the image and elements a_{ij} of the system matrix $\mathbf{A}$ are given by

$$a_{ij} = \int b(\vec{r} - \vec{r}_j) e^{-t_i/T_2^*} e^{-i\phi(\vec{r},t)} \mathrm{d}\vec{r} \tag{2.22}$$

where $b(\cdot)$ denotes the object basis functions, which are often chosen to be highly localised (centers of voxels) and then coefficients of the system matrix are simply

$$a_{ij} = e^{-t_i/T_2^*(\vec{r}_j)} e^{-i\phi(\vec{r}_j t_i)} \tag{2.23}$$

Stacking up all measurements and defining system encoding matrix of size $n \times N$, the final matrix-vector form of the signal model yields

$$\mathbf{y} = \mathbf{A}\rho + \varepsilon \tag{2.24}$$

A natural approach to the solution for ρ is to find the estimate by minimising the least-squares cost function:

$$\widehat{\rho} = \arg\min_{\rho} \Psi(\rho), \Psi(\rho) = \|\mathbf{y} - \mathbf{A}\rho\|_2^2 + \alpha \left\|\mathrm{R}(\rho)\right\|_2^2 \tag{2.25}$$

From this point and further on we call expressions in Eq. 2.24 and 2.25 forward and inverse problems in image reconstruction, respectively, and discuss solutions for the latter case of the inverse problem. Let have a look how this general reconstruction framework reads in a specific case of chemical shift imaging.

2.2.2. Case Study: Chemical Shift Imaging of ^{13}C-labeled Compounds

The forward transformation can be formulated as a two-step encoding process [94].

1. The data in spatial domain and frequency domain (*k*-space) are related through the Fourier transform. Non-Cartesian spiral sampling of *k*-space is used since such trajectories are fast to realise and the entire *k*-space can be acquired during a single acquisition or single "shot". The time diagram of the sequence, which realises such encoding, can be found in Section 2.1.4.

$$\xi_q(\vec{k}_n) = \sum_{p=1}^{N} x_q(\vec{r}_p) e^{i2\pi \vec{k}_n \vec{r}_p} \tag{2.26}$$

   Here $\vec{r}_p$ are 3D object space coordinates for a discrete voxel, $\vec{k}_n$ is the n^{th} sample of the *k*-space trajectory, $x_q(\vec{r}_p)$ and $\xi_q(\vec{k}_n)$ are concentrations of q^{th} metabolite in spatial and frequency domain, respectively. This step is often referred as *spatial* signal encoding.

2. Later acquisitions all have a slight relative shift in echo time TE_m, so the time after excitation is $TE_m + t_n$. The data from N metabolites with *a priori* known chemical shift frequencies Δf_q gets mixed in this way into a single measurement recorded for

a particular location in frequency domain and at particular time point. The step is commonly referred as *spectral* signal encoding.

$$s_{m,n} = \sum_{q=1}^{N} \xi_q(\vec{k}_n) e^{i2\pi\Delta f_q TE_m} e^{i2\pi\Delta f_q t_n} \tag{2.27}$$

The task now is to resolve these metabolites.

Both operations can be included into one encoding operator. Then in a matrix form the forward problem reads

$$\mathbf{s} = \mathbf{A} \cdot \mathbf{x} \tag{2.28}$$

where **A** comprises both operations of spatial and spectral encoding and has the components corresponding to different echo times, which are arranged in blocks along the rows, and metabolic substances – in blocks arranged along the columns

$$\mathbf{A} = \begin{bmatrix} e^{i2\pi\vec{k}_1\vec{r}_1} e^{i2\pi\Delta f_1 t_1} & \dots & e^{i2\pi\vec{k}_1\vec{r}_p} e^{i2\pi\Delta f_1 t_1} & e^{i2\pi\vec{k}_1\vec{r}_p} e^{i2\pi\Delta f_2 t_1} & \dots \\ \vdots & & \ddots & \vdots & \\ e^{i2\pi\vec{k}_L\vec{r}_p} e^{i2\pi\Delta f_1 t_L} & & & & \\ e^{i2\pi\vec{k}_1\vec{r}_p} e^{i2\pi\Delta f_1 (t_1+\Delta t_1)} & \dots & \dots & \dots & \\ \vdots & & & & \end{bmatrix} \tag{2.29}$$

$$\mathbf{s} = \begin{bmatrix} s_{11} \\ \vdots \\ s_{1L} \\ s_{21} \\ \vdots \\ s_{ML} \end{bmatrix} \tag{2.30}$$

$$\mathbf{x} = \begin{bmatrix} x_{11} \\ \vdots \\ x_{1P} \\ x_{21} \\ \vdots \\ x_{NP} \end{bmatrix} \tag{2.31}$$

where M is the number of echo time shifts, L is number of sampling points of the k-space trajectory, N is the number of metabolites of interest, P is the number of voxels (pixels) of the acquired 2D/3D distribution.

The inverse problem is solved in the least-squares sense, in practice, by direct unregularised inversion of the encoding system matrix.

$$\hat{\mathbf{x}} = arg\min_{\mathbf{x}} \|\mathbf{Ax\text{-}s}\|_2^2 \tag{2.32}$$

Given a matrix $\mathbf{A}$ $(M \cdot L \times N \cdot P)$, vectors of measurements $\mathbf{s}$ $(M \cdot L \times 1)$ and unknowns $\mathbf{x}$ $(N \cdot P \times 1)$, where $M \cdot L > N \cdot P$, we have an ill-conditioned overdetermined system. There are three different algorithms for computing the least squares minimum.

1. Normal equations (computationally cheap, less accurate)
   Solve the system of normal equations

   $$\mathbf{A}^{\mathsf{T}}\mathbf{Ax} = \mathbf{A}^{\mathsf{T}}\mathbf{s} \tag{2.33}$$

   by computing Moore−Penrose pseudoinverse $\mathbf{A}^{+}$

   $$\mathbf{x} = \mathbf{A}^{+}\mathbf{s},\ \mathbf{A}^{+} = (\mathbf{A}^{\mathsf{T}}\mathbf{A})^{-1}\mathbf{A}^{\mathsf{T}} \tag{2.34}$$

2. QR decomposition (requires modified version for non-square matrices) Given $\mathbf{A}_{(m \cdot n)}$, let its $\mathbf{QR}$ decomposition be given as $\mathbf{A} = \mathbf{QR}$, where $\mathbf{Q}_{(m \cdot n)}$ is an orthonormal matrix and $\mathbf{R}_{(n \cdot n)}$ is upper triangular. The solution reads

   $$\mathbf{x} = \mathbf{R}^{-1}\mathbf{Q}^{\mathsf{T}}\mathbf{s} \tag{2.35}$$

3. SVD (expensive, more reliable) Given the singular value decomposition (SVD) of a matrix $\mathbf{A}$

   $$\mathbf{A} = \mathbf{U}\Sigma\mathbf{V}^{\mathsf{T}} = \sum_{i=1}^{n} u_i \sigma_i \mathrm{v}_i^{\mathsf{T}} \tag{2.36}$$

   where $\mathbf{U} = (u_1, ..., u_n)$, $\mathbf{V} = (\mathrm{v}_1, ..., \mathrm{v}_n)$ have orthogonal columns and $\Sigma = \mathrm{diag}(\sigma_1, ..., \sigma_n)$ is a diagonal matrix of singular values of $\mathbf{A}$ with $\sigma_1 \geqslant ... \geqslant \sigma_n \geqslant 0$. The minimal solution corresponds to

   $$\mathbf{x} = \mathbf{V}\Sigma^{-1}\mathbf{U}^{\mathsf{T}}\mathbf{s} \tag{2.37}$$

   To further improve the performance, the truncated SVD can be used as a method of regularisation [66], [29]. The idea behind is to cut off the components corresponding to small singular values, which in their turn correspond to noisy SVD components and cause errors in the solution. The truncated SVD solution reads

   $$\mathbf{x}_k = \sum_{i=1}^{k} \frac{\mathrm{v}_i \mathbf{u}_i^{\mathsf{T}}\mathbf{s}}{\sigma_i} \tag{2.38}$$

   where k is a truncation parameter such that $\frac{\sigma_1}{\sigma_k} \ll \frac{\sigma_1}{\sigma_n}$.

The first algorithm is the fastest and the least accurate among the three. On the other hand, SVD is the slowest and the most accurate one. Performance of these algorithms with associated time costs is illustrated in Fig. 2.10.

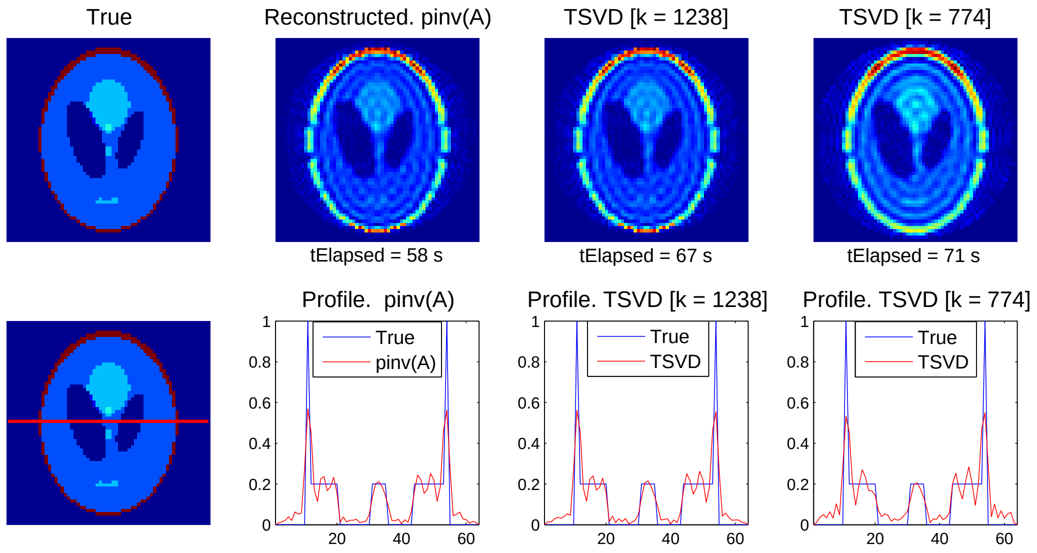

Figure 2.10.: Reconstruction of $[64 \times 64]$ pixels Shepp-Logan phantom using the normal equations; truncated SVD with $k = 1238$, which corresponds to 60 % of lowest singular values discarded; truncated SVD with $k = 774$, which corresponds to 75 % of lowest singular values discarded

The problems that might arise are due to the fact that elements of the matrix $\mathbf{A}$ can be complicated, depending on the model effects included into signal acquisition scheme, and the matrix size is too big to store it explicitly in iterative algorithm, where matrix-vector multiplications by $\mathbf{A}$ and its transpose are required [24]. To make these operations computationally less expensive, the problems of chemical shift separation and spatial reconstruction can be separated.

Least Squares Chemical Shift Separation

The acquired raw data has dimensionality $[M \times L]$, where M is the number of acquisitions and L specifies the number of sampling points, meaning that underlying information about distinct metabolites has to be separated. Transformation from several echoes to several frequencies is done with method known as least-squares chemical shift imaging (LSCSI) separation, well adapted from the decomposition of water and fat technique [73].

The signal, that we measure at time $\tau_{m,n} = TE_m + t_n$ after excitation with relative echo-time shift TE_m $(m = 1, ..., M)$, is combination of contributions from pyruvate and its products: lactate, alanine etc. and thus can be written

$$s_{m,n} = \xi_1(\vec{k}_n)e^{i2\pi\Delta f_1 \tau_{m,n}} + ... + \xi_N(\vec{k}_n)e^{i2\pi\Delta f_N \tau_{m,n}} \tag{2.39}$$

where $\xi_1, ..\xi_N$ express metabolite distributions in frequency domain and resonant frequencies of species $\Delta f_1, ..., \Delta f_N$ are supposed to be known in advance from a slice-selective FID acquisition at the beginning of each imaging module.

The formulation in the matrix form reads

$$\mathbf{s} = \mathbf{C}\xi \tag{2.40}$$

$$\xi = [\xi_1 \; \xi_2 \; ...\xi_N]^{\mathsf{T}}, \mathbf{C} = \begin{bmatrix} e^{i2\pi\Delta f_1 \tau_{1,n}} & ... & e^{i2\pi\Delta f_N \tau_{1,n}} \\ e^{i2\pi\Delta f_1 \tau_{2,n}} & ... & e^{i2\pi\Delta f_M \tau_{2,n}} \\ \vdots & \ddots & \\ e^{i2\pi\Delta f_1 \tau_{M,n}} & ... & e^{i2\pi\Delta f_N \tau_{M,n}} \end{bmatrix}. \tag{2.41}$$

This system of equations can be solved with one of previously described methods, for instance, using the Moore-Penrose pseudoinverse and the solution for distinct metabolite distributions in *k*-space reads

$$\xi = (\mathbf{C}^{\mathsf{T}}\mathbf{C})^{-1}\mathbf{C}^{\mathsf{T}}\mathbf{s} \tag{2.42}$$

It should be noted that at least $M \geqslant N$ acquisitions with different echo times are required in order to solve the system for N species. The main disadvantage of such overdetermination is inconsistency with the time behaviour of metabolites. The encoding matrix **C** in its current form does not account for the change in magnetisation levels between single excitations and approximates it with a constant function. This can become a source of errors and inaccuracies in the final reconstructed image.

There are other limitations of this method, such as necessitated knowledge of resonant frequencies and required optimisation of echo spacing. Uniformly spaced echoes are by far well-suited for most applications, but non-uniform TE increments can improve the noise performance [72].

Non-Uniform Fast Fourier Transformation

After separation with LSCSI method, the *k*-space data of individual metabolites has to be Fourier transformed into the image domain. This can be accomplished by, analogous to the previous step, inversion of the spatial encoding matrix

$$\mathbf{x} = (\mathbf{B}^{\mathsf{T}}\mathbf{B})^{-1}\mathbf{B}^{\mathsf{T}}\xi \tag{2.43}$$

$$\mathbf{x} = [x_1 ... x_N]^{\mathsf{T}}, \; \xi = [\xi_1 ... \xi_N]^T, \mathbf{B} = \begin{bmatrix} e^{i2\pi\vec{k}_1\vec{r}_1} & ... & e^{i2\pi\vec{k}_1\vec{r}_P} \\ e^{i2\pi\vec{k}_2\vec{r}_1} & ... & e^{i2\pi\vec{k}_2\vec{r}_P} \\ \vdots & \ddots & \\ e^{i2\pi\vec{k}_L\vec{r}_1} & ... & e^{i2\pi\vec{k}_L\vec{r}_P} \end{bmatrix} \tag{2.44}$$

More often a faster method of non-uniform fast Fourier transform (NUFFT), proposed by Jeffrey Fessler with co-authours [27], is used, which is an efficient algorithm for reconstruction of non-Cartesian data by first (I) resampling the data to a Cartesian grid and then (II) applying inverse 2D DFT.

An effective approach to interpolate the Cartesian data points from the non-Cartesian samples involves convolution of the data with a special kernel such as a Kaiser-Bessel (KB) interpolation kernel [26]. Fig. 2.11 illustrates an example of non-uniformly distributed radial samples and a gridding convolution kernel.

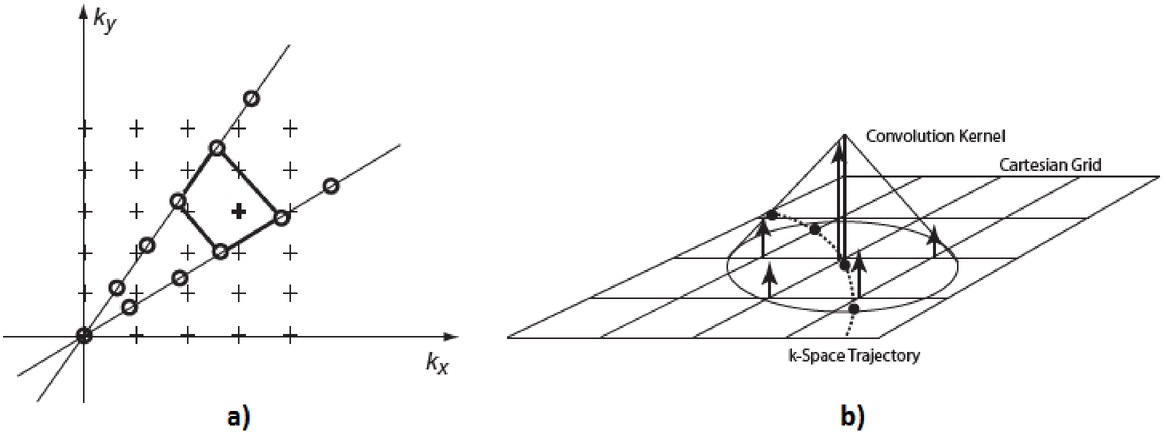

Figure 2.11.: (a) With radial k-space sampling the data lies on the spokes and has to be interpolated to the Cartesian grid. (b) Gridding kernel convolution and re-sampling [26]

The idea behind the kernel is to extend to the neighbouring pixels, so that after convolution with the data point, which lies on some k-space trajectory, the contribution of this point would be added to the surrounding grid points. There are several issues to be solved while setting up the NUFFT operator: the choice of the gridding kernel, sampling trajectory and a proper density correction function, which compensates for the overly dense population of samples in certain regions of non-Cartesian sampling patterns.

2.2.3. Types of Regularisation Constraints

In challenging contexts of MR spectroscopic imaging when there are multiple sources of potential errors, it is preferable to use a regularised version of the least-squares solution:

$$\widehat{\mathbf{x}} = \arg\min_{\mathbf{x}} \underbrace{\|\mathbf{y} - \mathbf{A}\mathbf{x}\|_2^2}_{Fidelity\,term} + \underbrace{\alpha\,\|\mathrm{R}(\mathbf{x})\|_2^2}_{Penalty\,term} \tag{2.45}$$

Minimisation of the cost function of this form ensures that estimated solution is consistent with experimental observations on the one hand, and on the other, that it satisfies the predefined constraints formulated by a penalty (or regularisation) function. This is a classical approach to introduce additional information which shall serve to discard non-plausible solutions.

The choice of the regularisation term is critical and defines the outcome of reconstruction but also application-specific since the term inherently gives preference to a solution with desirable properties. There are numerous ongoing studies which investigate the applicability of different regularisation techniques for reconstruction of MR images.

Tikhonov Regularisation

This regularisation method is the simplest and the most commonly used one. It minimises the norm of the solution:

$$\widehat{\mathbf{x}} = \arg\min_{\mathbf{x}} \|\mathbf{y} - \mathbf{A}\mathbf{x}\|_2^2 + \alpha \, \|\mathbf{I}(\mathbf{x} - \mathbf{x}_r)\|_2^2 \tag{2.46}$$

where $\mathbf{x}_r$ is a reference regularisation image, possibly zero, α is a regularisation parameter, which when large leads to oversmoothing, small α – to good fitting but less regular solutions, and $\alpha = 0$ brings back to unregularised naive least-squares solution. With $\mathbf{x}_r = 0$ the system has the closed form solution:

$$\widehat{\mathbf{x}} = (\mathbf{A}^\mathsf{T}\mathbf{A} + \alpha\mathbf{I})^{-1}\mathbf{A}^\mathsf{T}\mathbf{y}. \tag{2.47}$$

This penalty is rarely chosen in MR applications since it aims towards solutions with small norm, by this reducing the contrast unless the regularisation image is properly selected. The algorithm of the constructing optimal $\mathbf{x}_r$ by collecting additional reference data in the centre of *k*-space is described by Ying et al. [99].

Total Variation

Initially proposed as an efficient image denoising algorithm [76] and widely used in signal- and image processing for noise removal, total variation has been recently investigated for MR image reconstruction [25].

The constrained minimisation problem in context of preservation of total variation of the image is given by:

$$\widehat{\mathbf{x}} = \arg\min_{\mathbf{x}} \|\mathbf{y} - \mathbf{A}\mathbf{x}\|_2^2 + \alpha \mathrm{TV}(\mathbf{x}), \; \mathrm{TV}(\mathbf{x}) = \int\limits_{\Omega} |\nabla \mathbf{x}| \, \mathrm{d}\vec{r} = \int\limits_{\Omega} (|\nabla_x \mathbf{x}| + |\nabla_y \mathbf{x}|) \mathrm{d}x \mathrm{d}y \tag{2.48}$$

The advantage of total variation penalty is that it encourages piecewise constant solutions and preserves image edges at the same time, which makes it superior over Tikhonov regularisation. In MRI field it proved to reduce noise and artifacts caused by undersampling in parallel MR imaging with non-Cartesian sampling pattern [50], [6]. In both studies data was acquired using radial *k*-space trajectory with different number of spokes. Images exhibited characteristic striking artifacts after conventional regridding reconstruction but which were radically reduced in iterative reconstruction with TV penalty term.

The downside of variational penalties and their difference from Tikhonov-like regularisation terms is that the latter are L_2 norms (the square root of the sum of squared pixel values) of image while TV norms are L_1 norms (the sum of absolute pixel values) of image derivatives. L_1 estimation explains the difficulties associated with reconstruction with TV penalty: it is nonlinear, computationally complex and no well-understood closed form solution exists. [76]. The search for minimum of the cost function is realised using an iterative approach from groups of line search or trust region methods, which implies higher time costs.

The choice of weighting parameter α is not trivial either. Two common methods for its selection are: L-curve, which reflects the interdependence between regularisation parameter and corresponding residual error, and generalised cross-validation, which exploits the variability of data itself about the likely level of fit needed to estimate the regularisation parameter.

Total Generalised Variation of the Second Order

It has been shown in [9] that under certain conditions, for instance, when the image contains regions with sloping intensity, reconstruction with TV penalty will cause so-called staircasing artifacts being unable to restore the slanted image appearance. The same work contains the derivation of the second order total generalised variation (TGV) functional. TGV is claimed to perform better in scenario of images with slanted regions by providing the optimal balance between the first- and the second derivative of a function [49]:

$$\mathrm{TGV}_{\alpha}^{2}(\mathbf{x}) = \min_{\nu} \alpha_1 \int_{\Omega} |\nabla \mathbf{x} - \nu| \, dr + \alpha_0 \int_{\Omega} |\varepsilon(\nu)| \, \mathrm{d}r \tag{2.49}$$

where $\varepsilon(\nu) = \frac{1}{2}(\nabla\nu + \nabla\nu^{\mathsf{T}})$ is the the symmetrised derivative and the minimum is taken over all complex vector fields ν on Ω. With non-zero weight α_0 TGV, in contrast to TV, accounts for the second derivative as well. In [49] a very intuitive explanation of this property of TGV is given, based on the variation of ν depending on the order of the second derivative $\nabla^2\mathbf{x}$ in smooth regions or in the neighbourhood of edges. It has been shown that in the same case of reconstruction from radial k-space data, TGV outperforms TV in terms of resulting image quality and presence of artifacts. Since the functional has been developed relatively recently, there is still lack of statistics on how iterative reconstruction with TGV constraint would perform in different experimental settings.

Sparsity

The notion of sparsity, essentially meaning the fraction of zero elements in a matrix, has been broadly used in domain of signal- and image processing in context of image recovery and deblurring [97], [101], audio signal coding and separation [68].

It has been observed, that after certain transformations are applied to digital images, the level of sparsity can be drastically increased. The simple example would be of a 2D signal in image domain and its representation in frequency domain after Fourier transform (Fig. 2.12). The original image contains 65 % of "large"-intensity pixels (with values higher than 0.1 in the intensity range [0, 1]) versus negligible 0.02 % of pixels in this range for the Fourier transformed version.

The theory of sparse representations says that provided there is a signal $x(t), 1 \leqslant t \leq T$ in time domain, or as a vector $\mathbf{x} = [x(1)...x(T)]^{\mathsf{T}}$, it can be decomposed into a sum of the Q basis vectors $[\phi_q(1)...\phi_q(T)]^{\mathsf{T}}$ weighted by coefficients u_q

$$x(t) = \sum_{q=1}^{Q} u_q \phi_q(t). \tag{2.50}$$

Representation of a signal, in which only a small number of the coefficients of $\mathbf{u} = [u(1)...u(Q)]^{\mathsf{T}}$ are non-zero, are called sparse representations. Let us denote Ψ the sparsifying transform

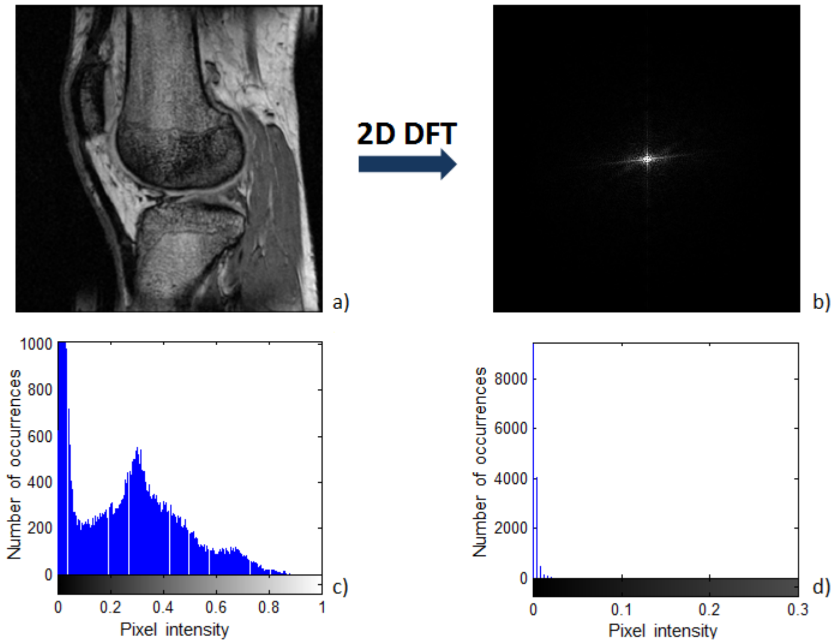

Figure 2.12.: (a) and (b) Proton MR image of the knee joint and its two-dimensional discrete Fourier transform. (c) and (d) The corresponding histograms reflecting the sparse structure of the Fourier-transformed data

[57] or operator which maps the image from pixel domain to a sparse form. Then typical formulation of minimisation problem is given by

$$\hat{\mathbf{x}} = \arg\min_{\mathbf{x}} \|\mathbf{y} - \mathbf{A}\mathbf{x}\|_2^2 + \alpha \|\Psi\mathbf{x}\|_1 . \tag{2.51}$$

There are many alternative transformations leading to a sparse representation of signal, such as the discrete Fourier transform (DFT), the discrete cosine transform (DCT) or the discrete wavelets transform (DWT). I refer the reader to [11] for the concise well-explained theory of compressed sensing (or compressive sensing (CS)), a signal processing technique for acquiring and recovering a sparse signal in the most efficient way with the help of an incoherent subsampling [12].

Sparse representation of data has advantages of

- saving significant amount of memory and speeding up the computational processes since only non-zero values have to be stored;
- noise removal by discarding portion of ”unwanted” coefficients, presumably corresponding to noise;
- data reconstruction. Provided an appropriate recovery scheme is used, the image can be reconstructed from the sparse domain using relatively few and possibly randomly distributed samples.

The successful application of sparsifying transform to reconstruct MR images from heavily undersampled *k*-space data by Lustig et al. [57] has motivated many research groups to explore dedicated compressed sensing techniques for other aspects of NMR imaging. Spatio-temporal sparsity has been exploited for correction of motion artifacts in free breathing cardiac imaging [89], in parallel imaging for MR angiography [83], for acceleration of MR diffusion imaging [96]. The entire group of so called *k*-t methods has evolved: *k*-t BLAST [86], *k*-t FOCUSS [39], *k*-t PCA [65], all are based on the concept of undersampling the *k*-space over time (*k*-t space) and propose different algorithms for recovery of the solutions from the limited data.

With *k*-t PCA applied to 2D spectroscopic imaging of hyperpolarised pyruvate in the heart, as was shown in [93], it was possible to achieve denoising of low SNR data and accurate reconstruction of up to five-fold undersampled *k*-t data. In work [44] two-fold enhancement of SNR has been achieved using inherent sparsity of hyperpolarised ^{13}C spectra.

Underlying Anatomy

The beauty of the functional imaging, whether it is chemical shift, perfusion or diffusion weighted MRI, is the insight which these techniques give into the vital biological processes on the molecular level. In simple terms, when the proton NMR answers the question: how does the tumour look today (its localisation, size, shape and other morphological features), metabolic imaging can predict its behaviour tomorrow (or in one week/month). Changes in measured physiologic parameters in some cases show correlation with positive response to therapy already within two weeks of treatment [70], [62]. Because of this molecular imaging is considered to be key in realising personalised medicine: for therapy planning and follow-up of disease progression [51].

However, without anatomical reference the functional image can be hard to interpret, if not meaningless for reliable diagnosis. That is why accurate registration techniques [48], [17] and hybrid imaging solutions [74], [67], [90], where anatomical and functional information complements each other in the most efficient way, are in focus of active scientific research today.

One can assume that high-resolution MR images of the underlying anatomy could potentially serve as a prior and be included in reconstruction as a regularisation term. Indeed, such attempts have been done and show a great potential to improve functional images with much lower SNR.

Clear classification of methods to incorporate the anatomical priors has been proposed in [3] and distinguishes between 1) techniques which use the MR to define anatomical regions of interest (ROI), over which the functional data are then analysed, and 2) the approaches which directly use part of MR image to affect reconstruction.

Examples from the first group are SLIM (spectral localisation by imaging) [71] and its modified improved generalised version GSLIM [54], which use preselected homogeneous anatomical compartments to reduce the partial volume effect and cross contamination of signal from neighbouring regions. Applied hyperpolarised MR imaging with ^{13}C pyruvate SLIM demonstrated reduced contamination from the high pyruvate signal in the blood pool [80]. Another method SLOOP (spectral localisation with optimal point spread function) [55], in which strengths of phase-encoding gradient are chosen to match the point spread function of the region of interest, was implemented in cardiac MRS studies as well and showed up to 30 % SNR improvement compared with conventional CSI. These methods work good for spectral localisation in organs with well-segmented compartments.

Methods from the second group in their large part use probabilistic statistical methods to influence reconstruction of metabolic image by pixel-wise analysis of coregistered anatomical slice. The Bayesian framework allows for incorporation of the prior knowledge about the desired properties of unknown image. Shepp and Vardi proposed to search for a solution that maximises a posterior probability density function, or equivalently the log of the posterior probability, a so called maximum *a posteriori* estimate using Expectation Maximisation algorithm (EM) to reconstruct unknown emission density in Positron Emission Tomography (PET) [78]. If we denote a measured signal as $\mathbf{y}$ and the desired image as $\mathbf{x}$, then the cost function, being maximised, is a conditional probability function

$$\widehat{\mathbf{x}} = \text{arg max}_{\mathbf{x}\geq 0} \{P(\mathbf{x}|\mathbf{y}) = P(\mathbf{y}|\mathbf{x})/P(\mathbf{y})\} \qquad (2.52)$$

Alternatively, the prior distribution of the image $P(\mathbf{x})$ can be designed, which specifies the local interconnections between neighbouring pixels. They can be all statistically independent but can relate to the properties of pixels in the neighbourhood. To define such local interactions, Markov Random Field model was proposed [4] to convey a certain degree of correlation between pixels. This is called MRF prior and pixel interdependencies can be modelled with high flexibility allowing for controllable constrained reconstruction.

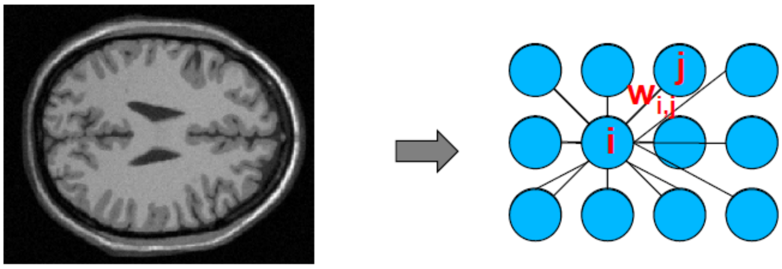

Figure 2.13.: Local interactions between adjacent pixels can be described with Markov Random Field model and its graphical representation. Where each pair of neighbours i and j is characterised by some label (weight) $w_{i,j}$

Anatomical boundaries and edges, extracted from high-resolution MR image, can be incorporated into MRFs in form of additional weighting variable which takes ”1” or ”0” values depending on the presence (absence) of boundary between each pair of neighbouring pixels. This is known as line site approach [34] and it serves the basis for many ”MR-guided” reconstruction algorithms. It allows for non-equal processing of the image, e.g. applying smoothing exclusively to image regions not lying on the boundaries, encouraging formation of connected boundaries or disregarding small closed regions [63].

Among other possible priors described in literature are intensity-based similarity metrics between low-resolution functional image and MR such as mutual information or joint entropy [82], [85].

The possible source of flaw in performance of all the methods is misregistration of functional and anatomical images and the fact that metabolic distribution does not necessarily replicates or follows the anatomical shape. It should be noted that all aforementioned techniques have been tried in reconstruction of PET images and showed the image quality enhancement only in numerical simulations with phantoms of decent resolution but rarely with real data. Another issue is objective data interpretation and risk of inducing the unwanted oversmoothing or, in contrast, loss of clinically valued details.

2.2.4. Iterative Reconstruction in MRI

It has been shown that iterative model-based approaches for solution of inverse problem in many imaging modalities (X-ray computer tomography (CT), optical imaging, MRI) usually outperform direct methods. At each iteration a new estimate of reconstructed image is computed in a way that, if inserted into the forward model, it would minimise the residual between theoretically predicted signal and the measured one. The more realistic the chosen physical forward model is, the more accurate, in ideal case, artifact-free image estimate we obtain.

However, computing the solution in an iterative fashion implies higher computational complexity and necessitates use of one of several dedicated methods for the search of minimum of the cost function. In Section 2.2.1 about the forward-inverse formalism, the discrete version of the signal model using finite-series approximation was given (Eq. 2.21), as well as formulation of the regularised least-squares estimation problem (Eq. 2.25). The purpose of this section is to give a concise overview of the iterative solvers and refer reader to works that demonstrate results of the most prominent approaches.

Among the most efficient iterative algorithms in solving large-scale linear problems $\mathbf{Ax} = \mathbf{s}$ is the conjugate gradient method (CG) [43]. The idea of the method is to present the solution as a weighted combination of mutually conjugate vectors and at each iteration to choose these conjugate vectors, residual and the next direction of the search so that the conjugacy condition stays preserved [40] (pseudo-code of the algorithm in Appendix A).

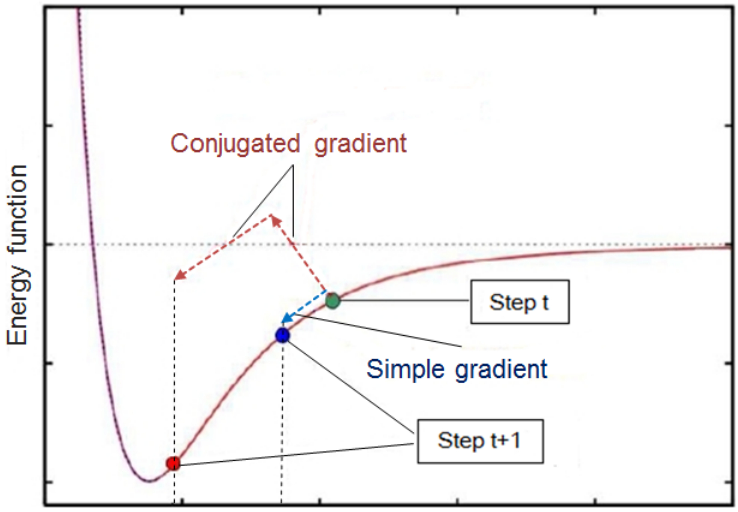

Figure 2.14.: Comparison between two gradient-based minimisation schemes for a 1D cost function [91]

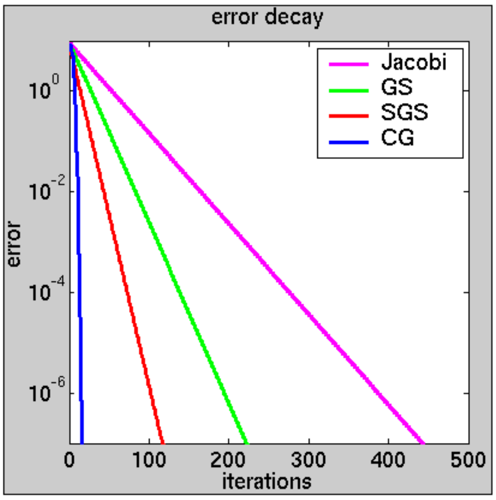

Figure 2.15.: Residual reduction for Jacobi, forward and symmetric Gauss-Seidel and Conjugate Gardient methods [30]

Performance of CG was compared with alternative iterative schemes for approximating the solution of a system of linear equations such as Jacobi or forward and symmetric Gauss-Seidel methods [52]. In terms of iterations needed until the error reaches a specified tolerance, CG showed the fastest convergence (Fig. 2.15). CG and its modified version of preconditioned CG are commonly used methods in the practice of iterative MR reconstruction [24].

As soon as a signal model includes additional physical effects, the problem becomes nonlinear in unknowns. Examples of such effects extending the physical model are:

- Coil sensitivities
- T_2 Relaxation
- Field inhomogeneities
- Diffusion, flow, motion etc.

Generalised nonlinear conjugate gradient approaches [41] or iteratively regularised Gauss-Newton method (IRGNM) have been successfully applied correspondingly for reconstruction of field-corrected MR images [84] and in parallel MR imaging with multiple receive coils [88], [50]. IRGNM tends to converge in fewer iterations than nonlinear CG but each step requires more computation due to calculation of the Hessian (matrix of second derivatives) in addition to the gradient.

Very recently algebraic reconstruction techniques (ART), known as state-of-the-art reconstruction technique in computer tomography and generalisation of the Kaczmarz method, demonstrated potential for MRI reconstruction [53]. It has an intuitive geometric interpretation, in which each row of the system of linear equations represents a hyperplane and when a unique solution to these equations exists, the intersection of all the hyperplanes is a single point giving that solution [47]. Although it does improve outcome of reconstruction compared to direct method of inversion, it is still slower than CG method, which additionally shows better performance (Fig. 2.16).

Pluses and minuses of analytical and numerical methods for image reconstruction can be summarised in Table 2.1.

Table 2.1.: Categorisation of Reconstruction Methods [Seminar: Novel Medical Imaging Methods, J. Vogel and T. Lasser, 2012]

Analytic (Direct) Methods	Numerical (Iterative) Methods
Examples: Filtered Back Projections (FBP); Gridding	Examples: Algebraic: Algebraic Reconstruction Technique (ART); Statistical: Conjugate Gradient (CG); Expectation Maximisation (EM)
Pros: Fast, intuitive; Inverse matrix can be pre-computed	Pros: Applicability for wide range of modalities; Accurate modelling of any physical effect
Cons: Cannot model any physical effect; Cannot be applied for any imaging modality	Cons: Slow, computationally expensive; Different mathematical framework for each imaging case

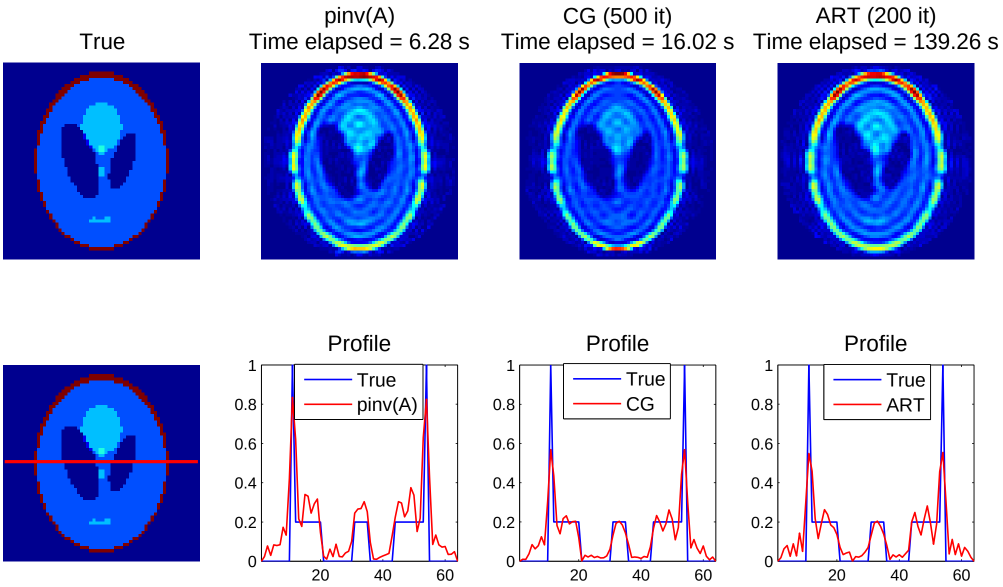

Figure 2.16.: Reconstruction of [64 × 64] pixel Shepp-Logan phantom using direct method of pseudo-inverse of the model matrix A and iterative: conjugate gradient (CG) and algebraic reconstruction technique (ART)

3. Methods and Experimental Strategy

3.1. Overview of Regularisation Techniques

In the previous chapter it has been shown that regularisation enhances quality of the solution when applied to the inverse ill-posed problems. Several types of regularisation terms were discussed. Here is the concise description of each discussed approach and a roadmap to the choice of methods implemented later.

Tikhonov regularisation

Key readings: Ying et al. On Tikhonov regularisation for image reconstruction in parallel MRI (2004) [99].
Pros: Simple computational realisation; direct regularisation method with existing closed form solution; flexibility in definition of regularisation matrix; L_2 norm-based constraint (easy to compute)
Cons: Choice of the reference regularisation image may not be straightforward; potential overregularisation effects, e.g. oversmoothing, reduced image contrast
Comments: Accepted for further investigation in application to reconstruction of metabolic images due to low time investment for implementation

---

Total variation

Key readings: Rudin et al. Nonlinear Total Variation Based Noise Removal Algorithms (1992) [76], Block et al. Undersampled radial MRI with multiple coils. Iterative image reconstruction using a total variation constraint (2007) [6].
Pros: Good edge preservation properties; allows for discontinuities in the solution; superiority over Tikhonov constraint for medical imaging applications has been shown [79]
Cons: Assumption of piecewise flat image is not always valid; common ”staircase” effect in the regions with steep intensity changes; L_1 norm-based constraint, nonlinear operator, computationally more expensive; TV functional is non-differentiable at locations where image gradient is zero
Comments: Accepted as a regularisation term in reconstruction of 13C images due to strong edge-preserving and denoising properties

---

Total generalised variation

Key readings: Knoll et al. Second order total generalised variation (TGV) for MRI (2011) [49]
Pros: Incorporates higher-order derivative information; captures texture not only of the flat but slanted regions and preserves edges; acts as conventional total variation (TV)

penalty when the second regularisation parameter is equal to one
Cons: More complex numerical realisation; two instead of one regularisation parameters defining the balance between the first- and the second derivatives
Comments: Accepted as a regularisation term in reconstruction of 13C images due to good denoising, edge preservation properties, higher flexibility in setting the optimum between smoothing and sharpening the image structures, and very scarce information on other applications of TGV regularisation for reconstruction of functional images.

Sparsity-promoting regularisation

Key readings: Lustig et al. Compressed sensing MRI (2008) [58], Kern et al. Wavelet-Based Reconstruction for Magnetic Resonance Imaging (2012) [40]
Pros: Acceleration of imaging by reconstruction from undersampled data
Cons: Non-trivial numerical realisation
Comments: Dismissed from further consideration due to inherently non-sparse acquired imaging data. Further undersampling would not bring any benefits.

Anatomical constraint

Key readings: Bai et al. Magnetic resonance-guided positron emission tomography image reconstruction (2013) [3]
Pros: Exploiting the natural correlation between low-resolution functional and high-resolution morphological images
Cons: Exact coregistration of images is prerequisite; complex probabilistic statistical methods to define pixel relations and influence reconstruction; high risk of oversmoothing and loss of clinically valuable details
Comments: Realisation of a simple form of support anatomical mask was performed.

All aforementioned regularisation techniques share a common complexity, namely the necessity to carefully select the regularisation parameter, which defines the trade-off between the goodness of fit, equivalently, consistency of the solution with the acquired data, and the reduction of noise and unregularities.

3.2. Iterative Regularisation for Linear Inverse Problem

To evaluate the effect of several penalty terms on the outcome of reconstruction of ^{13}C metabolic MR images, the following regularisation methods were implemented:

- Tikhonov regularisation
- Total Variation penalty
- Total Generalised Variation penalty
- Anatomical mask

Reasoning behind each of the methods can be found in Section 2.2.3. Here the implementation strategy and used tools are given. All the inversion algorithms were implemented in Matlab (Mathworks Inc., Natick, MA), and executed on a desktop computer with a Intel Core2 Quad Processors CPU operating at 2.67 GHz and 8 GB of RAM.

3.2.1. Iterative Solver and Realisation of Regularisation Terms

Iterative solver has been chosen after objective function has been correctly classified as *linear least-squares* with *general smooth constraint* and the model matrix **A** is *large* and *sparse*. Relevant solver then are `fmincon`, `lsqlin`, `lsqr`. In out task we used `lsqr` method which is an implementation of a conjugate-gradient type method for solving sparse linear equations and sparse least-squares problems [64] such as:

$$\widehat{\mathbf{x}} = \arg\min_{\mathbf{x}} \|\mathbf{A}\mathbf{x} - \mathbf{s}\|_2^2 + \lambda \|\mathtt{R}(\mathbf{x})\|_2^2 , \tag{3.1}$$

where $\mathtt{R}$ is operator which performs the regularisation transformation.

For realisation of Tikhonov and Total Variation (TV) penalty terms, the earlier developed function, which performs convolution of image with a pre-defined kernel, was modified to calculate and store the L_2-norm and directional derivatives of image region in the selected neighbourhood of pixels in case of Tikhonov and TV terms, respectively. For 2D image the 8-pixel neighbourhood was used for calculation. If we assign a single index pair $i \in [1, ..., m], j \in [1, ..., n]$ to each pixel and denote the set of neighbours of pixel $x_{i,j}$ as N_{ij}, then for the 8-neighbor system the general form of regularisation function reads:

$$\mathtt{R}(\mathbf{x}) = \sum_{\{i,j\}=1}^{N} \sum_{i,j \in N_{ij}} \chi(x_{i,j}) \tag{3.2}$$

Tikhonov term:

$$\mathtt{R}(\mathbf{x})_{Tikhonov} = \sum_{\{i,j\}=1}^{N} \sqrt{\sum_{i,j \in N_{ij}} |x_{i,j}|^2}, \tag{3.3}$$

Total variation term:

$$\mathtt{R}(\mathbf{x})_{TV} = \sum_{\{i,j\}=1}^{N} \sum_{i,j \in N_{ij}} |x_{i+1,j} - x_{i,j}|^2 + |x_{i,j+1} - x_{i,j}|^2 . \tag{3.4}$$

where with i, j we denote the linear index equivalent to the row and column subscripts of 2-dimensional array, and the penalty function $\chi(x_i, x_j)$ actually specifies a transformation on each pair of neighbouring pixels.

For realisation of regularisation with total generalised variation (TGV) penalty, the first-order primal-dual algorithm described in [14] has been employed (see Appendix A). The use case of TGV regularisation for undersampling reconstruction in parallel MRI of the human brain was provided by Dr. Florian Knoll (TU Graz), modified and adapted considering the specifics of our application with permission of author.

The discrete version of the reconstruction problem (Eq. 3.1) with a sample spacing $h = 1$

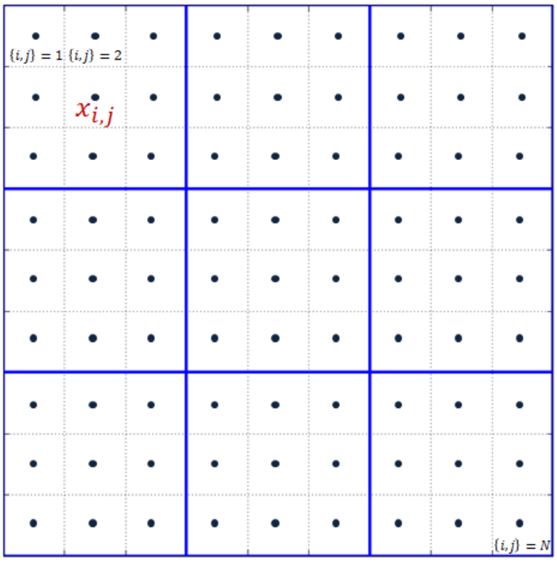

Figure 3.1.: Example of 9×9 grid of pixels divided into 8-neighbor regions. For each pair of pixels in the region the result of regularisation transformation was computed and stored

and TGV term reads

$$\widehat{\mathbf{x}} = \arg\min_{\mathbf{x}^h} \left\| \mathbf{A}^h \mathbf{x}^h - \mathbf{s}^h \right\|^2 + TGV_\alpha^2(\mathbf{x}^h), \tag{3.5}$$

where $\mathbf{x}^h$ is vector of unknowns, $\mathbf{A}^h$ is a discretised linear forward encoding operator, $\mathbf{s}^h$ is the measured discrete spiral sampling data and TGV operator expressed in a form:

$$TGV_\alpha^2 = \min_{\mathbf{x}^h, \nu^h} \alpha_1 \left\| \nabla^h \mathbf{x}^h - \nu^h \right\|_1 + \alpha_0 \left\| \varepsilon^h(\nu^h) \right\|_1 . \tag{3.6}$$

where superscript h denotes the discrete setting, ε^h is operator performing a symmetrised derivative on complex-valued vector ν.

Equation 3.5 is a convex-concave saddle-point problem and according to the duality principle of the optimisation theory can be viewed as

$$\min_{\mathbf{x}^h, \nu^h} \max_{p^h, q^h, r^h} \langle \nabla^h \mathbf{x}^h - \nu^h, p^h \rangle + \langle \varepsilon^h(\nu^h), q^h \rangle + \langle \mathbf{A}^h \mathbf{x}^h - \mathbf{s}^h, r^h \rangle. \tag{3.7}$$

where p^h, q^h, r^h are the dual variables. The primal-dual algorithm for the reconstruction problem is given in Appendix.

3.2.2. Support Mask Formation

Reconstructed metabolic images usually contain unwanted, out-of-object signal, which manifests as noise and blob-like structures corrupting the image quality and sometimes preventing user from distinguishing object from the background. Anatomical constraint shows potential to improve image readability by suppressing the background noise.

Two methods were considered while implementing the support mask:

- Active contour based segmentation into foreground (object) and background regions
- Intensity based thresholding followed by the closing operation

Method proposed by Chan et al. in [15] was used for realisation of the first approach. The contour is defined by a level-set function, initiated by user and evolving in accordance to the update function (see Eq. 3.9).

$$\phi(x) = \begin{cases} -d(x) & \text{if } x \text{ inside countour} \\ 0 & \text{if } x \text{ belongs to countour} \\ +d(x) & \text{if } x \text{ outside countour} \end{cases} \tag{3.8}$$

where $d(x)$ specifies the distance from any pixel to the contour

$$\phi(x)^{t+1} = \phi(x)^t - \kappa\delta[(\frac{(I(x)-\mu_i)^2}{2\nu_i}) + (\frac{(I(x)-\mu_o)^2}{2\nu_o})] + \lambda \mathrm{div}(\nabla\phi(x)) \tag{3.9}$$

where t is timestep, $\phi(x)^0$ the level-set function from the user-defined contour, κ, λ are user defined scalars for controlling the evolution, δ is an analytic approximation of the Dirac function, $I(x)$ is the pixel intensity at x, μ_i, μ_o are the mean pixel intensities and ν_i, ν_o are the variance of the regions inside and outside the contour (zero level-set), respectively.

Segmentation of MR image in this case involves the following steps:

1. Anisotropic diffusion filtering of the initial proton image
2. Active contour based segmentation (Fig. 3.3 (a))
3. Post-processing of the distance map (Fig. 3.3 (b, c, d))
4. Smoothing by convolution with Gaussian filter of size $3\sqrt{\sigma}$ with standard deviation $\sigma = 1.5$

In order to further take into account signal-free regions within the object, the second approach was implemented. Steps are:

1. Anisotropic diffusion filtering of the initial proton image (Fig. 3.4 (a))
2. Histogram thresholding (Fig. 3.4 (b))
3. Closing operation with a disk-shaped morphological structuring element of radius $R = 3$ (Fig. 3.4 (c))
4. Smoothing by convolution with Gaussian filter of size $3\sqrt{\sigma}$ with standard deviation $\sigma = 1.5$ (Fig. 3.4 (d))
5. Projective transformations of the mask for improved registration (optional)

The optimisation problem to be minimised in case of anatomical constraint is:

$$\hat{\mathbf{x}} = \arg\min_{\mathbf{x}} \|\mathbf{A}\mathbf{x} - \mathbf{s}\|^2 + \lambda \|\mathbf{x}(\mathbf{I} - \mathbf{M})\|^2 , \tag{3.10}$$

where **I** is the identity matrix, **M** is a precomputed mask.

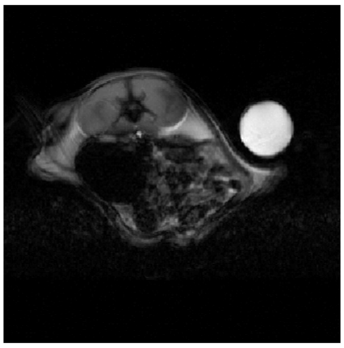

Figure 3.2.: T_2-weighted MR image of the slice through kidney of a rat

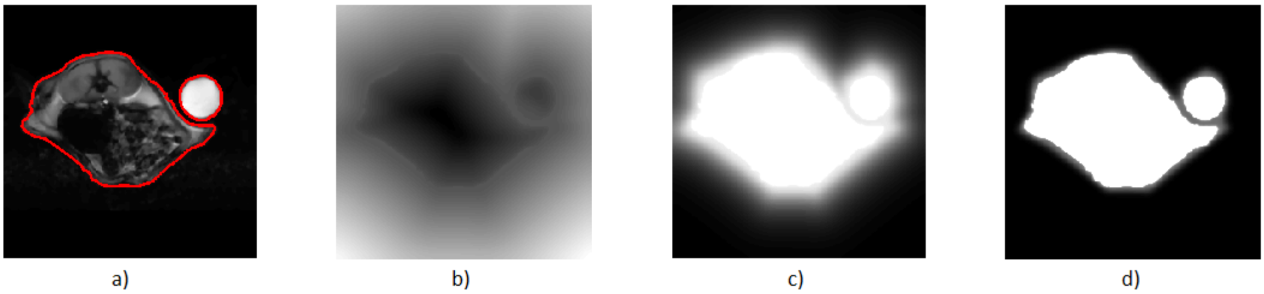

Figure 3.3.: Steps of mask formation using active contour based approach. (a) Active contour after 600 iterations. (b) Output distance map. (c) and (d) Stages of post-processing of the distance map by inverting and applying exponential weighting factor

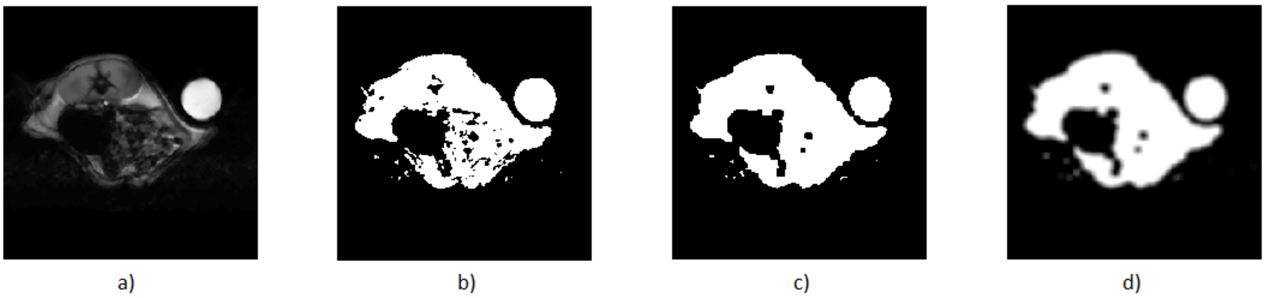

Figure 3.4.: Steps of mask formation using histogram thresholding approach. (a) Proton image after anisotropic filtering. (b) Thresholding using $T = 0.25$. (c) Morphological closing operation. (d) Convolution with Gaussian filter kernel ($\sigma = 1.5$)

3.3. First-Order Correction using Metabolic Time Curves

Some of the physical effects, briefly discussed in the previous chapter, include coil sensitivities, T_2 relaxation, field inhomogeneities, diffusion, flow, motion and potentially many other. If these effects are correctly modelled in the forward signal matrix, the inversion of it will yield more accurate reconstruction results then without incorporation of these priors.

Since the origin of *a priori* information varies for different types of MR studies (perfusion, diffusion MR, chemical shift MR imaging etc.), one could think of the appropriate extension to the physical model of ^{13}C metabolic MR imaging.

In multiple studies with hyperpolarised ^{13}C agents the reproducible behaviour of ^{13}C-pyruvate and its metabolic products: ^{13}C-lactate, ^{13}C-alanine, and ^{13}C-bicarbonate, has been observed [37], [37] (Fig. 3.5). Reproducibility of the illustrated time curves is explained by kinetics of hyperpolarised ^{13}C-pyruvate transport and metabolism in living cells [42].

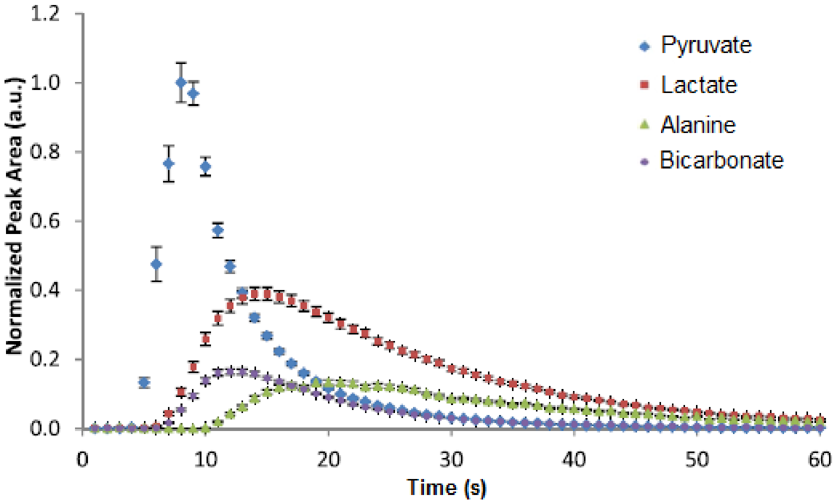

Figure 3.5.: An averaged time course of the fitted peak areas of pyruvate, lactate, alanine and bicarbonate from the fed rat heart (n = 4). Curves are normalised to the peak pyruvate signal intensity [20]

As was previously noted in Section 2.2.2, the currently employed method of least squares chemical shift imaging (LSCSI), which relies on multiple data acquisition and known resonance frequencies to resolve metabolites, does not account for the change of magnetisation level between single excitations and approximates it with a constant function.

Here we propose to use the measured metabolite time curves in order to compensate for dynamic signal change by deriving time-dependent correcting factors and solving the inverse problem:

$$\hat{\mathbf{x}} = \arg\min_{\mathbf{x}} \left\| \widetilde{\mathbf{A}}\mathbf{x} - \mathbf{s} \right\|_2^2, \quad \widetilde{\mathbf{A}} = \mathbf{K}\mathbf{A} \tag{3.11}$$

where **K** is a matrix of correcting factors. Further, we show how it is derived. This approach combines simplicity and computational efficacy of direct methods and increased accuracy of the model-based approaches.

3.3.1. Kinetic Modelling

Pyruvate-to-lactate conversion typically exhibits reproducible pattern. After injection of pyruvate *in vivo*, the signal intensity rapidly grows and reaches its peak shortly after the end of injection and its magnitude is typically times larger than the signal of lactate [98]. Then it decays due to combined effect of T_1 relaxation, RF excitation, irreversibly depleting the longitudinal magnetisation, and enzymatic conversion. Lactate signal, in contrast, increases gradually after the injection, and reaches the maximum ≈ 10 s after the pyruvate peak. Then follows a so-called "signal plateau", a quasi-steady-state lasting for ≈12-15 s and caused by self-compensating processes of T_1 relaxation and further lactate incoming from the conversion.

Such behaviour can be very well modelled using two-site exchange model describing the metabolic time courses with piecewise exponential equations governed by kinetic turnover rate, effective relaxation rates and the input function of the injected metabolite (Fig. 3.6).

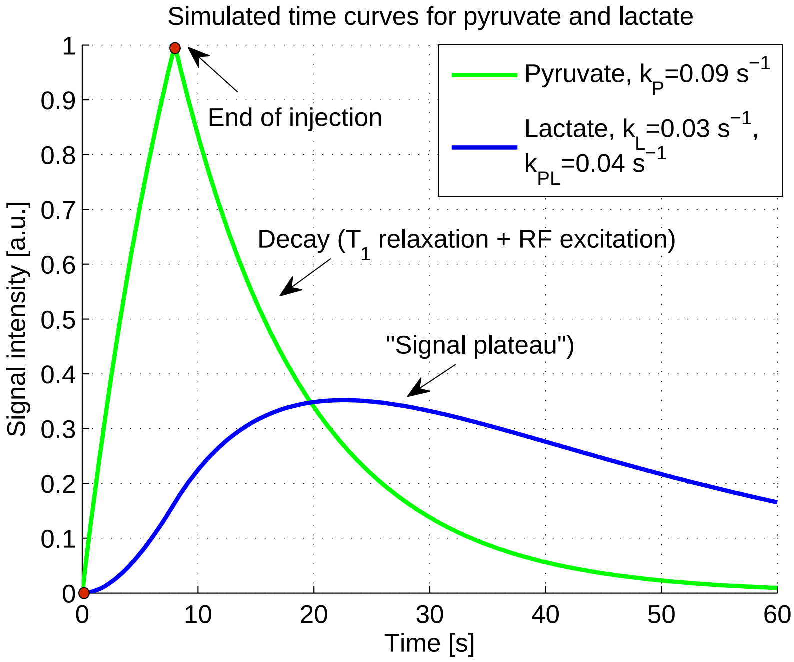

Figure 3.6.: Approximation of time curves for pyruvate and lactate according to the model of two-site exchange [18]

Equations 3.12, 3.13 are the modified Bloch equations, which describe pyruvate-lactate exchange rates $P \underset{k_{LP}}{\overset{k_{PL}}{\rightleftharpoons}} L$ [18] and, in principle, applicable for modelling conversion of pyruvate into other metabolic products

$$\frac{dP_z}{dt} = k_{LP}L_z - k_{PL}P_z - \rho_P(P_z - P_\infty) \tag{3.12}$$

$$\frac{dL_z}{dt} = k_{PL}P_z - k_{LP}L_z - \rho_L(L_z - L_\infty) \tag{3.13}$$

Here P and L denote pyruvate and lactate and P_z and L_z are their longitudinal magnetisations, P_∞ and L_∞ are corresponding equilibrium magnetisations at time $t = \infty$, k_{PL} and k_{LP} are rate constants of, respectively, forward and backward conversion from pyruvate to lactate and back, ρ_P, ρ_L are effective decay rates due to the spin lattice relaxation ($\frac{1}{T_1}$) and RF excitation.

In order to quantify the metabolite signal change and obtain the time curves, the area under the curve (AUC) was computed for each metabolite peak in a spectrum, reconstructed from free induction decay (FID), and summed up for all spectra in the span of measurement (Fig. 3.7).

Provided we now know the measured time curves P_z and L_z and assuming the equilibrium magnetisations negligibly small, it is possible to generate instantaneous fit by solving the system of equations for unknown rate constants. For lactate the solution reads:

$$\mathbf{k} = (\mathbf{A}^\mathsf{T}\mathbf{A})^{-1}\mathbf{A}^\mathsf{T}\mathbf{dL} \tag{3.14}$$

where

$$\mathbf{k} = \begin{bmatrix} k_{PL} \\ -k_L \end{bmatrix} \tag{3.15}$$

$$\mathbf{A} = \begin{bmatrix} P_z(t_1) & L_z(t_1) \\ \vdots & \vdots \\ P_z(t_n) & L_z(t_n) \end{bmatrix} \tag{3.16}$$

$$\mathbf{dL} = \begin{bmatrix} \frac{\Delta L_z(t_1)}{\Delta t_1} \\ \vdots \\ \frac{\Delta L_z(t_n)}{\Delta t_n} \end{bmatrix} \tag{3.17}$$

and $k_L = k_{LP} + \rho_L$ is an effective decay rate comprising effects from backward conversion, RF excitation and T_1 relaxation.

Fitting can be done by computing the increment iteratively:

```
input: $P_z$, $k_L$, $k_{PL}$
Initialisation: $\widehat{L}_z(t_1) = L_z(t_1)$, and $i = 1$;
repeat
$\Delta\widehat{L}_z \leftarrow (-k_L\widehat{L}_z(t_i) + k_{PL}P_z(t_{i+1})) \cdot \Delta t_{i+1}$;
$\widehat{L}_z(t_{i+1}) \leftarrow \widehat{L}_z(t_i) + \Delta\widehat{L}_z$;
$i \leftarrow i + 1$;
until $i \geq n$;
return $\widehat{L}_z$
```

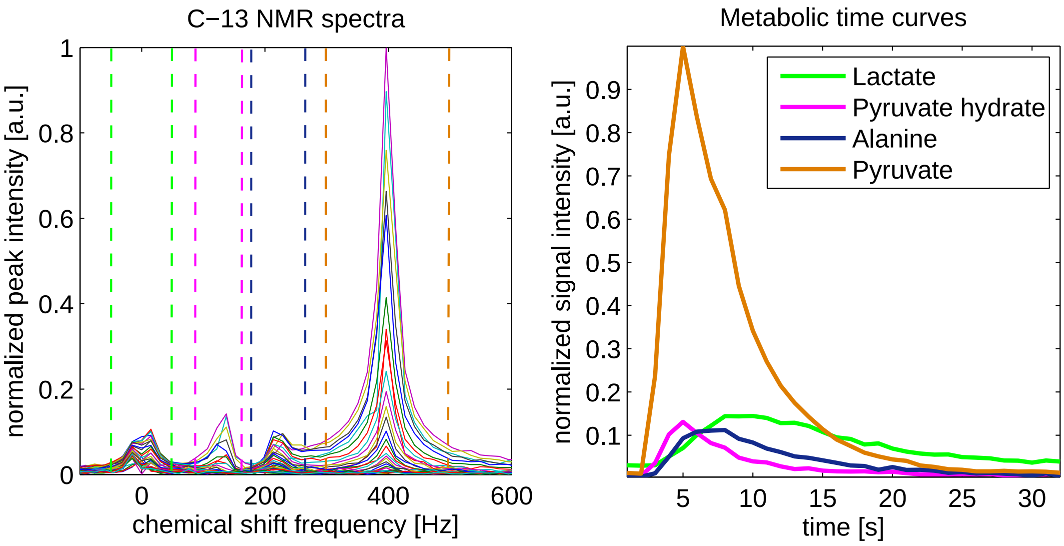

Figure 3.7.: (a) ^{13}C NMR spectra, repetition time=2 s, number of acquisitions=32. (b) Resulting time curves for pyruvate and its metabolites, all normalised to the maximum of pyruvate signal

The matrix of correcting factors **K** has a form:

$$\mathbf{K} = \begin{bmatrix} \hat{P}_z(t_1) & \hat{L}_z(t_1) & ... & \hat{M}_z(t_1) \\ \hat{P}_z(t_2) & \hat{L}_z(t_2) & ... & \hat{M}_z(t_2) \\ \vdots & \ddots & & \vdots \\ \hat{P}_z(t_n) & \hat{L}_z(t_n) & ... & \hat{M}_z(t_n) \end{bmatrix}. \tag{3.18}$$

where M_z denotes the time curve of any downstream metabolite produced apart from lactate. Spectral encoding matrix of IDEAL chemical shift imaging module given in Section 2.2.2 is then modified into:

$$\tilde{\mathbf{C}} = \begin{bmatrix} \hat{P}_z(t_{1,n}) \cdot e^{i2\pi\Delta f_1 \tau_{1,n}} & ... & \hat{M}_z(t_{1,n}) \cdot e^{i2\pi\Delta f_N \tau_{1,n}} \\ \hat{P}_z(t_{2,n}) \cdot e^{i2\pi\Delta f_1 \tau_{2,n}} & ... & \hat{M}_z(t_{2,n}) \cdot e^{i2\pi\Delta f_M \tau_{2,n}} \\ \vdots & \ddots & \\ \hat{P}_z(t_{M,n}) \cdot e^{i2\pi\Delta f_1 \tau_{M,n}} & ... & \hat{M}_z(t_{M,n}) \cdot e^{i2\pi\Delta f_N \tau_{M,n}} \end{bmatrix}. \tag{3.19}$$

where the double subscript simply means that M consequent values at times t_{n+1}, ..., t_{n+M} must be taken from the curve starting from the begin of measurement t_n.

3.3.2. Nonlinear Regression

The integral solutions to Equations 3.12, 3.13 for metabolite exchange rates are given by piecewise exponential equations [102]:

$$P_z(t) = \begin{cases} \frac{r_{inj}}{k_P}(1 - e^{-k_P(t-t_{arr})}), & t_{arr} \leq t \ < t_{end} \\ P_z(t_{end})e^{-k_P(t-t_{end})}, & t \geq t_{end} \end{cases} \tag{3.20}$$

$$L_z(t) = \begin{cases} \frac{k_{PL} r_{inj}}{k_P - k_L}(\frac{1-e^{-k_L(t-t_{arr})}}{k_L} - \frac{1-e^{-k_P(t-t_{arr})}}{k_P}), & t_{arr} \leq t < t_{end} \\ \frac{P_z(t_{end})k_{PL}}{k_P - k_L}(e^{-k_L(t-t_{end})} - e^{-k_P(t-t_{end})}), & t > t_{end} \\ \quad +L_z(t_{end})e^{-k_L(t-t_{end})}, & \end{cases} \tag{3.21}$$

where k_P, k_L are effective decay rates of pyruvate and lactate, respectively [s^{-1}]; k_{PL} is the forward ($Pyr \rightarrow Lac$) conversion rate [s^{-1}]; r_{inj} is the injection rate [mL/s]; t_{arr}, t_{end} are times of arrival of agent and the end of injection respectively [s].

With this model of metabolite signal change we can perform curve fitting to the measured data and estimation of the relevant kinetic rates. If we denote a column matrix of relative metabolite concentrations over time as
$\mathbf{b} = [M_{Pyr}(t_1), ..., M_{Pyr}(t_n), M_{Lac}(t_1), ..., M_{Lac}(t_n)]^\mathsf{T}$ and $\mathbf{u}$ - vector of unknowns: $\mathbf{u} = [k_P, k_{PL}, k_L, r_{inj}, t_{arr}, t_{end}]^\mathsf{T}$, the system of nonlinear equations arises:

$$\begin{bmatrix} P_z(\mathbf{u})(t_1) \\ \vdots \\ P_z(\mathbf{u})(t_n) \\ L_z(\mathbf{u})(t_1) \\ \vdots \\ L_z(\mathbf{u})(t_n) \end{bmatrix} = \mathbf{b}, \text{ subject to } g_i^l \leq u_i \leq g_i^u \tag{3.22}$$

with the specified constraints on the solution components u_i: g_i^l, g_i^u stay for lower and upper bounds, respectively.

Trust region methods are efficient for solving nonlinear least squares optimisation problems of type $\min_{\mathbf{x}} \|f(x)\|_2^2$. They constitute the second class of optimisation strategies after line search methods and can be viewed as the classical Levenberg-Marquardt (LM) method [100]. This algorithm, in a nutshell, solves the nonlinear equations $f(x) = 0$ by iteratively constructing an approximation model (linear or quadratic) and computing its solution locally in proximity to the current iterate. If within this neighbourhood (within the trust region) the current approximation model still fits the original one sufficiently well, the region gets extended, otherwise shrinked. The decisive parameters of the algorithm are the trust region trial step and the criterion of acceptance of the trial step. The LM method chooses the step as follows:

$$d_k = -(J(x_k)J(x_k)^\mathsf{T} + \lambda_k I)^{-1} J(x_k) f(x_k) \tag{3.23}$$

where $J(x_k$ is the Jacobian of $f(x)$ and λ_k is a control parameter, which is updated iteratively.

In our computation we used the iterative solver `lsqnonlin`, which realises the above described method. Sufficiently good fitting with small number of iterations has been achieved when algorithm used approximation of the Jacobian by finite differences.

3.4. Experimental Methodology

3.4.1. Computer Simulation

In the mathematical simulation the original data representing two distinct metabolites was encoded according to the forward signal model described in Section 2.2.2. The inverse reconstruction problem was solved with several techniques to later compare their performance.

The 2D images associated with initial distribution of two substances (after moderate Gaussian smoothing ($\sigma = 1.5$)) were multiplied with the corresponding metabolite signal curves, modelled in accordance with the two-site exchange. Effective decay rates were assumed to be $k_P = 0.09\,\mathrm{s}^{-1}$, $k_L = 0.03\,\mathrm{s}^{-1}$ for pyruvate and lactate, injection rate r_{inj} = 10 mL/s and conversion rate could take three different values of $k_{PL} = 0.02\,\mathrm{s}^{-1}$, $k_{PL} = 0.04\,\mathrm{s}^{-1}$ and $k_{PL} = 0.08\,\mathrm{s}^{-1}$ to simulate different ratios between pyruvate in lactate. The time vector had spacing of 250 ms, t_{arr} = 0 s, t_{end} = 8 s and the offset t_{start} = 3 s indicating the start of the measurement (Fig. 3.8). The resulting data **x** has then undergone two-step spatial-spectral encoding ($\mathbf{x} \to \xi \to \mathbf{s}$). For sampling the data in the *k*-space an Archimedean spiral trajectory sampled every $\Delta t_i = 4\,\mu s$ was used, in total 1000 sampling points.

The simulation of IDEAL encoding was done with consideration of 7 echoes with relative time shift of 1.12 ms. We assumed a FOV of 1.0, a pixel resolution of 32×32 pixels and a relative chemical shift of 400 Hz. The additive white Gaussian noise with zero mean and standard deviation $\sigma = 5$ was applied to get the final ”measured” signal.

As a reference for error quantification and to show performance of conventional reconstruction under the valid assumption for LSCSI method, additional data with the constant signal intensities within 7 IDEAL encoding steps were simulated.

3.4.2. Experiment Design with *in vivo* Data

Key stages of the ^{13}C measurement protocol are schematically reflected in Fig. 3.9. Here we briefly discuss each component. Material for the first three subsections is based on the work [21].

Scaner Specifications

Experiments were conducted on a parallel-transmit modified 3 T GE Signa Excite scanner (GE Healthcare, Milwaukee) using the whole body gradient coil with a maximum gradient amplitude 23 mT/m and a maximum slew rate of 77 T/m/s. Additionally a custom-built dual-tuned 1H/13C resonator, commonly known as ”rat coil”, operating at 127.7 MHz and 32.1 MHz, respectively, was used for radio frequency excitation and signal reception. It consists of a quadrature-tuned C12 birdcage connected with a 1H Alderman-Grant coil and is equipped with a ”mouse”-bed, ideally suited for preclinical experiments. Before start of scanning the pulse sequence for the hyperpolarised measurement must be configured and

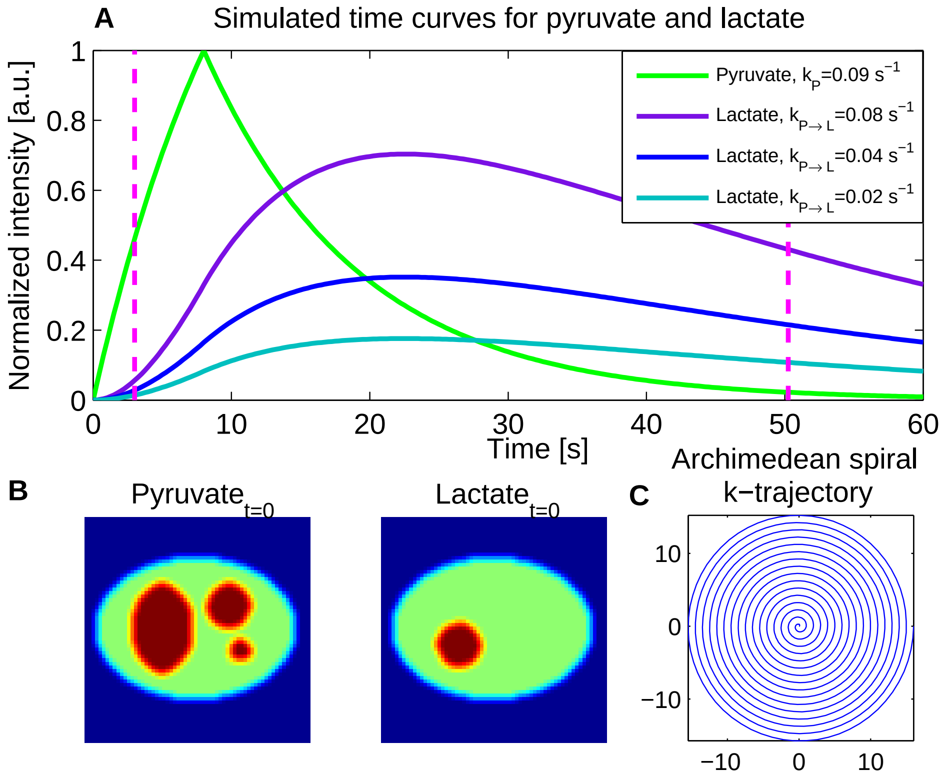

Figure 3.8.: Original images for pyruvate and lactate (B) are multiplied with kinetic curves (A) to model dynamic change of signal intensities on the interval (3,50) s. This true data is later encoded with spiral *k*-space trajectory (C)

coils chosen and tuned according to the use. To set correctly the centre frequency/transmit gain (TG)/shim values, a lactate reference syringe is placed at the inner edge of the coil and a preliminary scan is performed. All animal studies were performed on laboratory rats. For imaging experiments on healthy animals, outbred Wistar rats were subjected to measurements. For tumour studies, female inbred Fischer F344 rats were used. In this type of studies all animals had subcutaneously implanted tumour, in the majority of cases: MAT B III breast tumour model or multifocal hepatocellular carcinoma induced by the hepatocarcinogen, diethylnitrosamine (DENA).

Prior to experiment each rat is anesthetised with 1-3 % isoflurane with oxygen (delivered at 1.5 L/min) and a catheter is inserted into a tail vein for administration of the hyperpolarised ^{13}C solution. Afterwards, the animal is transferred to a water-driven heating pad on the coil-attached mouse bed to balance the body temperature during anaesthesia. Quantitative life parameters, such as heart and respiration rate, body temperature and oxygen saturation are continuously monitored throughout the experiment.

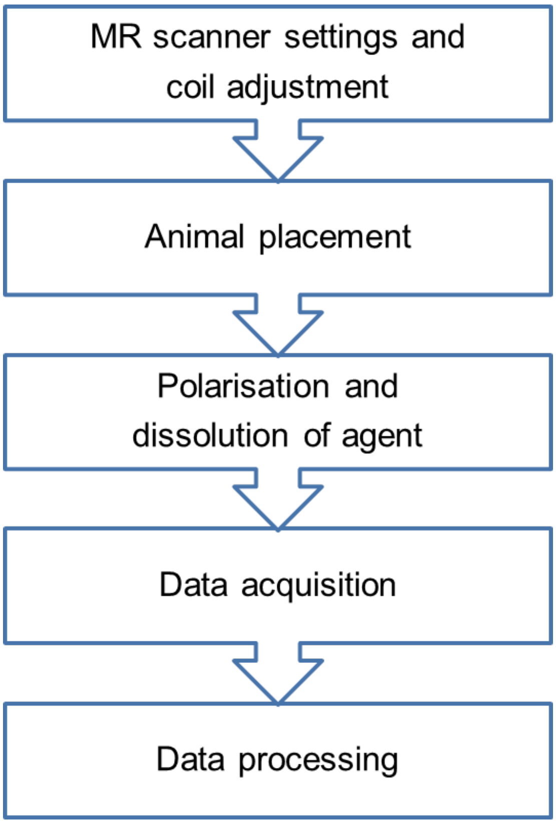

Figure 3.9.: ^{13}C metabolic imaging workflow

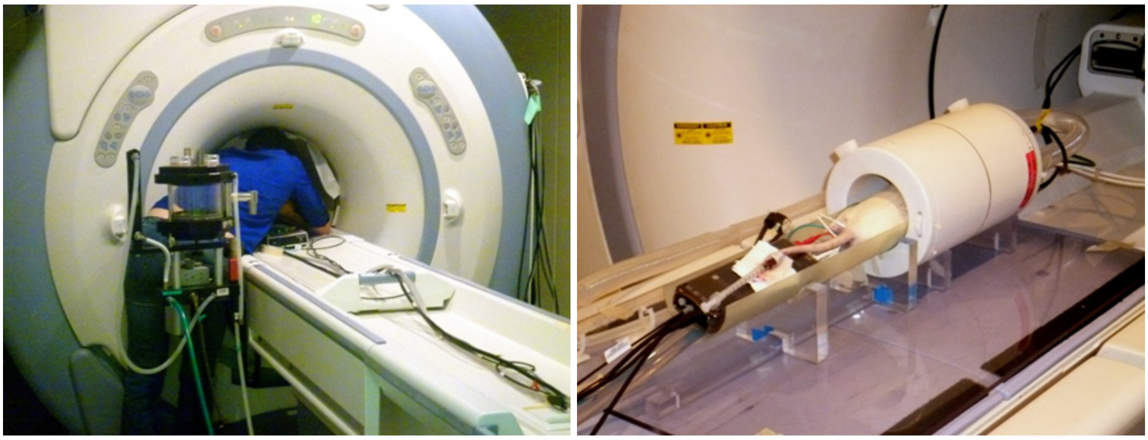

(a)

(b)

Figure 3.10.: Animal placement in 3 T MR scanner. (a) Fixation of the life monitoring devices. (b) Animal coil with the mouse-bed and the rat inside after injection of pyruvate

Polarisation and Dissolution Processes

Injected solutions used in the experiments contained as the active substance one of the following: fumarate, pyruvic acid, urine, dobutamin. Here the standard procedure of preparation of polarised substrate based on pyruvate is described. It consists of 20 M [1-13C] pyruvic acid, 15 mM OX063 trityl radical, and 10 mM Dotarem. All components are weighted, mixed in a sample vial, and stored in the freezer to avert decomposition before the actual use. 30 mg of this mixture is polarised for 60-120 min in a HyperSense DNP polariser (Oxford Instruments, UK) operating at 3.35 T. Polarisation is achieved by microwave irradiation of the sample at 1.4 K and the electron resonance frequency of 94 GHz. For dissolution of a polarised sample a solution containing 80 mM tris(hydroxymethyl)-aminomethane (TRIS) buffer, 80 mM NaOH and 0.1 g/L Na2-disodium (EDTA) heated to 100°C at 10 bar is used. The final solution contains 80 mM hyperpolarised [1-13C] pyruvate and has pH of 7.5 [21].

Data Acquisition

Proton Imaging

Proton MR images were acquired in axial, sagittal and coronal planes using standard proton gradient echo acquisition or a fast spin-echo sequence and served as anatomical references for correct interpretation of results of ^{13}C-CSI experiments. Up to 35 slices in axial direction were acquired with thickness varying from 3 to 10 mm, 0 to 20 mm separation (depending on the location of organ of interest) and a nominal in-plane resolution of ca. 0.5 mm.

Chemical Shift Imaging

The pulse sequence which has been used in the vast majority of experiments is IDEAL spiral CSI (ISPCSI). The characteristic features of this pulse sequence are a spiral *k*-space trajectory used for spatial encoding and a linear increase in echo time between subsequent acquisitions. For details please refer to Section 2.1.4 and [94]. The sequence consists of a slice-selective RF pulse followed by an imaging module, in this case a 65 ms long single-shot spiral readout designed for a field of view FOV = 80 mm, bandwidth of 62.5 kHz and a nominal matrix resolution of 38 points. Other relevant imaging parameters are: flip angle (FA) of 10°, repetition time (TR) of 250 ms, slice thickness of 10 mm.

In study with 5 metabolites of interest, as was shown in work of Wiesinger et al. [94], optimal performance is achieved if in one complete CSI encoding module the pulse sequence is repeated 7 times with relative echo time shift of 1.12 ms. By continuously repeating the entire basic CSI encoding module (number of acquisitions = 32) time-resolved metabolic data can be acquired. Each of these modules is preceded by an additional slice-selective FID spectrum measurement, resulting in an approximately 2 s duration for a single time step. It serves as a source of prior information about the resonance frequencies within the slice for further reconstruction of metabolic images.

Data Processing

Slice-selective FID spectra are decomposed and for each slice the CS frequencies are manually determined. This spectral prior knowledge is important for adapting the echo-time spacing to the present CS resonance peaks and is prerequisite for the correct reconstruction of metabolite maps.

Afterwards low-pass filter is applied in the frequency domain, gradient strength is accounted for and chopping is performed according to the maximum object dimension.

FID acquisition data is separated from the actual imaging data and incomplete CSI encoding data is matched with used *k*-space trajectory by discarding the uncovered points. Gaussian filter and proper reshaping of the data complete the pre-processing step.

Applying Gaussian or Hamming filter mitigates the so called ”ringing” or Gibbs effect discussed in Section 2.1.4, which appears as a result of multiplying the data with a window function in the image domain, which is analogous to convolution with *sinc* function in the frequency domain. The effect is especially pronounced at the places of sharp signal change and multiplication with Hamming function smoothly attenuates the signal at the borders.

Imaging data then undergoes reconstruction either by conventional inversion of the signal model matrix, which we for simplicity further denote as $pinv(A)$, or by iterative reconstruction after chemical shift separation with TGV operator and using anatomical constraint or reconstruction with derived correcting factors. In case of conventional inversion of the encoding operators, this is a two-step process. The theoretic background is thoroughly explained in Section 2.2.2. In case of iterative reconstruction, the first step of linear least squares chemical shift separation stays unchanged, then the resulting metabolite maps in *k*-space and the gridding operator with a proper density compensation function go as input to the function which assembles fidelity and regularisation terms and solves the problem (see Appendix for UML diagrams).

3.4.3. Experiment on a Phantom

A simple phantom consisting of light plastic vial holder for three containers and a reference lactate syringe was built (Fig. 3.11). The goal of the experiment was to conduct the catalysation of pyruvate in lactate following the reaction:

$$\text{Pyruvate} + \beta - \text{NADH} \xrightarrow{L-LacticDehydrogenase} \text{L-Lactate} + \beta - \text{NAD} \tag{3.24}$$

Conversion of pyruvate to lactate is catalysed by lactic dehydrogenase (LDH) and occurs in the presence of nicotinamide adenine dinucleotide reduced form (NADH) which is then undergoes oxidation with product: nicotinamide adenine dinucleotide oxidised form (NAD+).

The block scheme in Fig. 3.12 presents the components of the reaction and specifies the key parameters such as volume, molarity and density of the active substances (see Appendix A, Algorithm 3). Each vial contained 0.2 mL of lactic dehydrogenase enzyme. After polarisation process pyruvate was mixed with NADH and added to vials till the final volume of 1 mL. Calculation for 3 vials and accounting for 0.5 mL dead volume left on the walls of catheters is straightforward.

Total number of excitations for spectral encoding with IDEAL spiral CSI was set to 5, repetition time TR = 500 ms and flip angle FA = 10°.

Figure 3.11.: Plastic vial holder with four containers and attached catheters

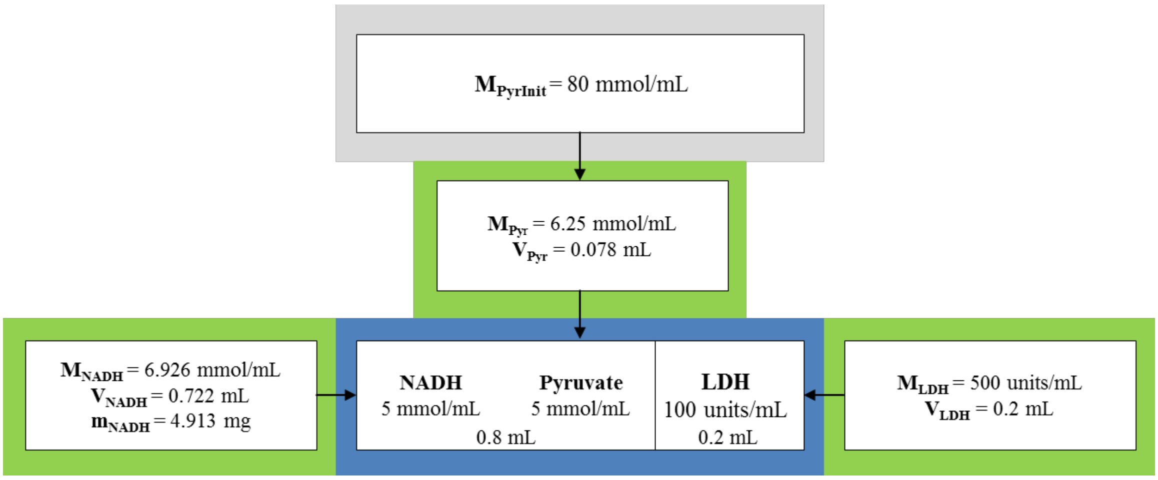

Figure 3.12.: The key components of the reaction from Eq. 3.24. Where M_x, V_x, m_x specify molarity, volume, mass of the substances added to yield the final volume of 1 mL

3.5. Image Quality Assessment Metrics

There are two applications of image quality assessment in this work: to evaluate performance of reconstruction techniques in terms of resulting image quality and to optimise certain regularisation parameters. A good image metric should correlate with perceived image quality. Which of existing metrics is more objective is still controversial issue. Signal-to-Noise Ratio (SNR) and Mean Squared Error (MSE) are the most widely used image quality metrics [92].

In the mathematical simulations all results were evaluated using root-mean-square error (RMSE) given by [35]:

$$\mathrm{RMSE} = \sqrt{\frac{\sum_i D_i^2}{\sum_i G_i^2}} \tag{3.25}$$

where $D_i = P_i - G_i$ is the difference between i-th pixel of reconstructed image P_i and the ground truth image G_i.

In studies with *in vivo* data, when the ground truth was not available, the signal-to-noise metric was used. It measures the relative signal strength compared to the background noise and has the form:

$$\mathrm{SNR} = \sqrt{2 - 0.5\pi}\frac{\mathrm{mean}(\mathrm{ROI}_2)}{\mathrm{std}(\mathrm{ROI}_1)} \tag{3.26}$$

where in the numinator stays the mean signal intensity over a region of interest ROI_2 containing the object, and in the denominator – the standard deviation of the background signal for a region without object ROI_1, $\sqrt{2 - 0.5\pi}$ is a correcting factor.

An additional metric was used to evaluate the preservation of image structures. From the mean signal within two regions of interest (Fig. 3.13), containing the object (ROI_2) and in the gap between structures (ROI_3) the contrast can be calculated:

$$\mathrm{C} = \frac{\mathrm{mean}(\mathrm{ROI}_2) - \mathrm{mean}(\mathrm{ROI}_3)}{\mathrm{mean}(\mathrm{ROI}_2)} \tag{3.27}$$

From the equations of the two-site exchange model (Eq. 3.12, 3.13) a metric to quantify the transfer rate of conversion of pyruvate to lactate can be derived by dividing the integral of the metabolite signal by the integral of the substrate pyruvate signal:

$$\frac{\int L_z(t)dt}{\int P_z(t)dt} = \frac{k_{P\to L}}{k_L} \tag{3.28}$$

where $k_{P\to L}$ and k_L are the respective kinetic rate constants of pyruvate-to-lactate conversion and the effective relaxation rate for lactate. With this quantitative measure the performance of reconstruction techniques was evaluated in terms of ability to correctly preserve the concentration differences between distinct compartments.

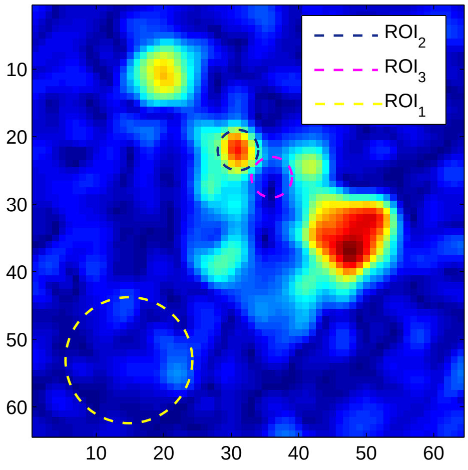

Figure 3.13.: Example of regions of interest (ROIs) used for calculation of image quality metrics in Eq. 3.26 and 3.27

4. Results and Discussion

4.1. Error Quantification for Conventional LSCSI Method

The true data for consequent spatial-spectral encoding according to the signal model, described in Section 2.2.2, were given by time series of 2D images of the size 64 pixels along each dimension. It corresponded to data acquisition each 250 ms in the interval (3,50) s (for description of the computer experiment see Section 3.4.1). Signal intensities of two regions over time are presented in Fig. 4.1 (b), where the staircase lines correspond to the second case with simulating the constant signal magnitude in the span of 7 acquisitions of each consequent IDEAL imaging module. This was done to model the "valid" assumption for the least-squares chemical shift method (LSCSI) currently being employed for the separation of individual metabolites at the initial reconstruction stage.

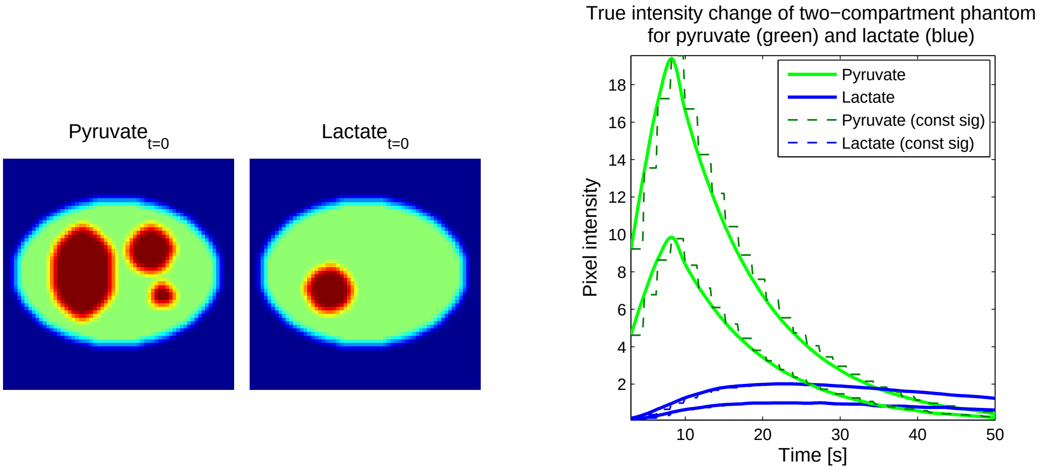

(a) Ground truth for pyruvate and lactate images at the null time point

(b) True intensity change of two-compartment phantom for pyruvate (green) and lactate (blue)

Figure 4.1.: Initial intensity maps and signal curves for simulation of time resolved metabolic images

The first observation was that, when reconstructed with the same algorithm of the direct matrix inversion, resulting images corresponding to the data with intervals of non-varying signal do not exhibit any significant artifacts except those caused by additive white Gaussian noise (AWGN). Reconstruction under realistic conditions of continuously changing signal leads to larger artifacts. They are particularly pronounced in the lactate data and manifest as "bleeding" patterns in places of pyruvate distribution (Fig. 4.2). The first time frame is the most distorted and corresponds to the acquisition interval with the highest lactate-to-pyruvate ratio.

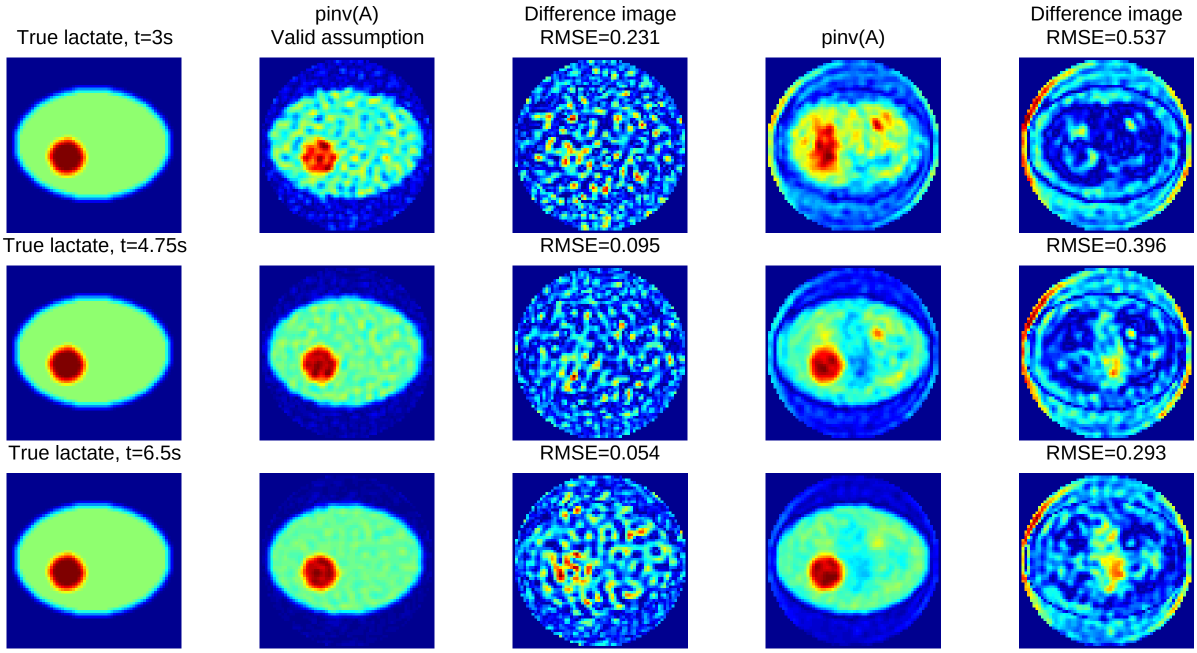

Figure 4.2.: True and reconstructed lactate images from the data with constant signal within 7 acquisitions, or varying according to the two-site exchange model (conversion rate $k_{P\to L} = 0.04\,\mathrm{s}^{-1}$)

The error between reconstructed images and the ground truth was quantified with the root-mean-square error metric (RMSE) on the entire interval of measurement and plotted versus time for these two cases of valid and invalid model assumptions (Fig. 4.3). To avoid ambiguity in terms, by valid we mean an assumption that is employed by LSCSI method and under which this algorithm yields the most accurate results, namely the assumption that the relative amounts of metabolites are fixed. Everywhere later we denote this case as valid. The maximum absolute reconstruction error for pyruvate data is 72 % smaller than the one for lactate.

Analogously, error plots were constructed for three different constant rates $k_{P\to L}$ of pyruvate-to-lactate conversion (Fig. 4.4). One can see that the images reconstructed from the measurements corresponding to the first half of the kinetic curve, before the end of injection and during the rapid pyruvate uptake, are the most error-prone, both for pyruvate and lactate data.

Another observation is that the average error for pyruvate is directly proportional to the conversion rate and vice versa, artifact level in the lactate images is inverse proportional to the conversion rate. Both results correlate with experimental observations when the data in the first time frames contain a larger portion of artifacts and spatial maps of lactate, which typically has a lower signal magnitude then pyruvate, also show worse SNR.

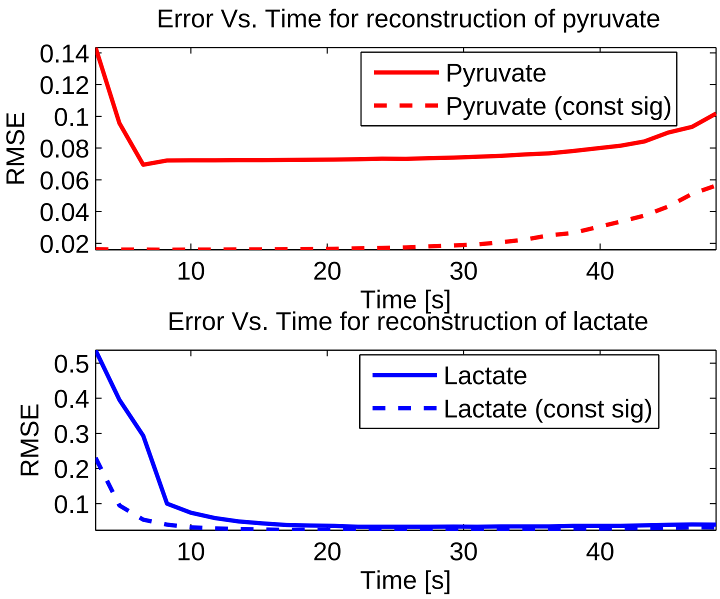

Figure 4.3.: Error between true and reconstructed images for cases with (solid line) and without (dashed line) signal change within 7 acquisitions (conversion rate $k_{P\to L} = 0.04\ \mathrm{s}^{-1}$)

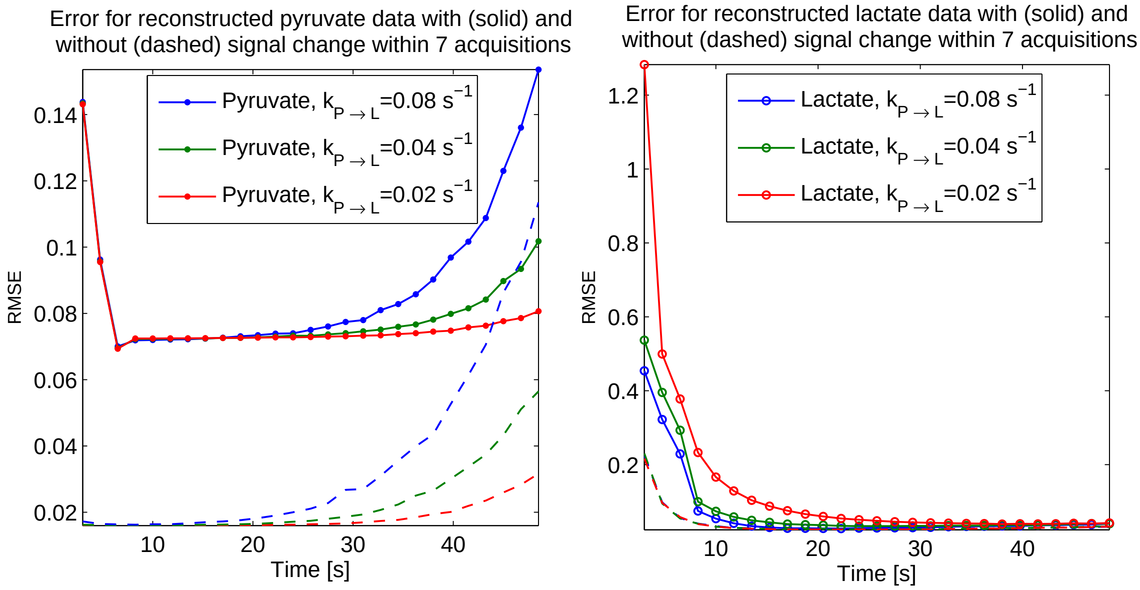

Figure 4.4.: Error between true and reconstructed images of pyruvate and lactate for 3 conversion rates in cases with (solid line) and without (dashed line) signal change within 7 acquisitions

4.2. Effect of Regularisation on Outcome of Reconstruction

4.2.1. Results for Simulated Data

In the following we present the results of iterative reconstruction with three different regularisation terms for simulated data. The performance of conventional reconstruction by inversion of the signal model matrix was compared with

1. Iterative reconstruction with Tikhonov regularisation term
2. Iterative reconstruction with the total variation (TV) penalty
3. Iterative reconstruction with the total generalised variation (TGV) penalty

Due to large number of simulated time steps comparison of method performance in terms of resulting image appearance is given for two time frames taken from the first and the second halves of kinetic curve (Fig. 4.5, 4.6) for pyruvate and lactate, respectively. For all images the root-mean-square errors (RMSE) between the reconstructed data and the ground truth are given.

General performance of reconstruction techniques on the entire interval of measurement can be deducted from the error plots (Fig. 4.7, 4.8).

Performance of reconstruction techniques can be additionally quantified in terms of their ability to preserve concentration difference of metabolites (here, pixel intensity difference) between distinct compartments as well as the weighted transfer rate, defined in Section 3.5 Eq. 3.28 as the integral of the metabolite (lactate) signal divided by the integral of the substrate (pyruvate) signal, which is equivalent to kinetic rate constant of pyruvate-to-lactate conversion divided by the effective relaxation rate for lactate. The pixel intensity change for two compartments of the pyruvate and lactate images is graphically represented in Figures 4.9, 4.10. From this data one can compute areas under all curves and consequently to make conclusion about how good the ratio between concentrations of pyruvate and lactate is preserved.

Table 4.1 summarises the performance of four reconstruction approaches in terms of RMSE averaged for three conversion rates separately for pyruvate and lactate, computational time, regularisation parameters, weighted transfer rate and the ratio of intensity for the first compartment to the second one. For the latter, data corresponding to three different locations within phantom was analysed. Noise performance was checked by inducing different levels of additive white Gaussian noise.

The best performance was achieved with total generalised variation (TGV) term, the results are equally better in reconstruction of the pyruvate and lactate images. The disadvantage is high time costs which can be reduced by decreasing the number of iterations and overall level of regularisation (Fig. 4.11).

TGV application requires two regularisation parameters α_1 and α_0. The ratio between them determines the balance between smoothing unregularities and edge preservation. The optimisation procedure was conducted in order to find the set of weighting factors which would yield the lowest error (Fig. 4.12).

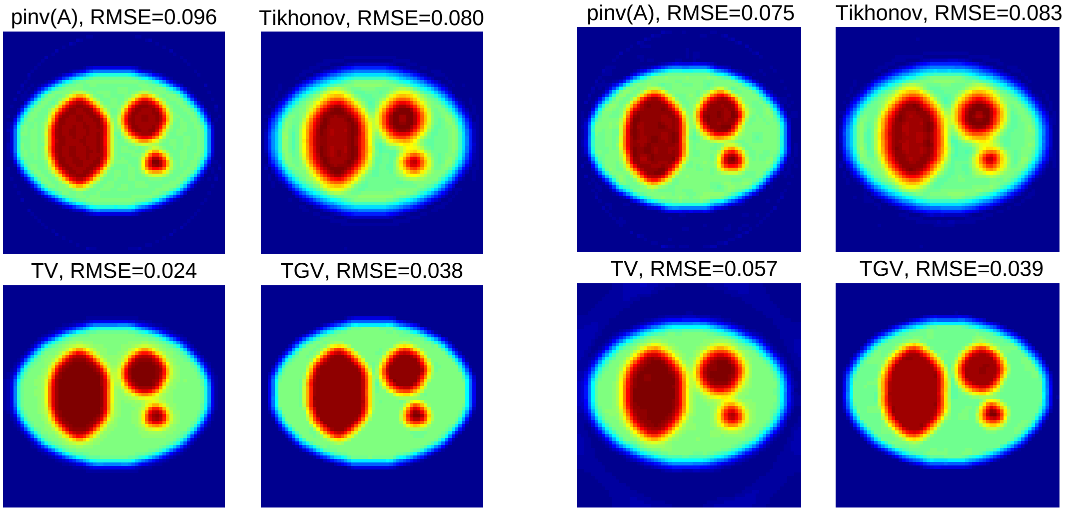

(a) Time frame = 2 (total 27)

(b) Time frame = 18 (total 27)

Figure 4.5.: Pyruvate image reconstructed with direct method of matrix inverse or using iterative reconstruction with Tikhonov, total variation (TV), total generalised variation (TGV) penalty terms

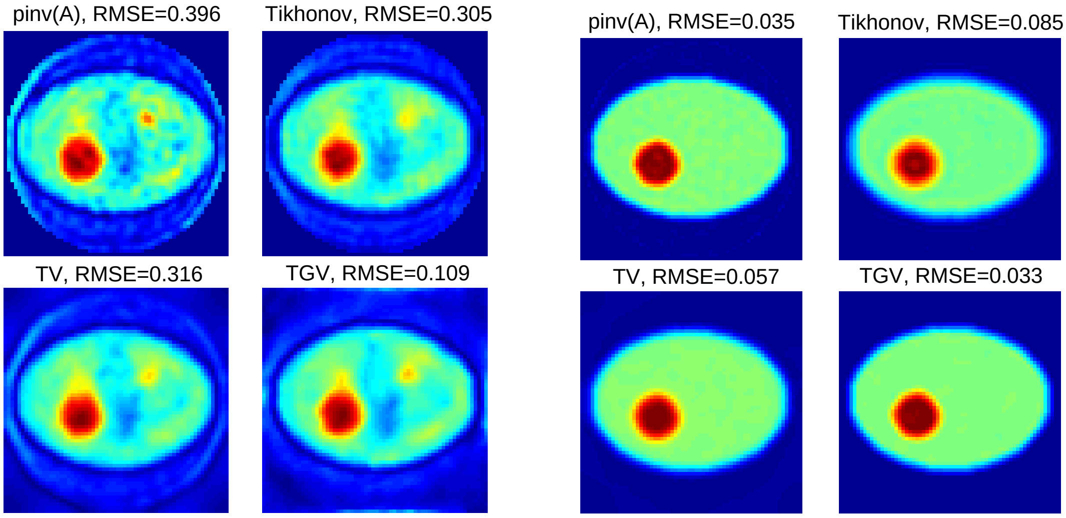

(a) Time frame = 2 (total 27)

(b) Time frame = 18 (total 27)

Figure 4.6.: Lactate image reconstructed with direct method of matrix inverse or using iterative reconstruction with Tikhonov, total variation (TV), total generalised variation (TGV) penalty terms

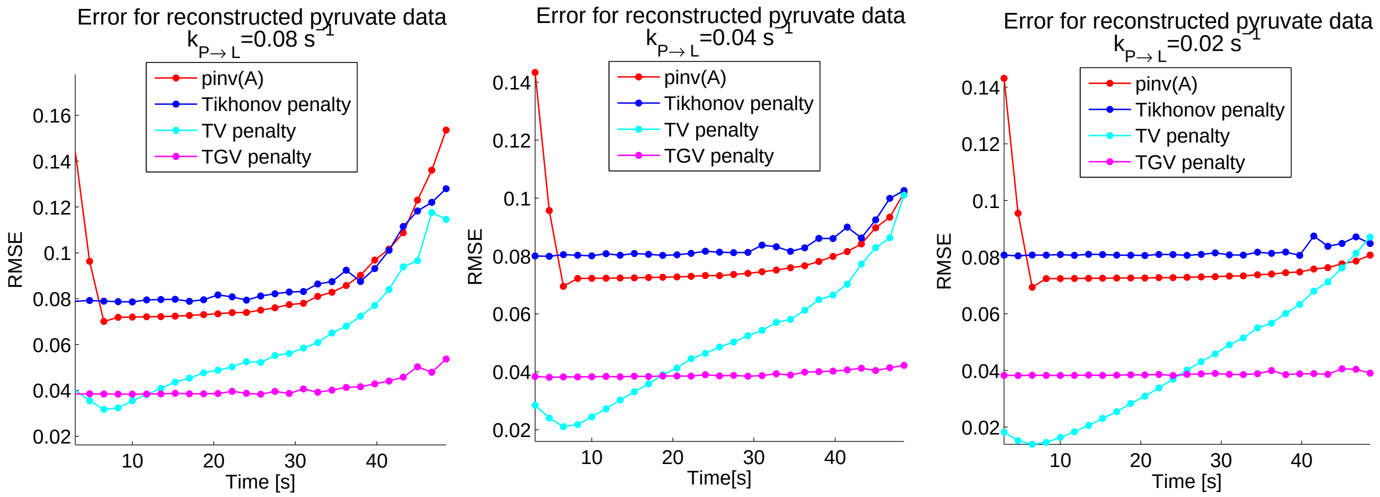

Figure 4.7.: RMSE versus time for reconstruction of pyruvate simulated data using different techniques for three conversion rates

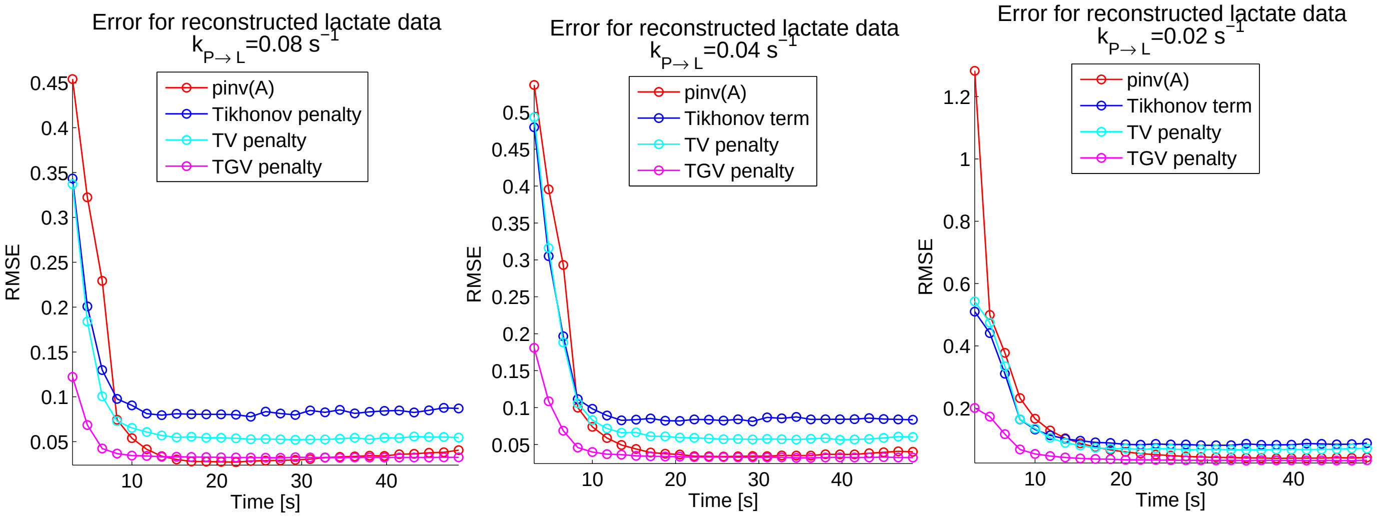

Figure 4.8.: RMSE versus time for reconstruction of lactate simulated data using different techniques for three conversion rates

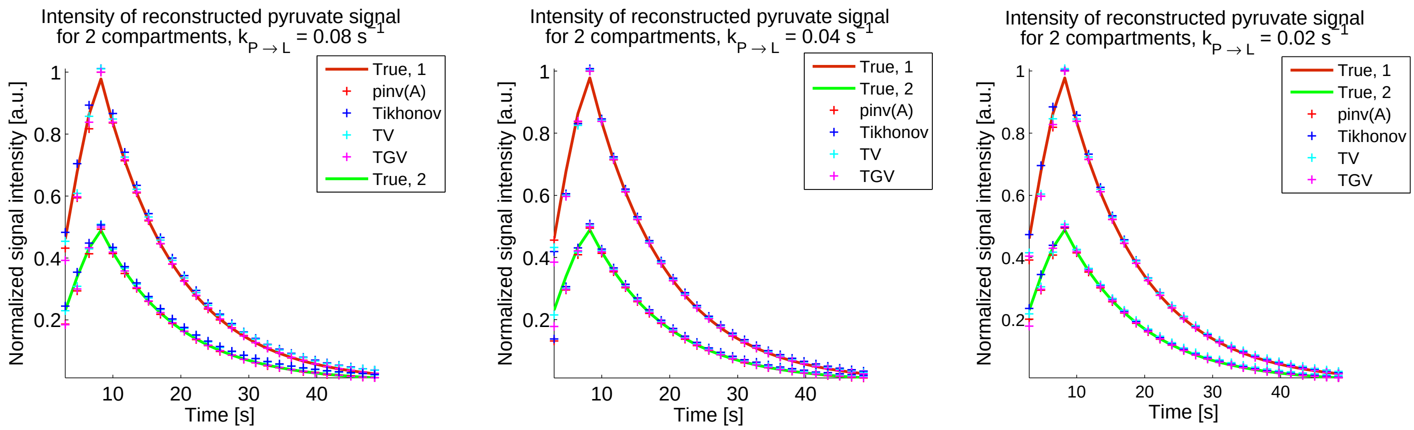

Figure 4.9.: Signal intensity change in two compartments for images of pyruvate reconstructed with different techniques for three conversion rates

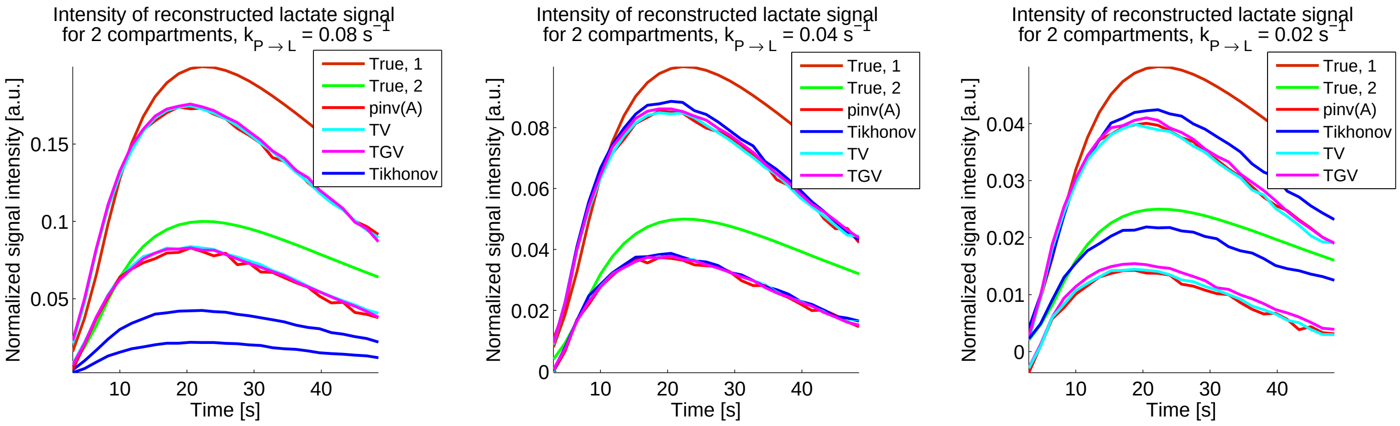

Figure 4.10.: Signal intensity change in two compartments for images of lactate reconstructed with different techniques for three conversion rates

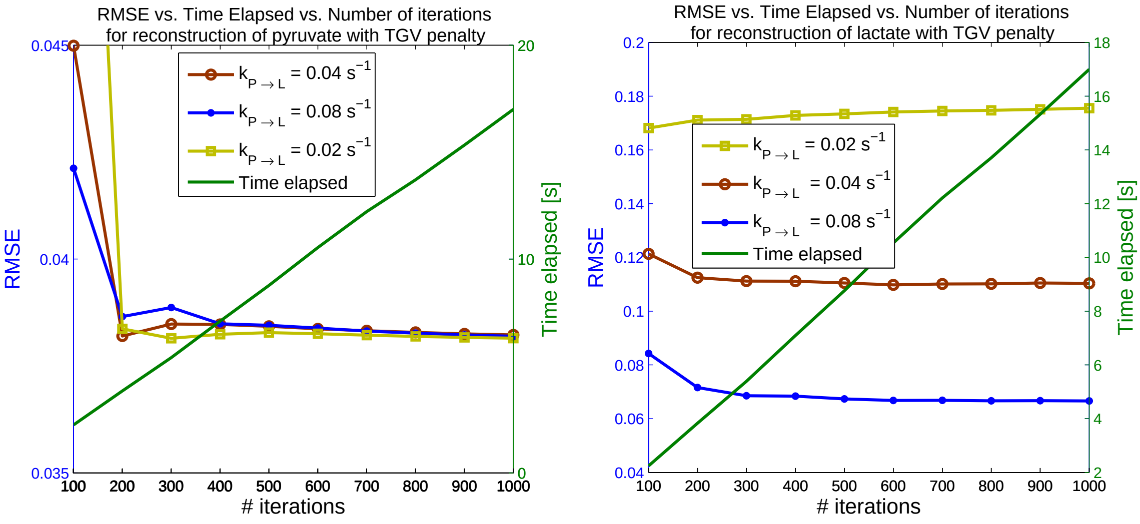

(a) (b)

Figure 4.11.: Dependency of RMSE and elapsed time from the number of iterations for pyruvate (a) and lactate (b) in iterative reconstruction with TGV constraint

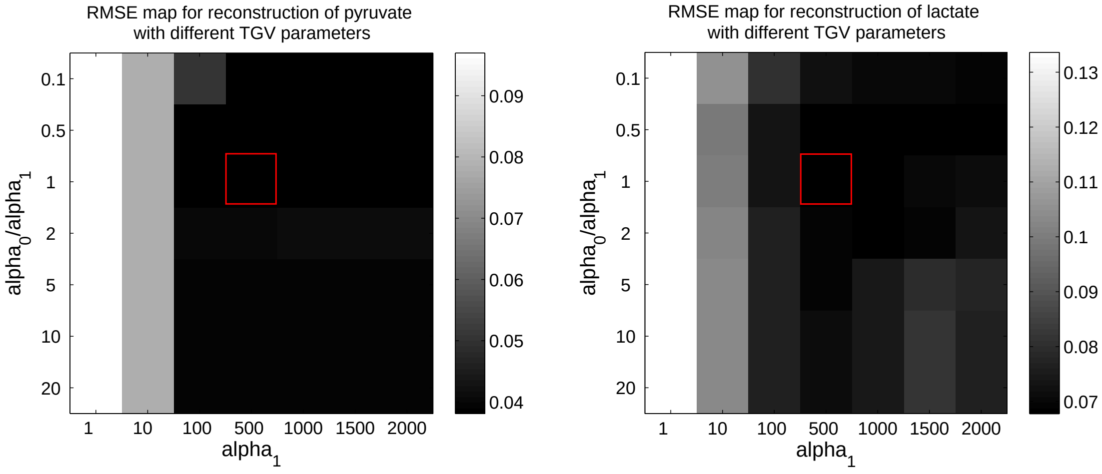

(a) (b)

Figure 4.12.: RMSE maps for optimisation of regularisation parameters in reconstruction of pyruvate (a) and lactate (b) with TGV constraint. The chosen combination is marked in red

Table 4.1.: Performance of conventional reconstruction by direct matrix inversion and iterative techniques with different regularisation terms.

	pinv(A)	Tikhonov	TV	TGV
RMSE	$0.082 \pm 0.019_{Pyr}$	$0.085 \pm 0.009_{Pyr}$	$0.051 \pm 0.023_{Pyr}$	$0.040 \pm 0.003_{Pyr}$
$(AWGN_{\sigma=5})$	$0.097 \pm 0.173_{Lac}$	$0.114 \pm 0.087_{Lac}$	$0.095 \pm 0.098_{Lac}$	$0.044 \pm 0.033_{Lac}$
RMSE	$0.093 \pm 0.038_{Pyr}$	$0.093 \pm 0.027_{Pyr}$	$0.057 \pm 0.033_{Pyr}$	$0.043 \pm 0.001_{Pyr}$
$(AWGN_{\sigma=10})$	$0.111 \pm 0.173_{Lac}$	$0.109 \pm 0.074_{Lac}$	$0.099 \pm 0.098_{Lac}$	$0.046 \pm 0.034_{Lac}$
Elapsed time	5.26 s	44.28 s	29.52 s	271.34 s
Parameters	-	$\alpha = 100$, $N_{it} = 100$	$\alpha = 100$, $N_{it} = 100$	$\alpha_1 = 500$, $N_{it} = 500$, $\alpha_0/\alpha_1 = 1$
Intensity ratio R	$2.049 \pm 0.022_{Pyr}$	$1.951 \pm 0.031_{Pyr}$	$1.942 \pm 0.044_{Pyr}$	$2.01 \pm 0.009_{Pyr}$
$(R_{true} = 2)$	$2.486 \pm 0.333_{Lac}$	$2.079 \pm 0.254_{Lac}$	$2.412 \pm 0.336_{Lac}$	$2.431 \pm 0.283_{Lac}$
Weighted transfer rate $k^i = k^i_{PL}/k_L$				
$k^1_{true} = 0.484$	0.406	0.095	0.389	0.409
$k^2_{true} = 0.242$	0.193	0.194	0.191	0.196
$k^3_{true} = 0.121$	0.091	0.093	0.084	0.095

*) The best and the worst performance characteristics are marked with green and red, respectively

Conclusion

From the comparison of resulting error for all reconstructed time series and image appearance we concluded, that iterative reconstruction with total generalised variation constraint (TGV) yielded the best results in these settings. It combines the advantages of the total variation (TV) penalty and is superior to it since it allows the higher flexibility in accounting for the image specifics. By adjusting two regularisation parameters it is possible to achieve moderate smoothing and preservation of edges, which is essential considering the nature of functional images. Evaluation of the second important metric, the weighted transfer rate, also proved that reconstruction with TGV constraint preserves the ratio of pyruvate to lactate signal in the most accurate way.

Iterative reconstruction with standard TV constraint showed a comparable or better performance than TGV only in the first time frames of reconstructed pyruvate data, in later frames – the error steeply grew. However, TV penalty outperformed the Tikhonov regularisation in all studies and is better from the point of time costs.

None of the reconstruction technique allows exactly restoring the quantitative information about pyruvate and lactate concentrations over time, the minimal error of 15 % was shown in reconstruction with TGV term.

The conducted simulations allowed to limit the number of regularisation techniques to be realised for the *in vivo* data. Out of considerations of better performance and limited applications in the processing of functional imaging data, that were documented in the literature until now, TGV term has been chosen for reconstruction of the experimental data. Both Tikhonov and TV regularisation showed suboptimal performance resulting in oversmoothing of the data and even further increased reconstruction error.

4.2.2. Results for Experiment with a Phantom

In the experiment with pyruvate-to-lactate conversion (see Section 3.4.3) two of three vials contained the same concentration of lactate dehydrogenase (LDH) and the one contained half the amount (Fig. 4.13). It resulted in different relative concentration levels of pyruvate to lactate for three vials and, correspondingly, different pixel intensities of these three regions in reconstructed images.

Time series of two-dimensional images of pyruvate and lactate distribution were reconstructed with conventional method (see Section 2.2.2), consisting of the least-squares chemical shift separation (LSCSI) followed by the non-uniform fast Fourier transform (NUFFT), and using iterative reconstruction with TGV constraint after the first stage of metabolite separation. Results were compared by qualitative assessment of the image appearance (Fig. 4.14, 4.15) and quantitatively by means of signal-to-noise ratio (SNR) computed separately for three regions of interest (three vials) (Fig. 4.16). By means of TGV penalty almost complete removal of background noise was achieved and circular shape of all objects with delineated edges was preserved.

Considerable improvement in SNR can be seen from graphics for all time series and vials. The increase of the mean SNR value for pyruvate is 74 %, 25 %, 25 % for upper, lower left and lower right vials, respectively, and analogous rates of SNR increase for lactate are 57 %, 43 % and 43 %. For both cases of higher concentrations of lactate (correspondingly, a higher pyruvate-to-lactate conversion rates) in two lower vials, SNR for these ROIs is larger in lactate images.

Pixel intensity was plotted separately to reflect the signal level for three vials in reconstructed images (Fig. 4.17). This showed that TGV reconstruction in not favourable for the resulting signal intensity. If one computes ratios of areas under respective curves of lactate and pyruvate, the results for two methods will be moderately different (see Table 4.2).

Table 4.2.: Weighted transfer rates for three vials.

	k (upper vial)	k (lower left vial)	k (lower right vial)
Conventional reconstruction	1.41	3.34	4.95
TGV	1.31	4.11	7.75

In order to evaluate whether both methods produce images consistent with underlying metabolic concentration levels, the ^{13}C NMR spectra acquired throughout the measurement were quantified. The resulting time courses represent the relative concentration levels of pyruvate and lactate for each time step (Fig. 4.18). From this data a reference weighted transfer rate can be computed as integral of lactate signal divided by the integral of pyruvate signal.

Analogous curves can be built from the reconstructed images simply by computing the composite pyruvate (lactate) pixel intensities for all three vials.

Figures 4.19 represent the relation between concentration level of the certain metabolite and its corresponding signal intensity in the image. The linear dependency can be observed for both cases of conventional reconstruction and iterative reconstruction with TGV constraint.

Table 4.3 contains the main performance features of two applied reconstruction techniques, which can be compared in terms of mean SNR of the resulting images, computational costs and transfer rate.

Table 4.3.: Performance of reconstruction using conventional NUFFT and iterative reconstruction with TGV constraint.

	NUFFT	TGV
SNR (mean value)	19.15_{Pyr} 51.75_{Lac}	29.89_{Pyr} 78.62_{Lac}
Elapsed time	16 s	1305.5 s
Parameters	-	$\alpha_1 = 100$, $N_{it} = 2000$, $\alpha_0/\alpha_1 = 20$
Weighted transfer rate $k=k_{PL}/k_L$ $k_{ref} = 1.93$	2.44	2.63

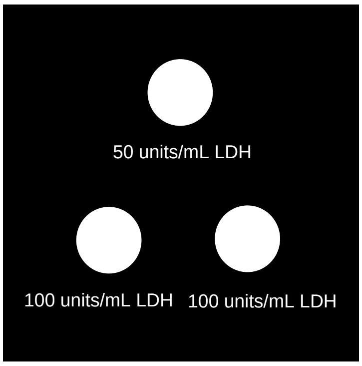

Figure 4.13.: Location of three vials in the experiment with specification of concentration of lactate dehydrogenase (LDH) in each vial

Conclusion

Iterative reconstruction with total generalised constraint (TGV) was applied for reconstruction of time series of pyruvate and lactate images from the data acquired in the experiment with a phantom. The reaction of pyruvate-to-lactate conversion was conducted with two different concentrations of lactate. As was initially predicted in simulations, SNR performance for pyruvate is getting worse with increasing level of lactate.

TGV reconstruction demonstrated good denoising properties and showed up to 70 % increase in SNR. In terms of preservation of ratio between overall concentrations of pyruvate and lactate, conventional method is still superior over iterative reconstruction (26 % error against 37 % error when compared with the transfer rate derived from quantified NMR spectra).

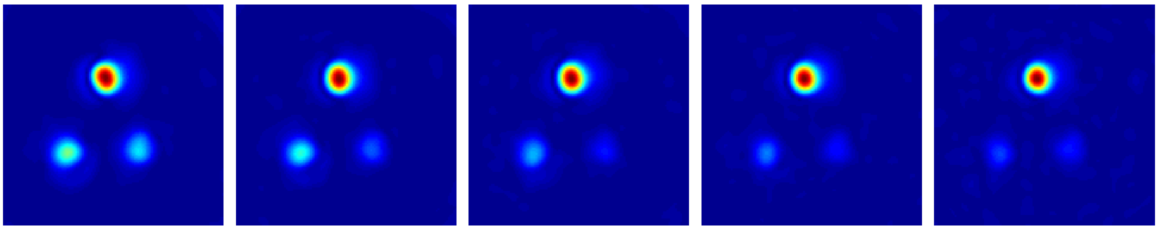

Pyruvate, 5 time steps

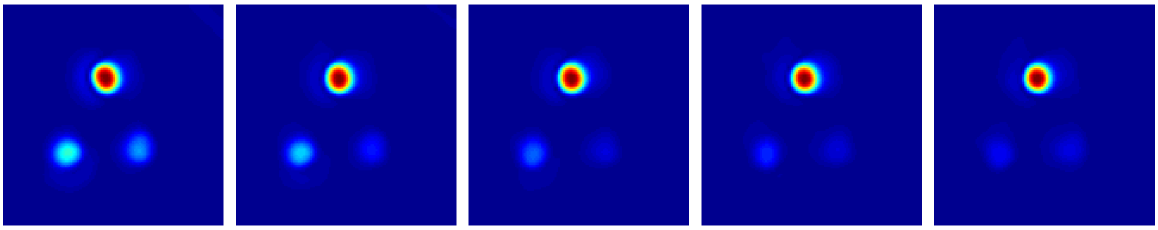

Pyruvate (TGV), 5 time steps

Figure 4.14.: Images of pyruvate distribution in 3 vials reconstructed with conventional method (upper row) and iterative reconstruction with TGV constraint (lower row)

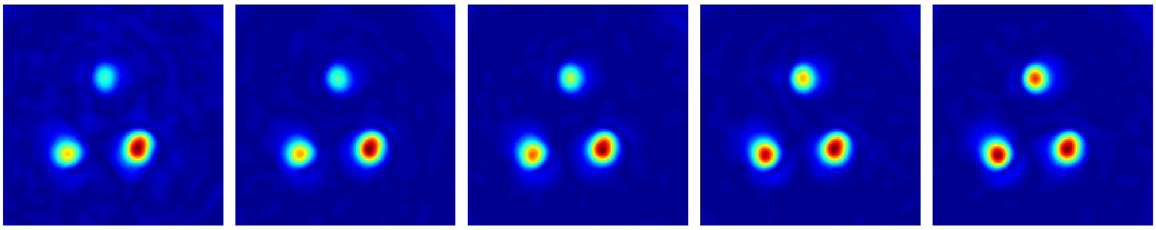

Lactate, 5 time steps

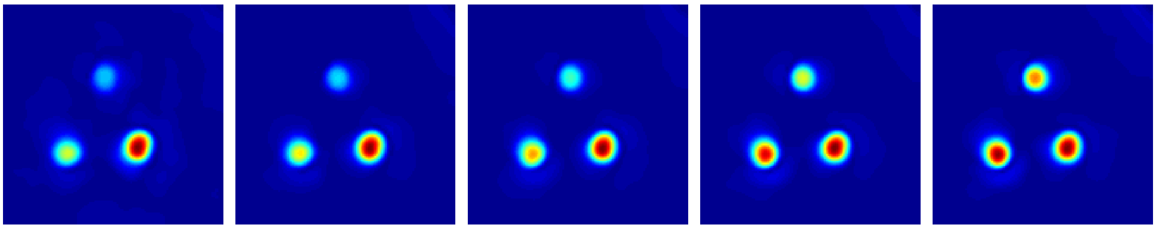

Lactate (TGV), 5 time steps

Figure 4.15.: Images of lactate distribution in 3 vials reconstructed with conventional method (upper row) and iterative reconstruction with TGV constraint (lower row)

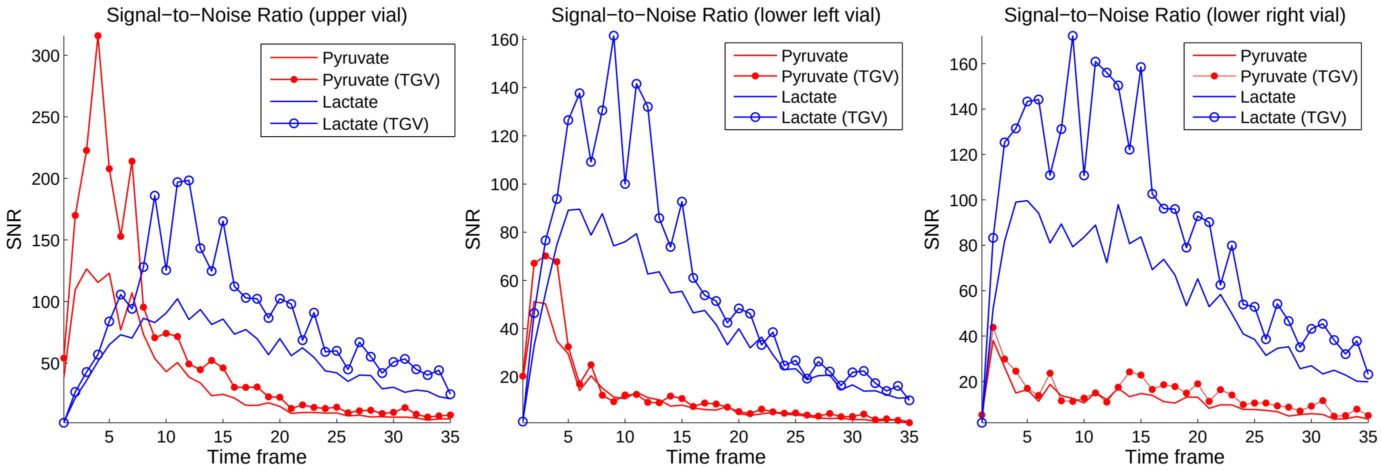

Figure 4.16.: Signal-to-Noise ratio (SNR) measured for three vials in images reconstructed with conventional method (solid line) and iterative reconstruction with TGV constraint (marked with filled and empty circles for pyruvate and lactate data, respectively)

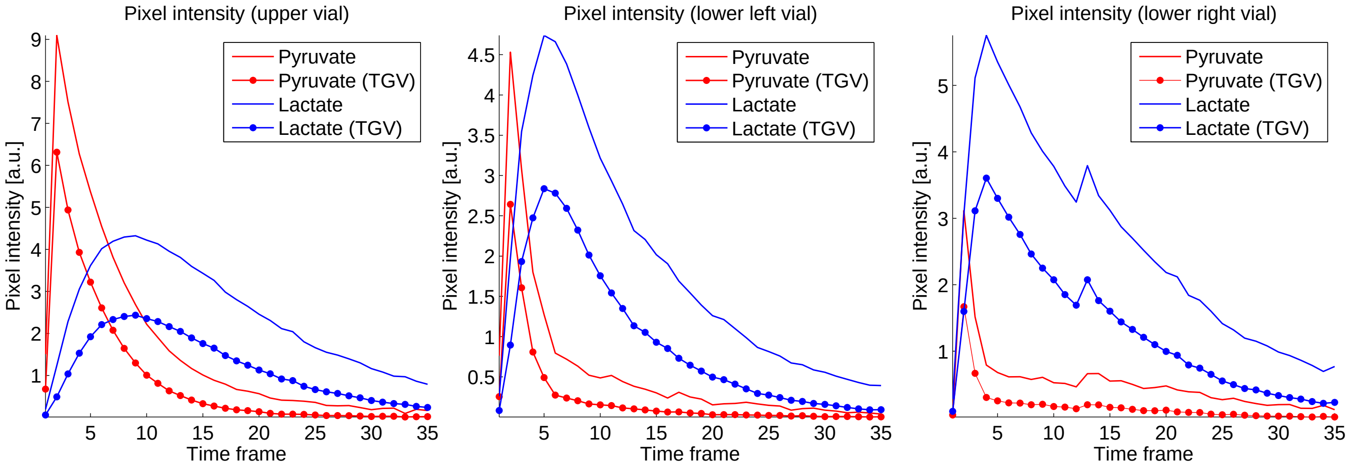

Figure 4.17.: Pixel intensity measured for three vials in images reconstructed with conventional method (solid line) and iterative reconstruction with TGV constraint (marked with filled circles)

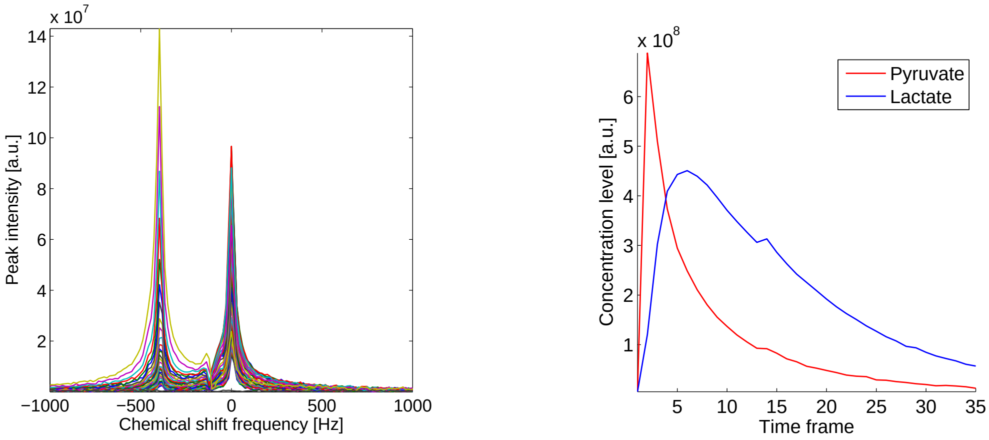

(a) (b)

Figure 4.18.: (a) ^{13}C NMR spectra of pyruvate and lactate for 35 acquisitions. (b) Metabolic time curves obtained by quantification of the spectra

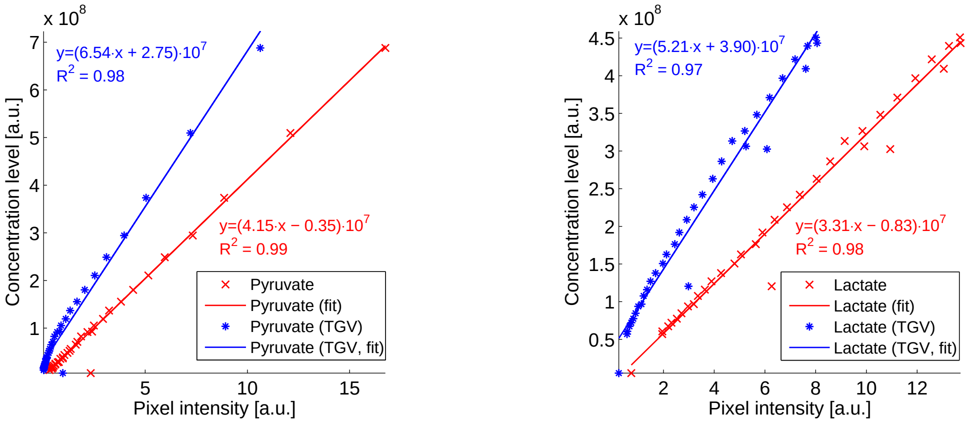

(a) (b)

Figure 4.19.: Concentration level versus pixel intensity and generated fit (a) for pyruvate and (b) for lactate sum images reconstructed with conventional method (in red) and iterative reconstruction with TGV constraint (in blue)

4.2.3. Results for *in vivo* Data

For validation of the chosen reconstruction approach, the data acquired during *in vivo* studies with healthy male outbred Wistar and tumour-bearing female inbred Fischer rats were used.

Selection of the regularisation parameters for the total generalised variation (TGV) minimisation functional (for the formulation see Section 2.2.3) was done by 1) performing reconstruction with different regularisation parameters α_1 and α_0 of the TGV, 2) constructing associated contrast and SNR maps and 3) assessment of the specified image quality metrics. This was done for images of four metabolites (pyruvate, alanine, pyruvate hydrate and lactate) at the same time frame to avoid large deviations due to metabolic dynamics.

Fig. 4.20 illustrates the way the image appearance was changing depending on the choice of the regularisation parameter α_1, and shows regions of interest (ROIs) used for the computation of SNR and contrast. Noise level was significantly reduced for larger values of α_1, while the important structures stayed preserved.

In Fig. 4.21 and 4.22 matrices of SNR and contrast values for different combinations of regularisation parameters are given. In each case, additionally the SNR and contrast values for image reconstructed with conventional method of non-uniform Fast Fourier Transform (NUFFT) are given for comparison. The trade-off between noise reduction and oversmoothing is well represented here: SNR is increasing for larger values of α_1, coefficient in TGV functional which forces minimisation of the intensity variations in homogeneous regions of the image and reduces the noise level. At the same time, it negatively affects the image contrast, which manifests in the increased blurring in gaps between distinct structures. The second coefficient, α_0, stands for accounting the higher-order image features such as edges and sharp structures. We could observe only subtle influence of this factor on the outcome of reconstruction and, typically, after this coefficient reached the certain value the further increase did not affect the image quality.

Plots presented in Fig. 4.23 illustrate the effect of the increasing number of iterations on SNR and contrast of the resulting images and allow avoiding unnecessary time expenses after acceptable SNR performance has been reached.

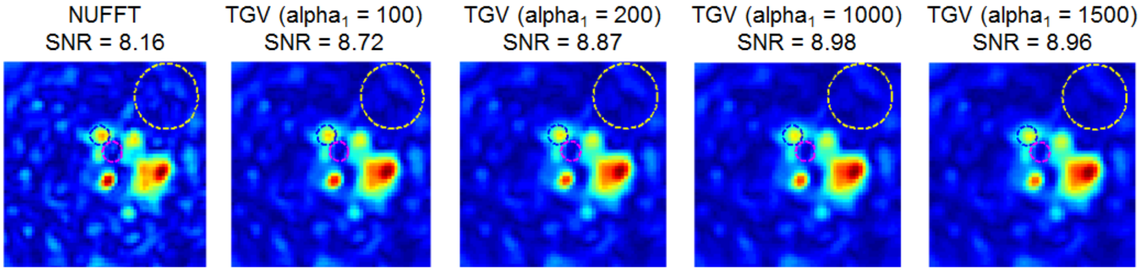

Figure 4.20.: Pyruvate hydrate reconstructed with conventional reconstruction (NUFFT) and TGV for different regularisation parameter α_1

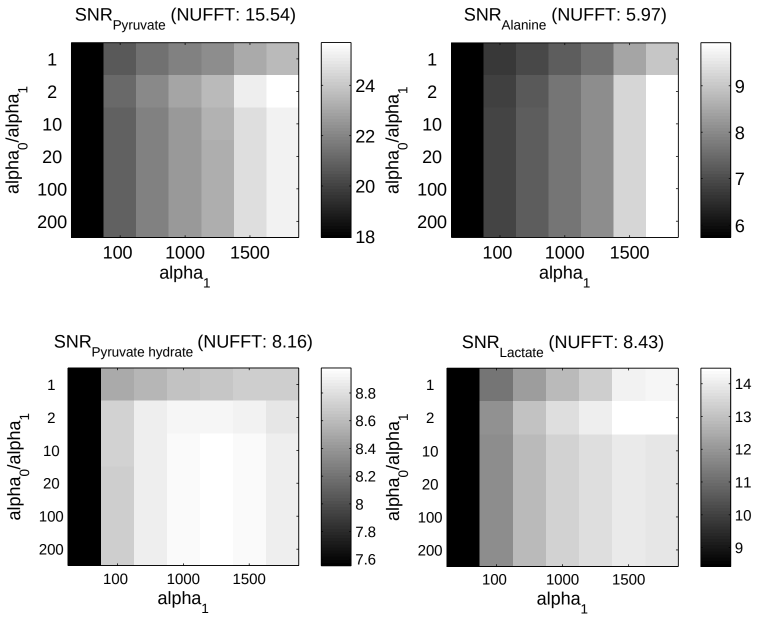

Figure 4.21.: Signal-to-noise ratio (SNR) maps for 4 metabolites reconstructed with TGV (SNR after conventional reconstruction (NUFFT) is given in brackets)

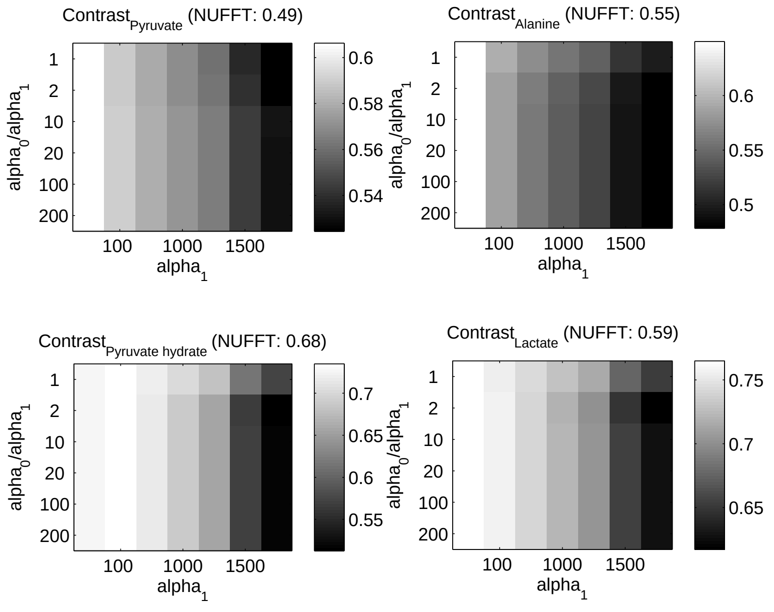

Figure 4.22.: Contrast maps for 4 metabolites reconstructed with TGV (SNR after conventional reconstruction (NUFFT) is given in brackets)

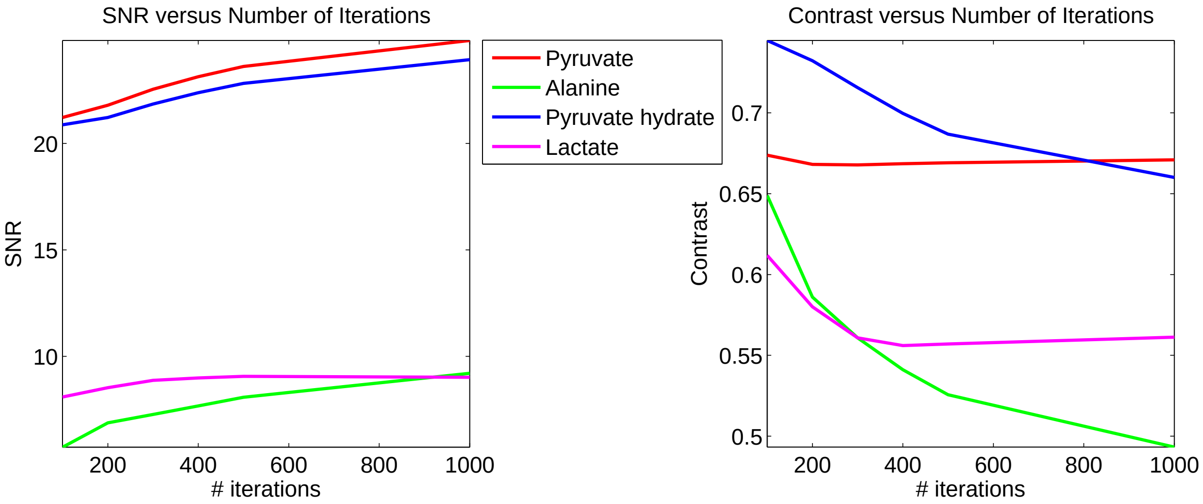

Figure 4.23.: Signal-to-noise ratio (SNR) and contrast for 4 metabolites for different number of iterations of TGV reconstruction

For reconstruction, parameters $\alpha_1 = 1000$, $\alpha_0/\alpha_1 = 10$ and number of iterations 400 were chosen.

Resulting images are presented in Fig. 4.25, 4.27 for two data sets. Images reconstructed with conventional non-uniform Fast Fourier transform (NUFFT) were compared with iterative reconstruction with total generalised variation (TGV) penalty and anatomical constraint in a form of the support mask. Reference morphological scans are given above each data set (Fig. 4.24, 4.26 for two studies).

Anatomy-based support mask can be derived also in a different way. By means of intensity thresholding followed by morphological operation of closing, it is possible to penalise even a larger portion of non-zero signal intensities outside the area of interest (see Section 3.2.2 for steps of mask derivation). The prior anatomy and generated mask are given in Fig. 4.28. Results for conventional reconstruction and iterative reconstruction with variational and anatomical constraints are presented in Fig. 4.29.

Despite the fact that pixel intensities in the resulting images are different for cases of NUFFT and TGV reconstruction, it has been proven that both approaches yield comparable results when the rate constant of pyruvate-to-lactate conversion was calculated. For such quantitative assessment, the metabolic time curves corresponding to the pixel intensity change in the centre of tumour and in kidney on reconstructed time series of pyruvate and lactate images were fitted with the two-site exchange model (see Section 3.3.1).

Estimated conversion rates k_{PL}, as shown in Fig. 4.33 were $0.0294\,\mathrm{s}^{-1}$ and $0.0237\,\mathrm{s}^{-1}$ for NUFFT and TGV reconstruction, respectively. Resulting values of estimated relaxation rates for these two respective cases are: $k_P = 0.1752\,\mathrm{s}^{-1}$ for the pyruvate and $k_L = 0.0834\,\mathrm{s}^{-1}$ for the lactate (NUFFT); $k_P = 0.2088\,\mathrm{s}^{-1}$ and $k_L = 0.0774\,\mathrm{s}^{-1}$ (TGV).

Close estimates were obtained from the fitting the model to the time curves obtained from quantification of the NMR spectra (Fig. 4.47): $k_P = 0.1242\,\mathrm{s}^{-1}$, $k_L = 0.0954\,\mathrm{s}^{-1}$, $k_{PL} = 0.0606\,\mathrm{s}^{-1}$. However, by no means it can be used as a reference since it reflects the behaviour of the composite pyruvate (lactate) signal in the entire considered slice, and from the reconstructed images the signal could be measured only locally.

Linear relation between concentration metabolite level and signal intensity of the reconstructed images is maintained with both reconstruction approaches and is illustrated in Fig. 4.31. Occurred deviations can be explained again by too rough approximation of the local metabolic changes in tumour with composite signal from the whole slice.

To demonstrate strong denoising properties of reconstruction when the TGV constraint is employed, the additive white Gaussian noise with zero mean and standard deviation of $5 \cdot 10^5$ was applied to both real and imaginary parts of the acquired signal prior to reconstruction.

Table 4.4 contains main performance characteristics for two reconstruction techniques. SNR was calculated for 5 different regions of interest within 2D slice and the conversion rates were computed from pyruvate-lactate signal in the middle of tumour and in the kidney.

Table 4.4.: Performance of reconstruction using conventional NUFFT and iterative reconstruction with TGV constraint.

	NUFFT	TGV
SNR (AWGN$_{\sigma=5\cdot10^5}$)	$37.57 \pm 12.96_{Pyr}$ $16.76 \pm 1.93_{Lac}$ $9.65 \pm 3.45_{Ala}$ $8.25 \pm 2.66_{PyrHydr}$	$47.25 \pm 16.41_{Pyr}$ $22.11 \pm 3.61_{Lac}$ $11.64 \pm 3.13_{Ala}$ $10.41 \pm 2.75_{PyrHydr}$
Elapsed time	5.65 s	519.85 s
Parameters	-	$\alpha_1 = 1000$, $N_{it} = 400$, $\alpha_0/\alpha_1 = 10$
Conversion rate $k_{PL}[s^{-1}]$	0.0294 (tumour) 0.0225 (kidney)	0.0237 (tumour) 0.0211 (kidney)
Estimated T_1 $T_{1P} = 1/k_P[s]$ $T_{1L} = 1/k_L[s]$	 5.7 (tumour), 8.4 (kidney) 12.1 (tumour), 14.4 (kidney)	 4.8 (tumour), 8.4 (kidney) 13.0 (tumour), 12.6 (kidney)

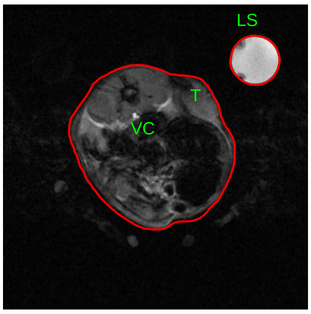

Figure 4.24.: T2-weighted ^{1}H-MR image of the slice through tumour

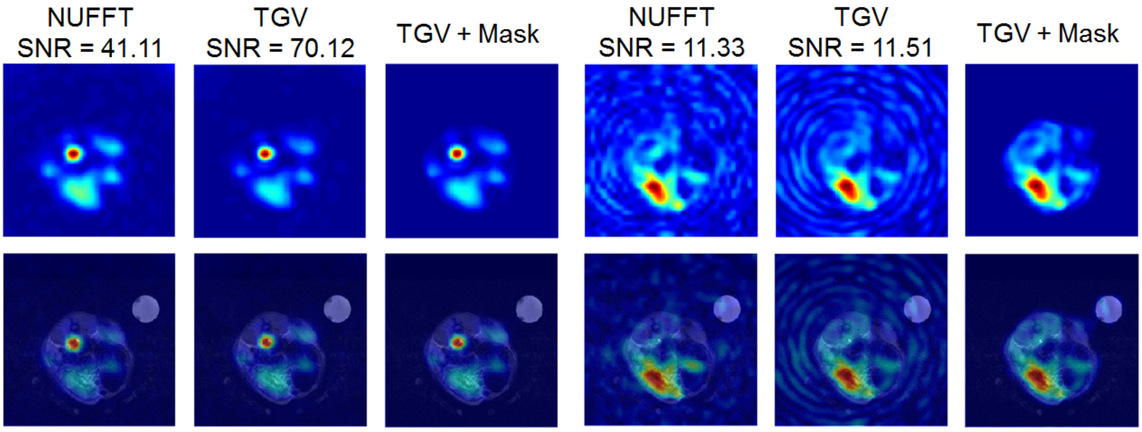

(a) Pyruvate (sum over 32 time frames)

(b) Alanine (sum over 32 time frames)

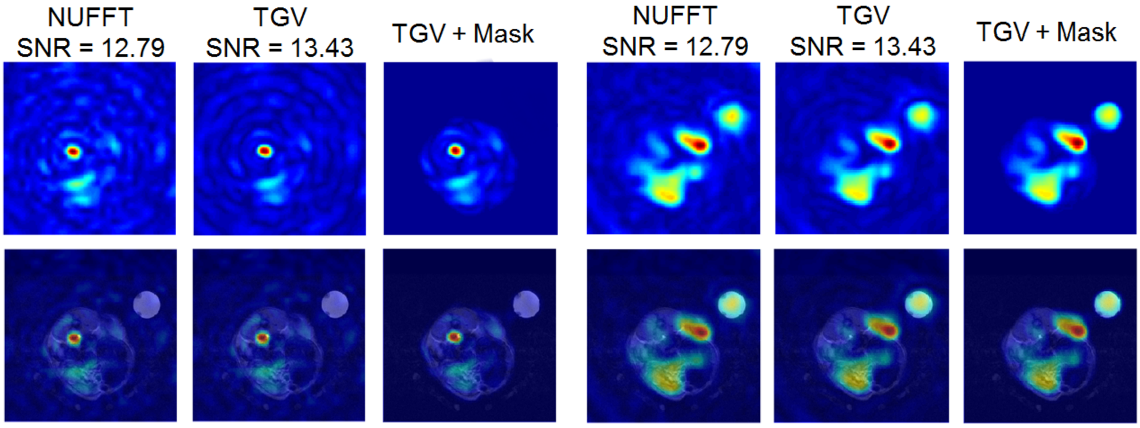

(c) Pyruvate hydrate (sum over 32 time frames)

(d) Lactate (sum over 32 time frames)

Figure 4.25.: Case study 1. (a) Metabolite images reconstructed with conventional method (NUFFT). (b) Iterative reconstruction with TGV constraint and active contour-based mask

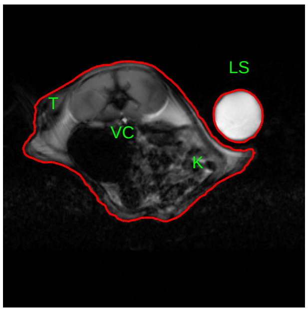

LS − lactate syringe; T − tumour; VC − vena cava; K − kidney

Figure 4.26.: T2-weighted ^{1}H-MR image of the slice through tumour and kidney

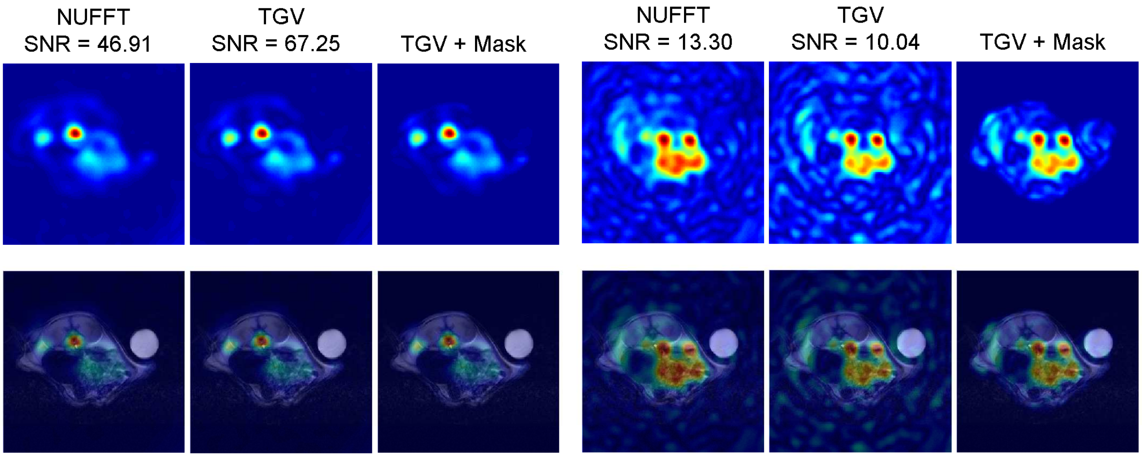

(a) Pyruvate (sum over 32 time frames)

(b) Alanine (sum over 32 time frames)

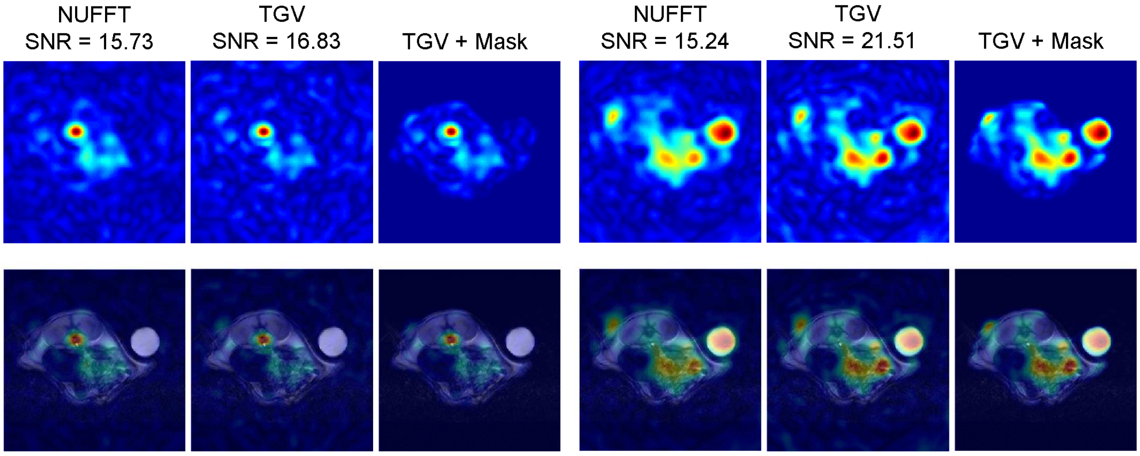

(c) Pyruvate hydrate (sum over 32 time frames)

(d) Lactate (sum over 32 time frames)

Figure 4.27.: Case study 2. (a) Metabolite images reconstructed with conventional method (NUFFT). (b) Iterative reconstruction with TGV constraint and active contour-based mask

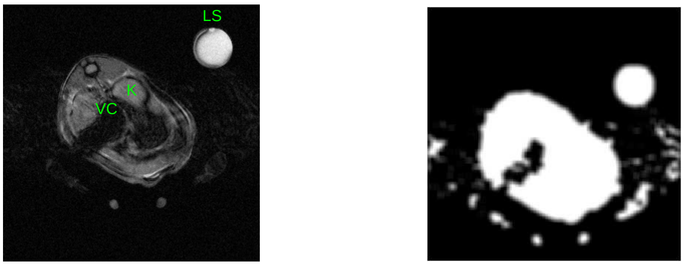

LS − lactate syringe; VC − vena cava; K − kidney

(a) Anatomy (b) Mask

Figure 4.28.: (a) T2-weighted ^{1}H-MR image of the slice through healthy rat kidney. (b) Derived support mask used for reconstruction

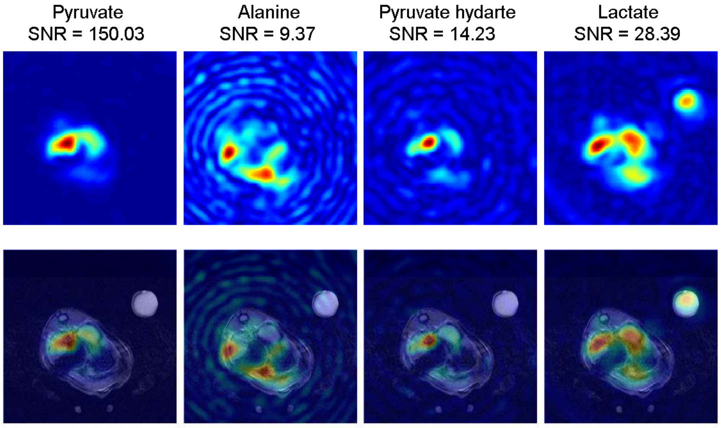

(a) NUFFT (time-average from 32 frames)

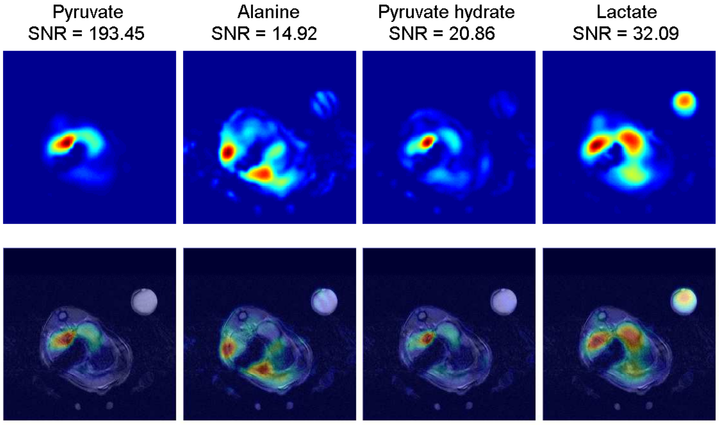

(b) TGV (time-average from 32 frames)

Figure 4.29.: Case study 3. (a) Metabolite images reconstructed with conventional method (NUFFT). (b) Iterative reconstruction with TGV constraint and threshold-based mask

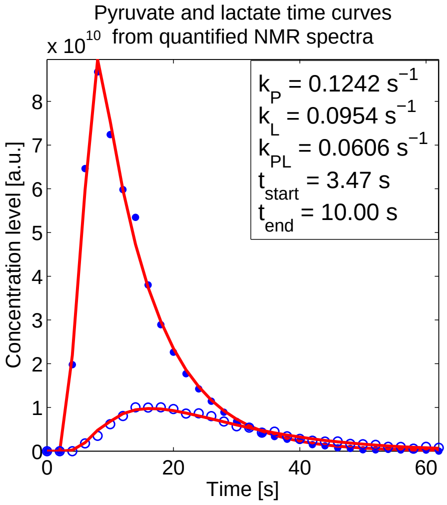

Figure 4.30.: Dynamic curves of metabolite levels in a slice centered on a rat kidney estimated from NMR spectra. Pyruvate data are represented by filled circles, lactate data are represented by empty circles. Estimated best fit lines are represented by red lines. Metabolic parameters, estimated from the model, are listed inside the plot

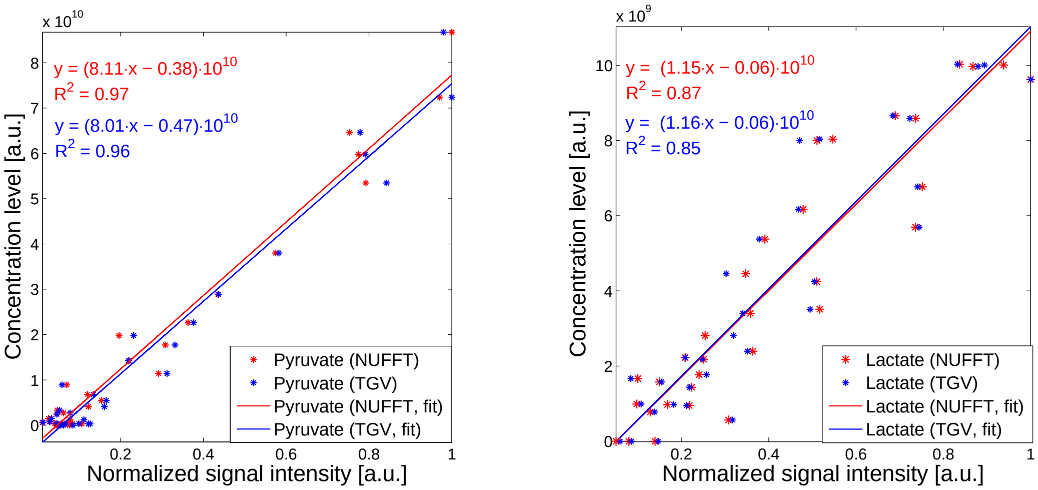

(a) Pyruvate

(b) Lactate

Figure 4.31.: Correlation between measured metabolite levels and reconstructed pixel intensity for pyruvate (a) and lactate (b). Data reconstructed with NUFFT and TGV approaches are represented with red and blue asterisks, respectively. Estimated best fit lines are represented by red and blue lines, respectively. The fit equations and the goodness of linear regression R^2 are given inside the plots

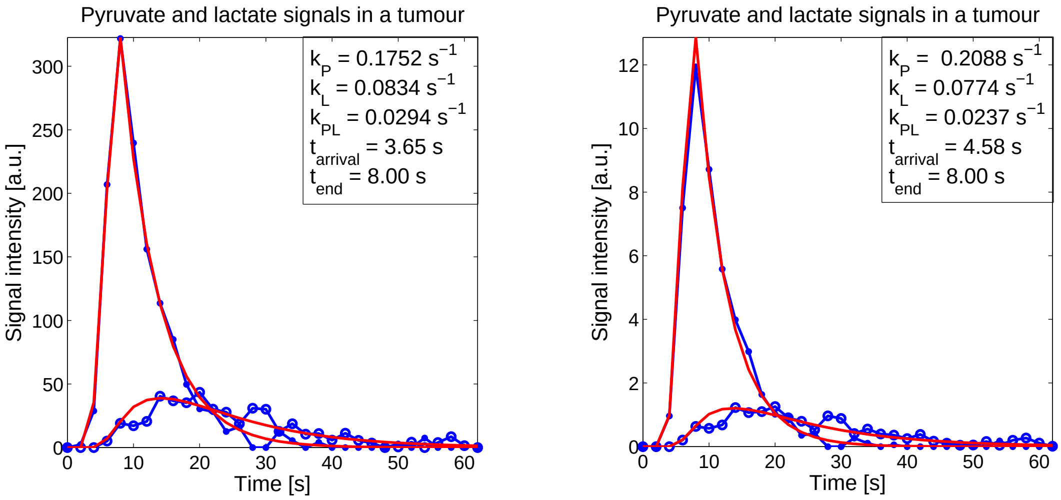

(a) NUFFT (b) TGV

Figure 4.32.: Dynamic curves of metabolite signal intensity in a tumour estimated from images of pyruvate and lactate reconstructed with NUFFT (a) and TGV (b). Pyruvate data are represented by filled circles, lactate data are represented by empty circles. Estimated best fit lines are represented by red lines. Metabolic parameters, estimated from the model, are listed inside the plots

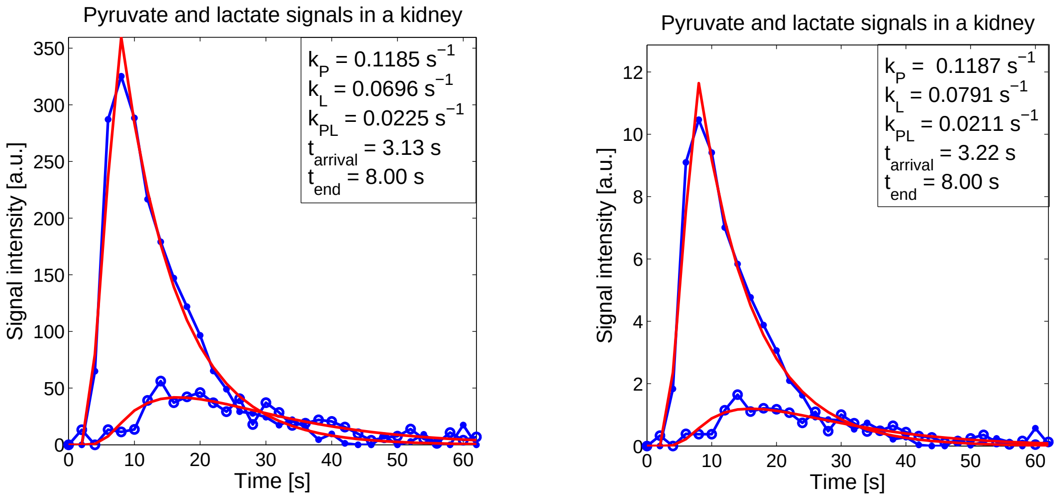

(a) NUFFT (b) TGV

Figure 4.33.: Dynamic curves of metabolite signal intensity in a kidney estimated from images of pyruvate and lactate reconstructed with NUFFT (a) and TGV (b). Pyruvate data are represented by filled circles, lactate data are represented by empty circles. Estimated best fit lines are represented by red lines. Metabolic parameters, estimated from the model, are listed inside the plots

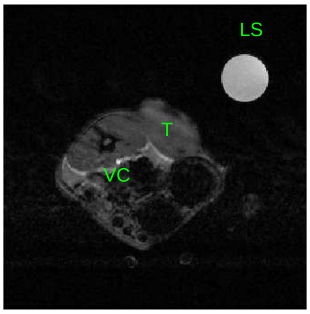

LS − lactate syringe; T − tumour; VC − vena cava

Figure 4.34.: T2-weighted ^{1}H-MR image of the slice through tumour

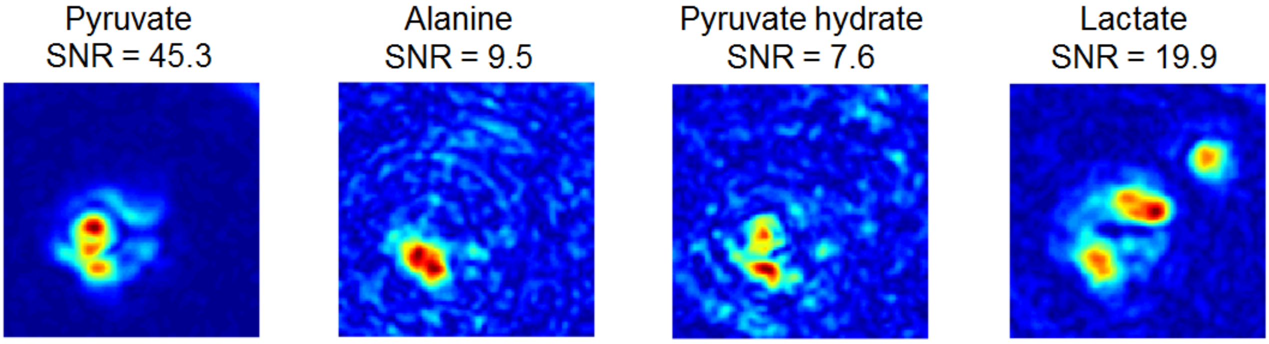

(a) NUFFT (sum images for 32 time frames)

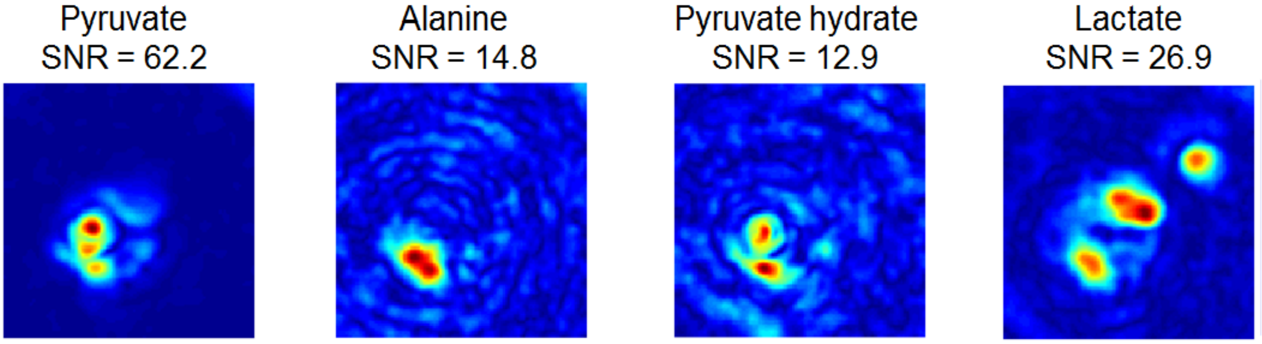

(b) TGV (sum images for 32 time frames)

Figure 4.35.: Noisy images of four metabolites reconstructed with conventional NUFFT technique (a) and iterative reconstruction with TGV constraint (b)

4.2.4. Discussion

Here we presented the results of iterative reconstruction with several regularisation terms. Methods were implemented and validated first in numerical simulations by means of root-mean-square error (RMSE) calculation between the reconstructed images and available ground truth, and afterwards were applied to the *in vivo* animal data. It has been shown that conventional reconstruction by means of direct inversion of signal model matrix results in errors, which manifest in characteristic Gibbs arifacts and more specific "bleeding patterns" in the lactate data in places of pyruvate distribution. Simulations for different rates of pyruvate-to-lactate conversion demonstrated that artifacts can be pronounced to a lesser or greater extent depending on the ratio of pyruvate to lactate peak signal height.

Root-mean square error (RMSE), signal-to-noise (SNR) and weighted transfer rates for pyruvate-to-lactate conversion ($Pyr \rightarrow Lac$) served the criteria for image quality assessment. The latter proved that quantification properties of reconstructed images were preserved with proposed iterative reconstruction. Conversion rates $k_{Pyr \rightarrow Lac}$ estimated from the signal evolution curves and corresponding to pyruvate (lactate) signal in local regions of reconstructed image were approximately the same for different reconstruction techniques, and in good correspondence with underlying metabolic concentration levels obtained from the quantified NMR spectra.

After numerical simulations two of three regularisation terms were rejected from the further consideration since they showed suboptimal performance and did not lead to any sound image quality improvement. TGV demonstrated clear advantage over both total variation (TV) and Tikhonov regularisation terms, it has equally good edge-preserving and denoising properties. Significantly longer computational times of TGV reconstruction did not become the obstacle for research purposes, but can be critical for the clinical workflow.

Total generalised variation (TGV) constraint was applied to *in vivo* data in the iterative reconstruction scheme and the SNR increase of up to 40 % as well as better delineation of structure borders and good denoising performance was achieved.

It has been shown that the balance between sufficient regularisation and preservation of image features is rather difficult to achieve and is controlled by two regularisation factors in case of TGV penalty function. In current implementation, the right amount of regularisation was determined by generating SNR and contrast maps for different sets of regularisation parameters and choosing the values corresponding to moderate SNR increase (noise removal) and desirably only a small decrease in the image contrast.

The critical part of such model-based *a priori* information induced by regularisation terms is that it may lead to losses in certain parts of the image, or the introduction of unwanted features [49]. It can be always checked in simulations, when the ground truth is available, but becomes a problem with experimentally acquired *in vivo* data. There only the expert knowledge of several reviewers can give an objective assessment of whether the diagnostically valuable content has been preserved or not.

4.3. Effect of Model-based Correction on Outcome of Reconstruction

4.3.1. Results for Simulated Data

The goal of this simulation was to investigate how the results of conventional reconstruction by inversion of the signal model matrix would change if the spectral encoding operator is extended with additional correcting factors. To obtain them in simulation settings, the original signal curves were corrupted with additive white Gaussian noise with zero mean and standard deviation σ=1.5 and σ=0.5 for pyruvate and lactate curves, respectively. Then the values between each 8-th sample of these newly built time curves were either linearly interpolated or fitted using the two-site exchange model (Fig. 4.36) and later inserted into the chemical shift imaging encoding matrix (for exact method see Section 3.3.1). Time curves representing metabolic concentration levels over time are experimentally obtained by quantifying the spectra, reconstructed from FID signal throughout the measurement.

Performing the linear approximation to the time curve to find the correcting factors is faster and does not require any additional computations, while kinetic modelling implies solving the system of non-linear equations for unknown kinetic rates in order to generate the fit.

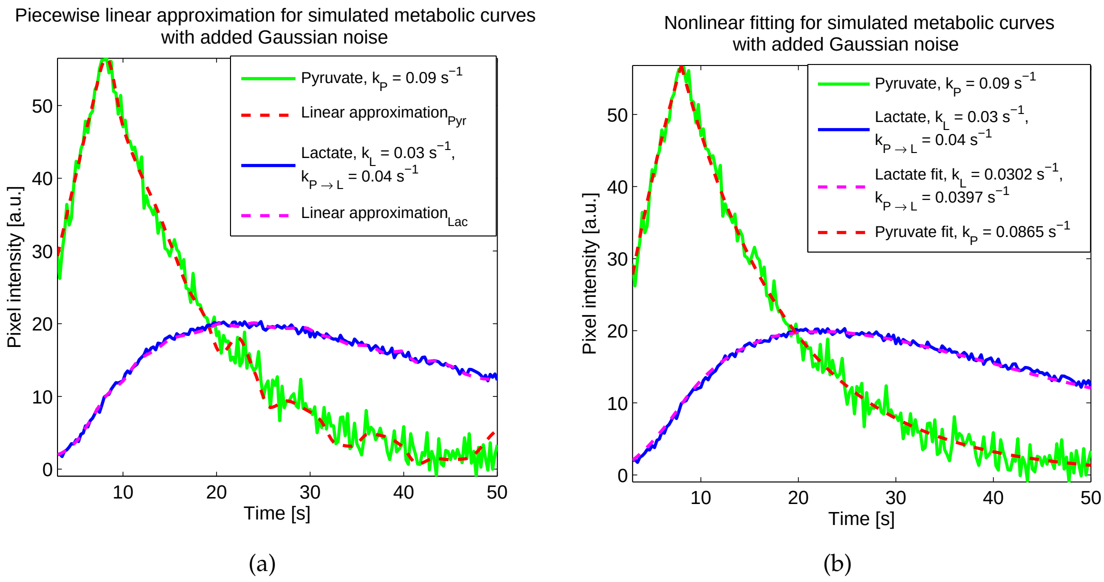

(a) (b)

Figure 4.36.: Approximation to simulated metabolic signal curves corrupted with Gaussian noise by means of linear interpolation (a) and fitting with the two-site exchange model (b)

Reconstructed images were compared with conventional approach of direct inverse of the signal model matrix without correction and reconstruction under the valid assumption of LSCSI method. Figures 4.37 and 4.38 demonstrate the effect of such correction on the outcome of reconstruction for a single time frame for pyruvate and lactate, respectively.

The difference images for each case reflect the presence of artifacts on resulting images.

The error behaviour for all time frames and for three different pyruvate-to-lactate conversion rates were plotted versus time (Fig. 4.39, 4.40). General observation that can be made based on the constructed error plot is that reconstruction after model-based correction yields better results than the conventional one no matter how the correcting factors were obtained. However, outcome of reconstruction when the linear approximation to the time curves was performed is less predictable since the observed error shows larger deviations from the mean value.

Signal intensities for two compartments of reconstructed images were compared with true intensities and plotted versus time (Fig. 4.41, 4.42). For pyruvate data, the conventional reconstruction is better than any of two proposed methods in terms of quantification. For lactate data, the pixel intensity curves, corresponding to images reconstructed with a proposed technique, are closer to the original ones and with correcting factors taken from the fitted curves the results are more stable.

Both approaches were evaluated under different noise levels and the intensity level change was compared for different pixels within two compartments. On its basis, the ratio between the curves and the transfer rate were computed. The results are summarised in Table 4.5.

Table 4.5.: Performance of reconstruction with method of direct inverse of conventional signal model matrix and the modified one using two approaches to compute correcting factors.

	pinv(A)	Linear approximation	Kinetic modelling
RMSE	$0.082 \pm 0.019_{Pyr}$	$0.047 \pm 0.028_{Pyr}$	$0.046 \pm 0.025_{Pyr}$
($AWGN_{\sigma=5}$)	$0.097 \pm 0.173_{Lac}$	$0.052 \pm 0.038_{Lac}$	$0.044 \pm 0.029_{Lac}$
RMSE	$0.093 \pm 0.038_{Pyr}$	$0.072 \pm 0.071_{Pyr}$	$0.066 \pm 0.055_{Pyr}$
($AWGN_{\sigma=10}$)	$0.111 \pm 0.173_{Lac}$	$0.080 \pm 0.052_{Lac}$	$0.075 \pm 0.053_{Lac}$
Elapsed time	6.96 s	7.50 s	7.42 s
Intensity ratio R	$2.049 \pm 0.022_{Pyr}$	$1.977 \pm 0.048_{Pyr}$	$1.950 \pm 0.030_{Pyr}$
($R_{true} = 2$)	$2.486 \pm 0.333_{Lac}$	$2.261 \pm 0.148_{Lac}$	$2.254 \pm 0.114_{Lac}$
Weighted transfer			
rate $k^i = k^i_{PL}/k_L$			
$k^1_{true} = 0.484$	0.406	0.356	0.375
$k^2_{true} = 0.242$	0.193	0.188	0.185
$k^3_{true} = 0.121$	0.091	0.095	0.097

*) The best and the worst performance characteristics are marked with green and red, respectively

Conclusion

In these simulation studies the effect of the model-based correction was investigated and results were compared with conventional reconstruction. Image appearance, presence of artifacts on resulting images, root-mean-square error between reconstructed data and the ground truth as well as weighted transfer rate and ratio between pyruvate (lactate) signal intensities of two compartments served as metrics for quality assessment of reconstruction approaches.

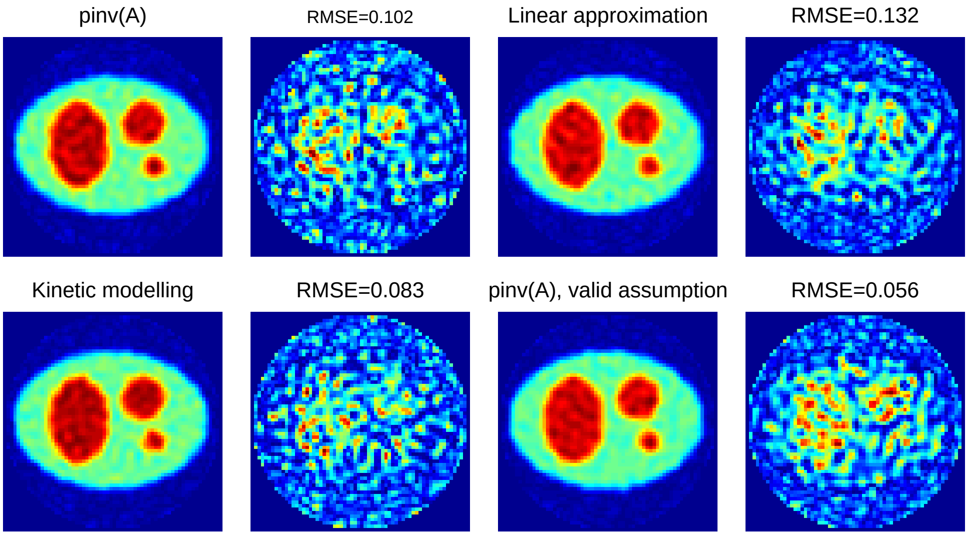

Figure 4.37.: Pyruvate simulated data reconstructed with method of direct inverse of conventional model matrix and the corrected one, using two approaches to approximate the time curves

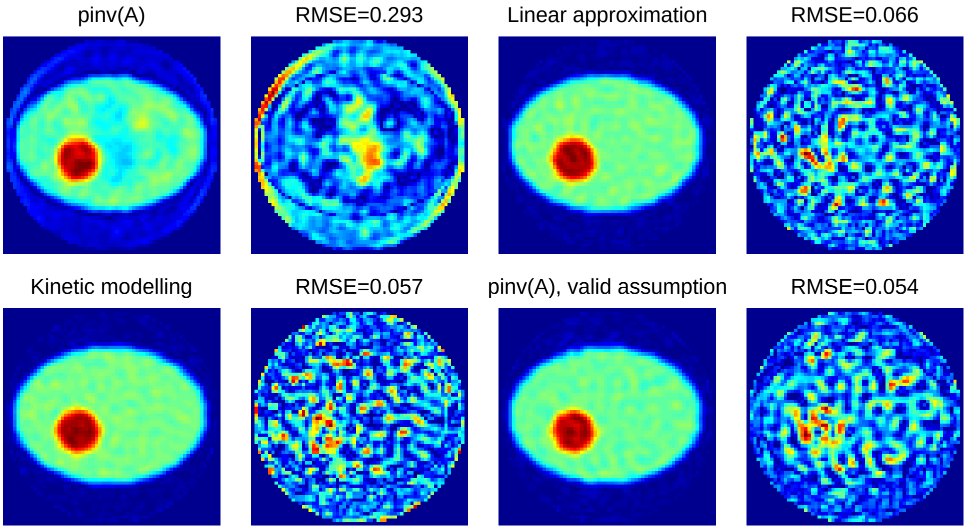

Figure 4.38.: Lactate simulated data reconstructed with method of direct inverse of conventional model matrix and the corrected one, using two approaches to approximate the time curves

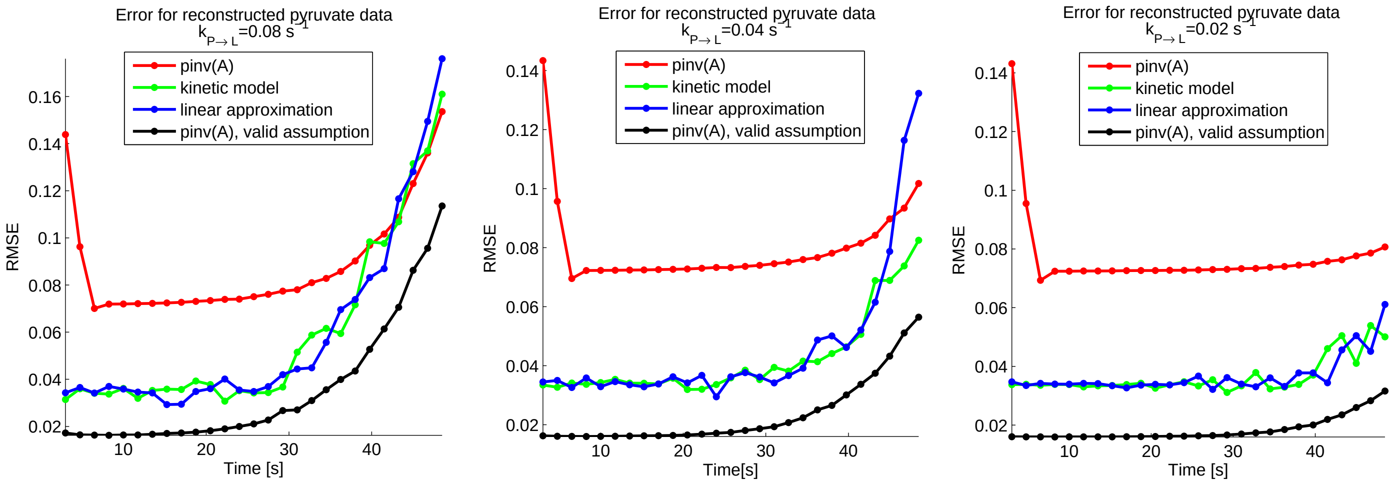

Figure 4.39.: RMSE versus time for pyruvate simulated data reconstructed with method of direct inverse of conventional model matrix and the corrected one, using two approaches to approximate the time curves

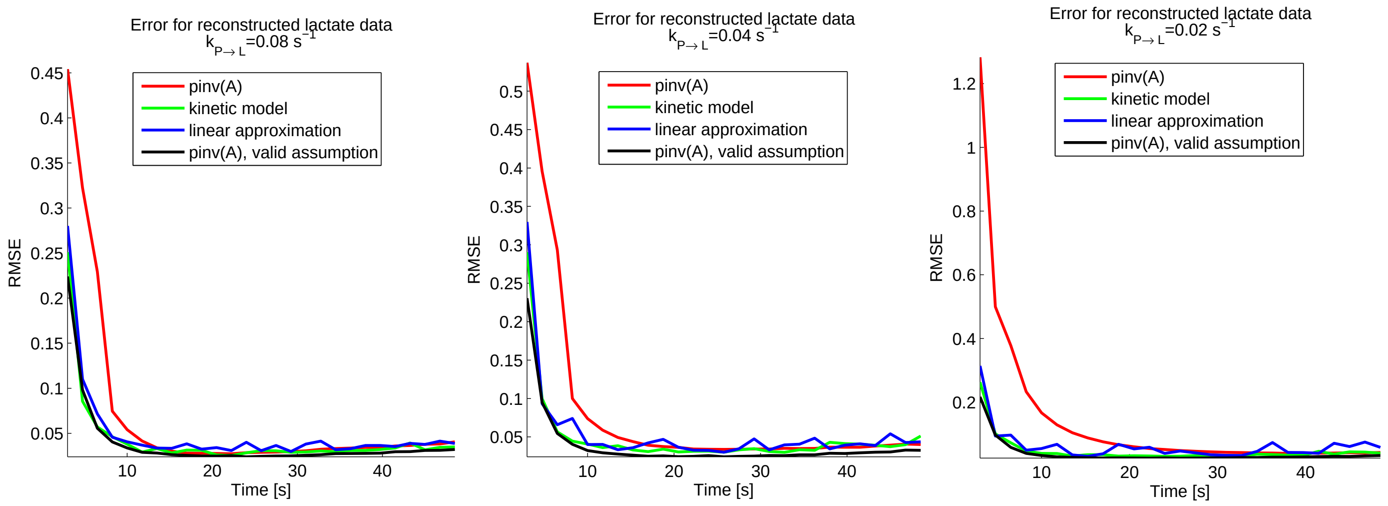

Figure 4.40.: RMSE versus time for lactate simulated data reconstructed with method of direct inverse of conventional model matrix and the corrected one, using two approaches to approximate the time curves

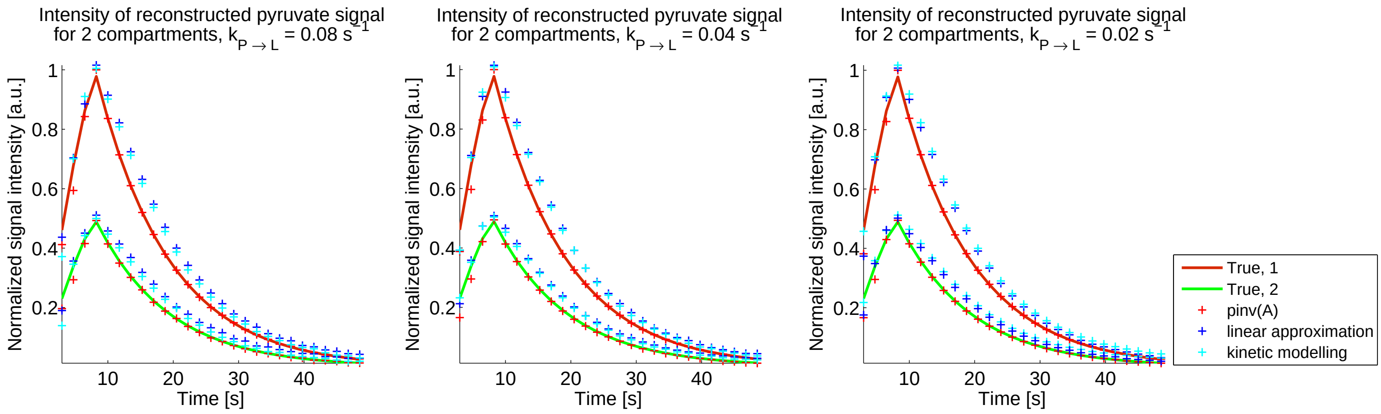

Figure 4.41.: Signal intensity change in two compartments for images of pyruvate reconstructed with method of direct inverse of conventional model matrix and the corrected one, using two approaches to approximate the time curves for three conversion rates

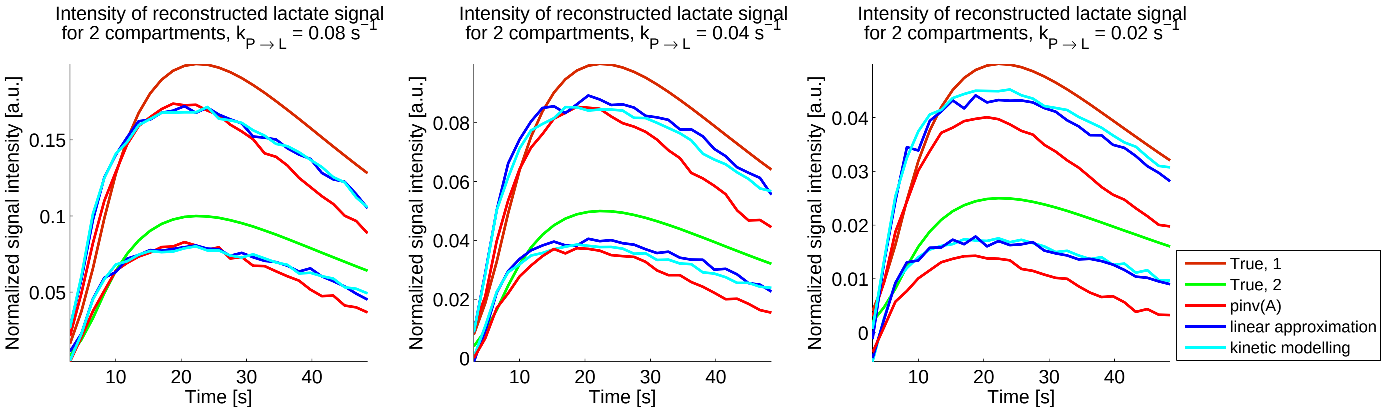

Figure 4.42.: Signal intensity change in two compartments for images of lactate reconstructed with method of direct inverse of conventional model matrix and the corrected one, using two approaches to approximate the time curves for three conversion rates

The outcome of the proposed reconstruction was different for two methods of deriving the correcting factors and results showed that kinetic modelling is the best approach for this purpose. RMS error was the lowest in this case, the pixel intensity curves for reconstructed images did not exhibit large fluctuations. Jointly estimated kinetic rates of pyruvate-to-lactate conversion and signal decay rates may present additional interest in this case.

4.3.2. Results for *in vivo* Data

Numerical simulations showed the potential to achieve substantial artifact reduction in images reconstructed with modified spectral encoding matrix. So this method, further on denoted as the First-Order Correction (FOC), was applied to the real *in vivo* data and here the results are presented.

To obtain components of the correction matrix, which complements conventional spectral encoding matrix and compensates for the average signal evolution within the slice, the NMR spectra were quantified and fitted with the two-site exchange model. Figures 4.43 (a,b) and 4.45 illustrate the actual anatomical scans and both measured and fitted metabolic time curves for two different sets of animal data. Images before and after correction are shown in Fig. 4.44, 4.46.

Flip angles of 10° and 90° were used to acquire two respective data sets, echo time of 0.025 ms and repetition time of 250 ms.

Analysis of the results presented in Fig. 4.44 (b), obtained by means of reconstruction after the first-order correction of spectral encoding matrix was performed, and comparison with Fig. 4.44 (a), prior to correction, allows to draw some conclusions regarding the achieved image improvement. The first image shows elevated pyruvic signal in kidney, the signal-to-noise ratio (SNR) however decreased due to appeared background noise. Significant artifact reduction was reached in the alanine data (+ 26 % SNR). ”Bleeding” patterns, clearly observed after conventional reconstruction, disappeared in the corrected images. Pyruvate hydrate, similarly to pyruvate behaviour, shows gain in signal in kidneys and at the same time increased noise level. The lactate image in (b) has much smoother background signal after correction than before (+ 10 % SNR).

Metabolite images in Fig. 4.46 (a,b) serve as another example of how the first-order correction changes the outcome of reconstruction. In all images one can observe increased signal in organs (in this case study specifically in kidney) as well as in tumour. SNR level for pyruvate, alanine, lactate data show the increase respectively of 11 %, 5 %, 12 % compared to the conventional reconstruction.

Table 4.6 contains the estimated values of SNR and relevant kinetic rates calculated from the pixel intensity curves in the specified local regions on reconstructed images. To avoid large deviations between different studies here the kinetic rate estimates from one reconstructed set of images are given (see the source images in Fig. 4.46). SNR was calculated from four processed data sets and averaged for each metabolite.

Table 4.6.: Reconstruction performance with conventional LSCSI method for metabolite separation and the first-order correction.

	LSCSI	FOC
SNR (mean value)	$96.25_{Pyr}, 16.29_{Lac}$ $10.37_{Ala}, 18.43_{PyrHydr}$	$79.28_{Pyr}, 19.18_{Lac}$ $12.70_{Ala}, 16.74_{PyrHydr}$
Elapsed time	6.15 s	10 s
Conversion rate $k_{PL}[s^{-1}]$	0.0294 (tumour) 0.0225 (kidney)	0.0282 (tumour) 0.0383 (kidney)
Estimated T_1		
$T_{1P} = 1/k_P[s]$	5.7 (tumour), 8.4 (kidney)	5.4 (tumour), 10.3 (kidney)
$T_{1L} = 1/k_L[s]$	12.01 (tumour), 14.4 (kidney)	12.7 (tumour), 10.8 (kidney)

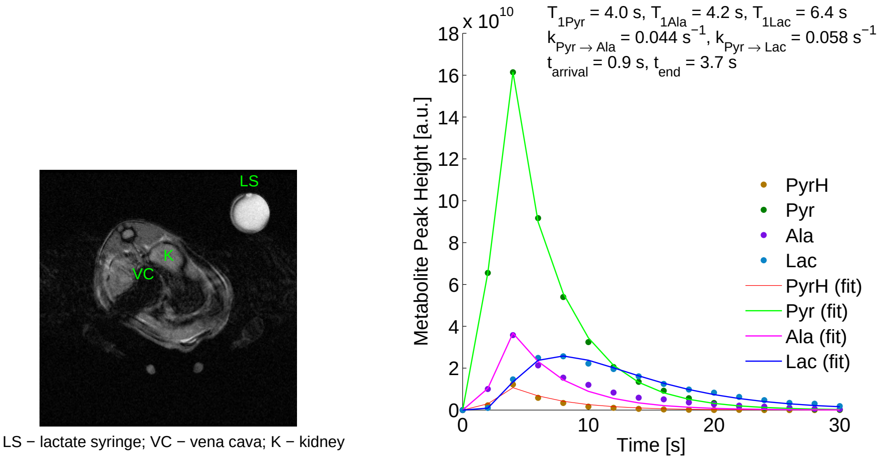

(a) (b)

Figure 4.43.: (a) T2-weighted MR image of a 10 mm slice centered on rat kidney. (b) Time curves of metabolite levels. Measured data are represented by coloured filled circles, the estimated fit lines are represented by solid lines

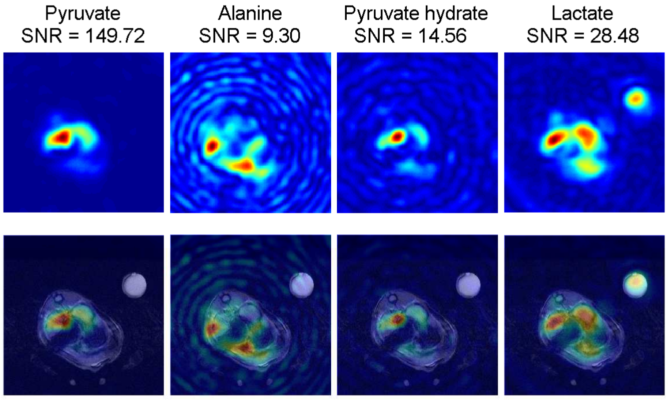

(a) Conventional LSCSI

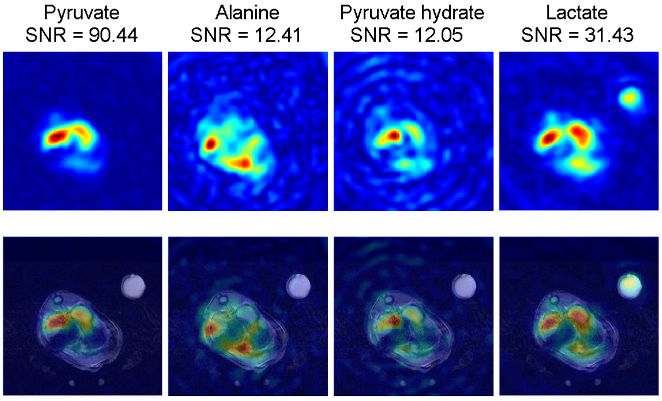

(b) First-order correction

Figure 4.44.: Case study 1. Images of 4 metabolites with specified SNR (sum over 16 time frames) reconstructed using conventional LSCSI method for metabolite separation (a) and the corrected version (b)

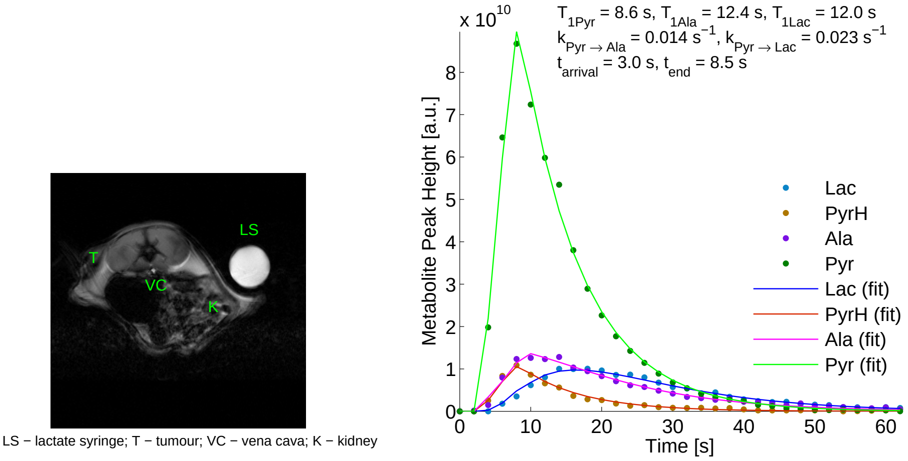

(a) (b)

Figure 4.45.: (a) T2-weighted MR image of a 3 mm slice centered on rat tumour. (b) Time curves of metabolite levels. Measured data are represented by coloured filled circles, the estimated fit lines are represented by solid lines

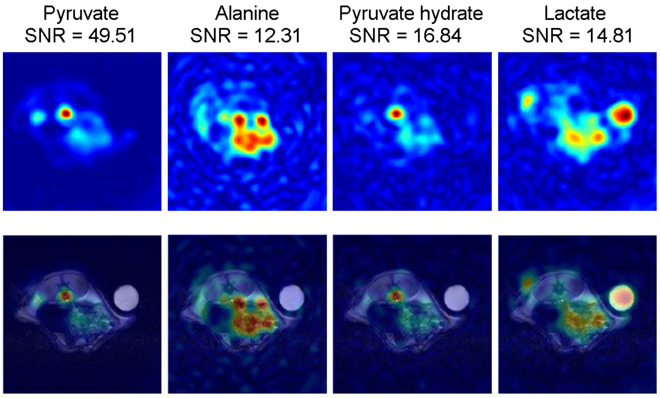

(a) Conventional LSCSI

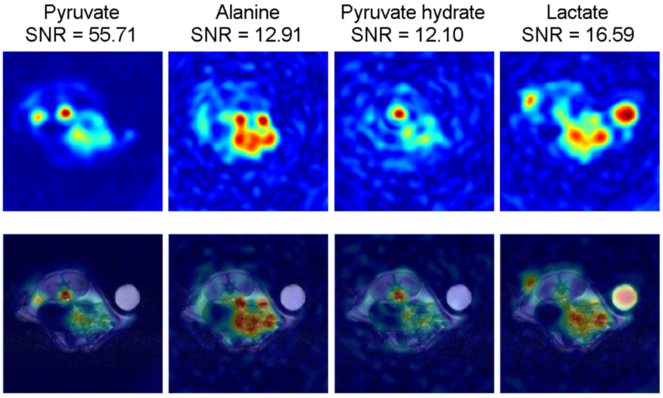

(b) First-order correction

Figure 4.46.: Case study 2. Images of 4 metabolites with specified SNR (sum over 32 time frames) reconstructed using conventional LSCSI method for metabolite separation (a) and the corrected version (b)

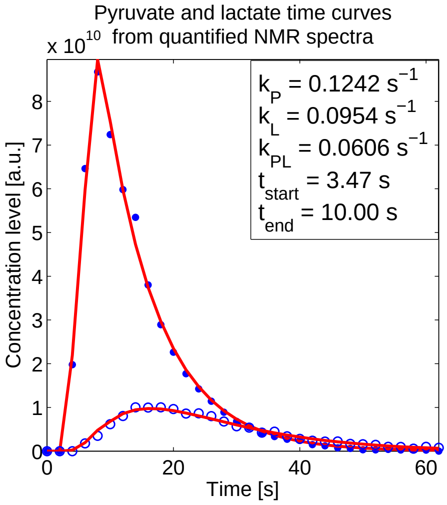

Figure 4.47.: Dynamic curves of metabolite levels in a slice centered on rat kidney estimated from NMR spectra. Pyruvate data are represented by filled circles, lactate data are represented by empty circles. Estimated best fit lines are represented by red lines. Metabolic parameters, estimated from the model, are listed inside the plot

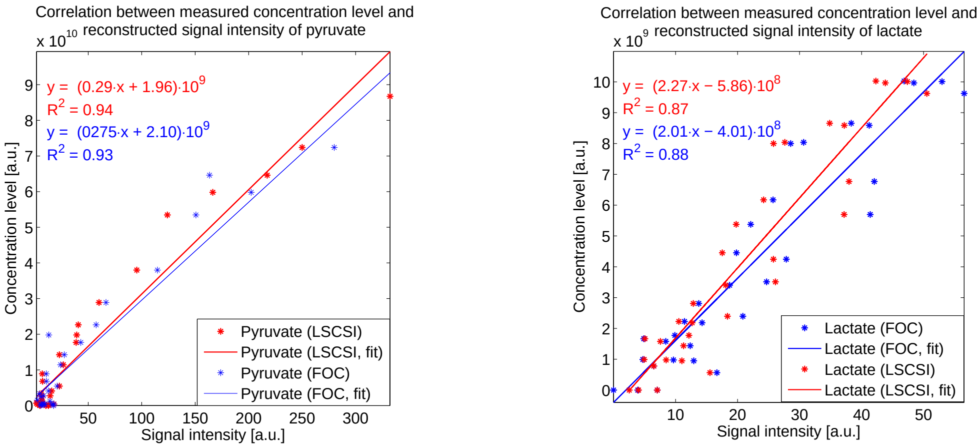

(a) Pyruvate

(b) Lactate

Figure 4.48.: Correlation between measured metabolite levels and reconstructed pixel intensity for pyruvate (a) and lactate (b). Data reconstructed with conventional method of LSCSI and after the first-order correction (FOC) are shown with red and blue asterisks, respectively. Estimated best fit lines are represented by the red and blue solid line,s respectively. The fit equations and the goodness of linear regression R^2 are given inside the plots

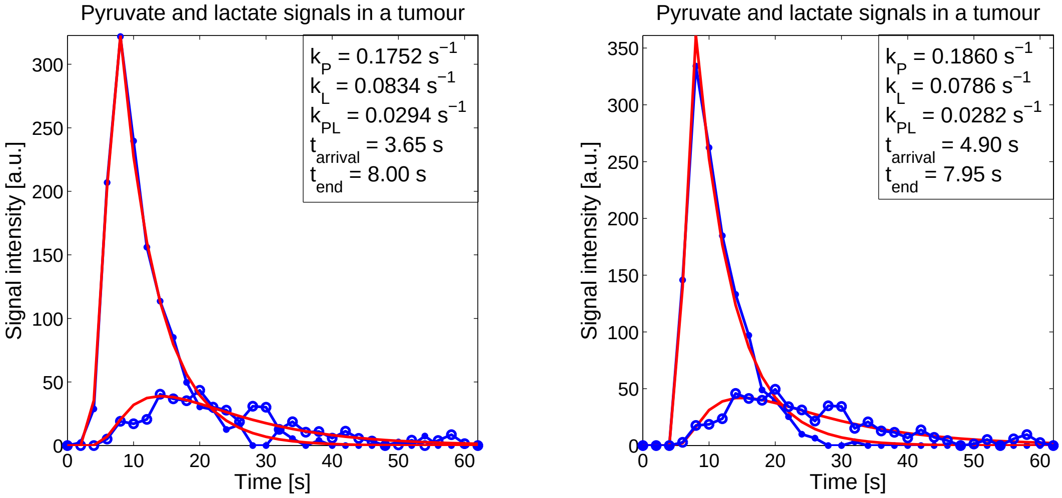
Pyruvate and lactate signals in a tumour

Pyruvate and lactate signals in a tumour

(a) Conventional LSCSI

(b) Model-based correction

Figure 4.49.: Dynamic curves of metabolite signal intensity in a tumour estimated from images of pyruvate and lactate when conventional LSCSI (a) and first-order correction (b) were used. Pyruvate data are represented by filled circles, lactate data are represented by empty circles. Estimated best fit lines are represented by red lines

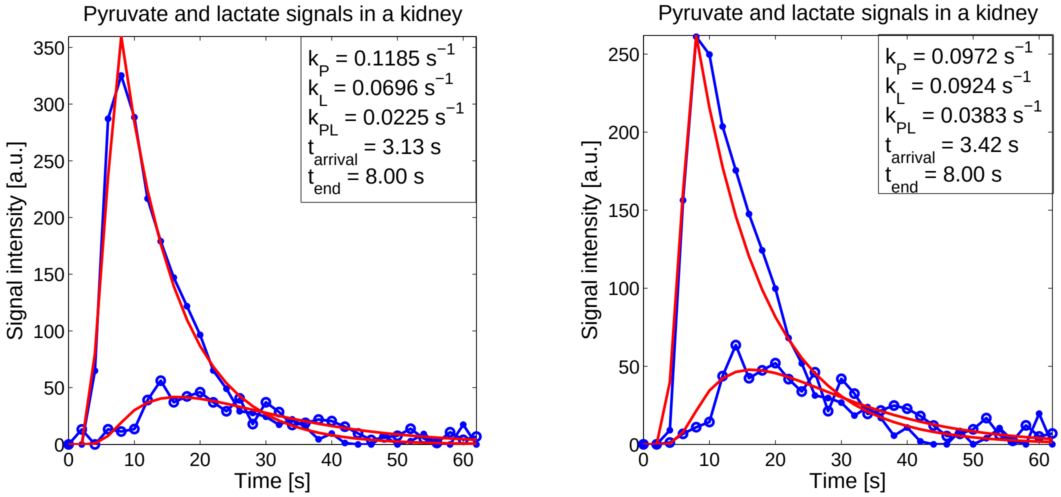
Pyruvate and lactate signals in a kidney

Pyruvate and lactate signals in a kidney

(a) Conventional LSCSI

(b) Model-based correction

Figure 4.50.: Dynamic curves of metabolite signal intensity in a kidney estimated from images of pyruvate and lactate when conventional LSCSI (a) and first-order correction (b) were used. Pyruvate data are represented by filled circles, lactate data are represented by empty circles. Estimated best fit lines are represented by red lines

In order to check whether the quantification ability of the new method is comparable with conventional reconstruction and which discrepancies arise, the kinetic rates such as pyruvate-to-lactate conversion k_{PL} as well as rate constants of pyruvate and lactate signal decay k_P and k_L were estimated. For this, pixel intensity curves corresponding to the signal change in the middle of tumour and in kidney were fitted using the two-site exchange model. Results are presented in Figures 4.49, 4.50 with corresponding estimated parameters listed inside the plots. Images from the case study 2 (Fig. 4.46) served the source for comparison of the estimated kinetic rates.

One important aspect of metabolic quantification by imaging is maintenance of linear relation between metabolite peak heights measured by NMR spectroscopy (proportional to the metabolite concentration levels) and the signal intensity of the same metabolite obtained from the image. With the current technique we are able to measure the spectrum of the composite lactate within the entire slice only.

When the distribution of metabolite of interest is relatively homogeneous and kinetic behaviour did not radically change, like it was shown in the experiment with a phantom in Section 4.2.2, we could sum the signal intensities within the slice and these two variables (metabolite concentration and image signal intensity) demonstrated perfect linear relationship (Fig. 4.19).

For the *in vivo* data as shown in Fig. 4.48 there are deviations from linear regression since the intensities of pyruvate and lactate signal were measured locally in the region of tumour. Still we can say that both methods, conventional LSCSI and the FOC, lead to very close results.

Pixel intensity curves obtained from images reconstructed with the conventional method and the one we proposed are given in Figures 4.49, 4.50 for two respective cases of measuring the signal in the center of a tumour and kidney in animal model.

The obtained time curves were fitted using the two-site exchange model and we used the estimated kinetic rates for quantitative comparison between conventional and the proposed methods. Since there is no reference or ground truth available to be able to say which method conveys the metabolic behaviour more accurately, we could only reflect on the arisen differences between these two methods. In a tumour we obtained a higher pyruvate signal using the FOC of chemical shift separation matrix and steeper but also later signal uptake (4.9 sec versus 3.6 sec), and lower noise level at the later acquisitions (Fig. 4.49 (b)) compared to conventional reconstruction (Fig. 4.49 (a)). Other differences include slightly shorter pyruvate and longer lactate T_1 times and a rather close resulting value of pyruvate-to-lacte conversion (0.0282 s^{-1} versus 0.0294 s^{-1}) in case of the corrected reconstruction.

Pyruvate and lactate signals in kidney had larger discrepancies for two methods (Fig. 4.50). After the FOC the pyruvate signal slightly dropped and, in opposite, lactate signal increased. The resulting conversion rate differs to a larger extent from the one estimated for the conventional case (0.0383 s^{-1} versus 0.0225 s^{-1}).

4.3.3. Discussion

Iterative decomposition of water and fat with echo asymmetry and least-squares estimation (IDEAL) method has proven to be fast and efficient for separation of ^{13}C species. However, the underlying least squares chemical shift imaging (LSCSI) technique, which requires multiple acquisitions to resolve metabolites, is not consistent with the fast changing metabolic signal. Total signal contributions from metabolites are assumed to be constant within several acquisitions, which contradicts with the highly dynamic metabolic behaviour. In this work a valid extension to the physical model of signal acquisition in ^{13}C chemical shift imaging (CSI) was proposed. It uses correcting factors obtained by kinetic modelling of metabolic time curves, combines computational simplicity of the direct inversion with higher accuracy of model-based approaches and eliminates the need for additional regularisation.

Results obtained in numerical simulations demonstrated improvement of image quality and preservation of metabolic quantification properties of images reconstructed using the corrected version of the spectral encoding matrix for chemical shift separation. Major sign of improvement was the decrease or complete elimination of the so-called "bleeding" artifact appearing in lactate images at places of pyruvate distribution.

Results for *in vivo* data are rather contradictory since they differ significantly from one data set to another. The achieved increase in SNR is not reproducible therefore it is hard to draw the conclusion regarding the yielded improvement with the proposed technique. However, what we observed was the decrease of artifacts in alanine and lactate images and the overall slightly elevated signal level.

5. Outlook and Future Work

5.1. Voxel-Wise Nonlinear Model Regression

Kinetic modelling in this work has been performed using NMR spectra of carbon reconstructed from the slice-selective FID signal. Obtained time curves represent evolution of the composite metabolite signal from the entire slice. It would be highly advantageous to include the kinetic equations into the existing signal model and perform iterative reconstruction with joint estimation of kinetic rate constants for all individual pixels (voxels in 3D imaging). In other words, we would search for a solution such that each pixel of the resulting series of images behaves in accordance with the kinetic exchange model [102] and is consistent with the acquired data. This task leads to a system of nonlinear equations which should be solved for the unknown kinetic parameters and phase components

$$\begin{gathered}\widehat{\mathbf{x}} = \text{arg} \min_{k_P^i, k_L^i, k_{PL}^i, r_{inj}, t_{arr}^i, t_{end}^i, \phi_i} \left\| \mathbf{A}(M_z^i, \phi_i) - \mathbf{s} \right\|_2^2 \text{ such that} \\ x_i = M_z^i e^{i2\pi\phi_i}, M_z \in \mathbb{R}^2, \phi \in \mathbb{R}^2 \text{ subject to} \\ k_P^i \leq 0.1,\ k_L^i \leq 0.1,\ k_{PL}^i \leq 0.1,\ 0 \leq \phi \leq 2\pi \end{gathered} \tag{5.1}$$

where

$$M_z = \begin{cases} \frac{r_{inj}}{k_P}(1 - e^{-k_P(t-t_{arr})}), & t_{arr} \leq t < t_{end} \\ M_z(t_{end})e^{-k_P(t-t_{end})}, & t \geq t_{end} \end{cases} \text{for substrate} \tag{5.2}$$

$$M_z = \begin{cases} \frac{k_{PL}r_{inj}}{k_P-k_L}(\frac{1-e^{-k_L(t-t_{arr})}}{k_L} - \frac{1-e^{-k_P(t-t_{arr})}}{k_P}), & t_{arr} \leq t < t_{end} \\ \frac{P_z(t_{end})k_{PL}}{k_P-k_L}(e^{-k_L(t-t_{end})} - e^{-k_P(t-t_{end})}), & t > t_{end} \\ \quad +M_z(t_{end})e^{-k_L(t-t_{end})}, & \end{cases} \text{for downstream metabolite} \tag{5.3}$$

Here the signal model matrix **A** includes kinetic equations 5.2, 5.3 and depends nonlinearly on the unknown kinetic rates: k_P, k_L (effective decay rates of pyruvate and lactate [s^{-1}]), k_{PL} (forward ($Pyr \to Lac$) conversion rate [s^{-1}]), r_{inj} (injection rate [mL/s]), t_{arr}, t_{end} (times of arrival of agent and the end of injection, respectively [s]). Subscript $i = 1...N$ denotes pixel index and N is the total number of pixels. Since the desired unknown image is complex valued we separated the magnitude and pase components. Our goal then is to reconstruct both the magnitude map $M_z \in \mathbb{R}^2$ and the phase map $\phi \in \mathbb{R}^2$ from the measured data **s** subject to the specified inequality constraints.

The feasibility of this concept has been proven in numerical simulations. We used a very similar design of computer experiment that was used for validation of reconstruction techniques with regularisation (see 3.4.1). However, higher variability of kineic rates was simulated. True maps of kinetic rates are given in Fig. 5.1 (a). Inserting these values into exponential kinetic equations (Eq. 5.2, 5.3) we can compute the metabolite concentration

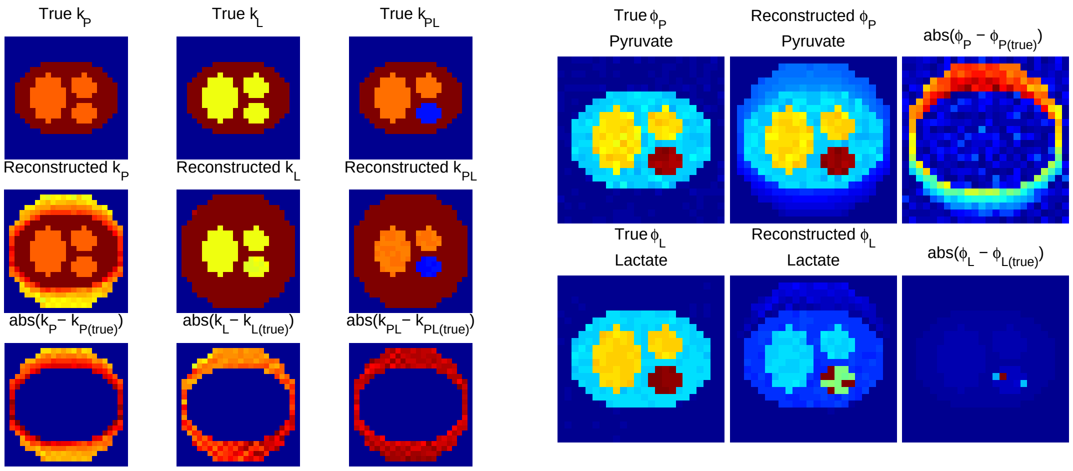

(a)

(b)

Figure 5.1.: (a) From upper to lower row: 24×24 matrices of kinetic rates for 2D slice; reconstructed maps of kinetic rates; difference image. (b) True and reconstructed phase maps and computed difference images for pyruvate (1st row) and lactate (2nd row)

levels at each time step for each pixel location, which gives the resulting true images.

Reconstruction was performed using conventional method of the direct matrix inversion and by means of iterative solution of the arisen nonlinear least squares problem (5.1) for all unknown kinetic rates using `lsqnonlin` solver. The method required user-defined Jacobian for the faster convergence. Estimated rates were then used to calculate all metabolic maps.

Figures 5.2, 5.3 show images of pyruvate and lactate, respectively, reconstructed with conventional method of direct inversion of signal model matrix and by means of pixel-wise fitting of kinetic equations in iterative reconstruction scheme. Difference images and calculated root-mean-square error (RMSE) show at least 100-fold decrease of error with iterative reconstruction when individual signal curves were fitted using kinetic model.

There are several critical aspects that have caused complexities when applying the method to the *in vivo* data:

1. Very long computational time
   Reconstruction time for 5 time frames, 2 metabolites, 24×24 image size and 40 iterations was 39 minutes in simulations. In experiments with *in vivo* we typically acquire from 16 to 30-35 time frames for 5 metabolites and 64×64 image size, which leads to very high time expenses, inability to evaluate the performance of reconstruction technique and perform debugging.
2. Necessity to obtain good initial estimate
   Nonlinear regression is iterative procedure. Before the procedure can begin we need to define initial values for each parameter.
3. Decision-making upon which model parameters to fit and which to constrain

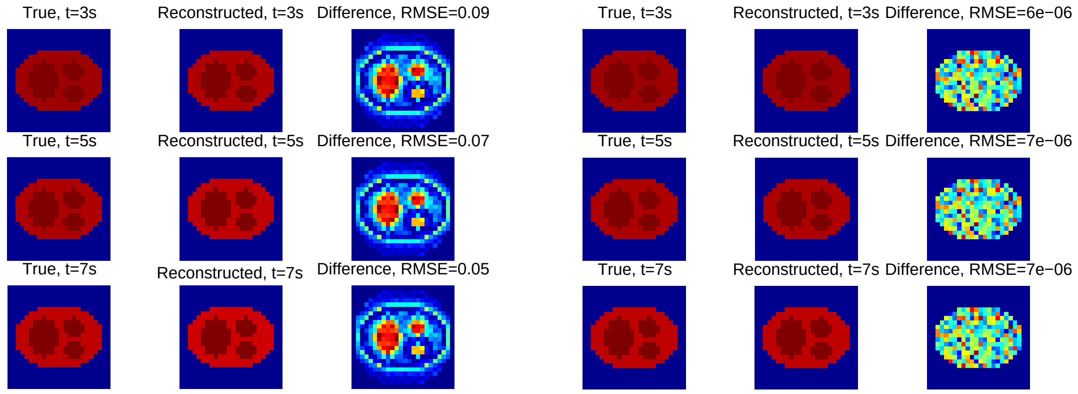

(a) Conventional reconstruction using pseudoinverse of signal matrix

(b) Iterative reconstruction using pixel-wise kinetic modelling

Figure 5.2.: True and reconstructed images of pyruvate for three time steps

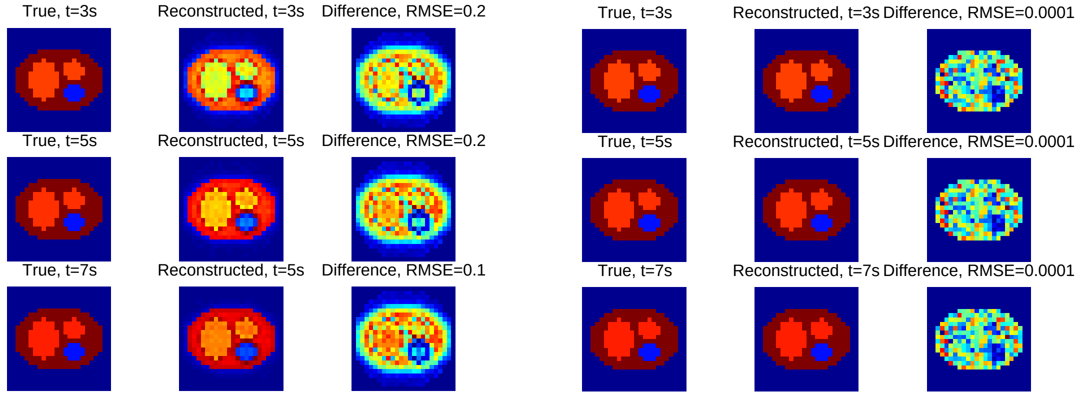

(a) Conventional reconstruction using pseudoinverse of signal matrix

(b) Iterative reconstruction using pixel-wise kinetic modelling

Figure 5.3.: True and reconstructed images of lactate for three time steps

4. Outliers removal
   Some of the pixels may have signal which does not satisfy the defined model. If deviations from the modelled behaviour are too big, the outlier must be deleted from analysis but for that the difference must be quantified.

Depending on complexity of the biological model, fitting it to the measured data may become a difficult task when many different factors have a large impact on the results.

Results achieved in numerical simulations show great potential of the iterative reconstruction using nonlinear regression for fitting the family of kinetic curves to the measured data, and it is a task which is worth investigating in future.

5.2. Quantification Challenges

There are several issues concerning reliability and interpretation of metabolite maps for clinical diagnosis.
First relates to the method of analysis of the acquired data. It can be static and dynamic, qualitative (visual assessment of images) and quantitative (measurement of signal magnitude of expressed metabolite and physiological parameters).

^{13}C chemical shift imaging with IDEAL (iterative decomposition of water and fat with echo asymmetry and least-squares estimation) serves the purpose to visualise, localise metabolic activity and to obtain quantitative estimate of underlying kinetic parameters. Therefore it is important to ensure that reconstruction yields meaningful reproducible results. When a new reconstruction method is proposed, phantom experiments are indispensable as well as comparative studies with other reconstruction techniques.

One should choose an appropriate method for quantification of ^{13}C spectra such as measurement of peak height, integration, spectral fitting etc. But even if areas under resonance peaks in ^{13}C spectra are, in principle, directly proportional to concentrations of respective metabolites, for *in vivo* studies this is often not the case. Detection of resonance peaks can be affected by imperfections in RF pulse angles, coupling effects [16] and other sources of bias which when uncorrected lead to errors in quantification.

Absolute quantification of spectra is not enough to make conclusions regarding the presence of abnormality in tissue state. It is important to trace the evolution of metabolic time courses relative to each other due to very high variability among absolute signal intensities. Lactate-to-pyruvate ratio (LPR) serve as a marker of glycolytic lactate production [60] and a reliable metric for quantification of metabolic conversion.

There are also two challenging aspects when performing the visual image assessment and localisation of suspicious metabolic activity. One is availability of correct up-to-date anatomical reference and exact coregistration of anatomical and functional information. For *in vivo* settings voluntarily and involuntarily patient motion can become a major problem - even a slight shift in organ position can disrupt readability of the data.

Secondly, large spectral dispersion of resonance frequencies sometimes leads to severe chemical shift displacement artifacts [46], known in literature also as chemical shift displacement error (CSDE). It is a well-studied but often underestimated effect in localised spectroscopy [95] which arises from the fact that signals with different chemical shifts experience different frequency-encoded slice selections and do not originate from exactly the same volume. It leads to inaccurate signal localisation, no more conforming to an anatomical scan and voxel contamination.

For further quantitative analysis it would be beneficial to compare ^{13}C MRSI with other functional imaging modalities and, indeed, such studies were conducted. Menzel et al. [60] presented the results of comparative study with ^{13}C MRSI and ^{18}F-FDG PET, a well-established method for measuring glucose uptake by tumour cells. However, no significant correlation between PET and MRSI data was observed.

Last but not least, concentrations of metabolites of interest are much less than concentration of the water molecules (approximately 10 mM versus 55 M [31]), the fact which results in times lower signal magnitude compared to the signal coming from the water and the lipids.

5.3. Conclusion

Magnetic resonance spectroscopic imaging with hyperpolarised ^{13}C agents is a novel technique that reveals a wealth of metabolic information, which can be spatially mapped over the entire slice and time-resolved to depict metabolic conversion. Clinical importance of the method lies in the provided cues to differentiate between tumour and healthy tissues due to large change of the metabolic profile.

Being acquired under challenging conditions of rapidly decaying signal and limited doses of injected hyperpolarised agent, reconstructed images exhibit low signal-to-noise ratio (SNR) and artifacts. The goal of this work was 1) to enhance the quality of images by means of iterative reconstruction with regularisation terms and 2) to propose a valid extension to the physical model of signal acquisition in ^{13}C chemical shift imaging (CSI).

The first goal was addressed by reformulating the inverse problem as a regularised least-squares, where the solution was chosen to be one that minimises a user-defined objective function consisting of a fidelity term and a regularisation term aiming at penalising noise and non-smooth changes. For the latter, mathematical simulations were performed to investigate the effect of Tikhonov, total variation (TV) and total generalised variation (TGV) penalty [49] terms on the outcome of reconstruction when the ground truth was provided. TGV demonstrated clear advantage over both TV and Tikhonov regularisation terms. It has equally good edge-preserving and denoising properties. Longer computational times of TGV reconstruction did not become the obstacle for research purposes, but can be critical for the clinical workflow. TGV constraint was applied to the real *in vivo* data together with the support mask derived either by means of active contour-based segmentation or thresholding to discard the out-of-object signal and to improve visualisation of coregistered anatomical and functional images.

In the second approach of the model-based correction, we used time-dependent factors obtained by kinetic modelling of metabolic time curves in order to compensate for errors which arise due to inaccuracy of least-squares chemical shift imaging (LSCSI) technique [72] for separation of the metabolites at the initial stage of reconstruction.

To validate both techniques, the simulation framework for ^{13}C metabolic imaging with quantitative evaluation of reconstruction performance with root-mean-square error (RMSE) was presented. In case with experimentally acquired *in vivo* animal data, signal-to-noise ratio (SNR) metric was used to characterise and compare reconstruction techniques.

In simulated- and real-data experiments quantification ability of reconstructed time series of metabolic images was not disrupted. It was verified by calculating kinetic rates of pyruvate-to-lactate conversion and comparing them between methods.

SNR improvement of up to 40 % as well as better delineation of structure borders and good denoising performance were achieved with TGV penalty function and anatomical constraint. Summarising the effect of the model-based correction on the outcome of reconstruction, noise reduction was observed in images of alanine and lactate distribution and pyruvate and pyruvate hydrate spatial maps showed elevated signal in organs. Such first-order correction required very low computational resources and only a single additional step of spectra quantification. The major drawback is the current ability to account only for the average signal evolution from the whole slice, which still results in errors in case of heterogeneous kinetic rates within the slice.

There are two potential directions of future work. One will be aimed at modification of the pulse sequences so that the repetition time and flip angle would depend on the metabolic dynamics. In the second approach, signal evolution of the individual voxels can be included in the forward signal model. So far this method has been validated only in simulations but showed a large increase in accuracy of reconstruction and therefore is worth further investigation.

Appendix

A. Appendix

Algorithm 1: Conjugate gradient solving $\mathbf{A}\mathbf{x} = \mathbf{s}$ with $\mathbf{A}$ symmetric and positive-definite.

```
input: $\mathbf{A}$, $\mathbf{s}$, and $\mathbf{x}_0$ (default: $\mathbf{x}_0 = 0$);
Initialization: $\mathbf{r}_0 = \mathbf{s} - \mathbf{A}\mathbf{x}_0$, $\mathbf{p}_0 = \mathbf{r}_0$, and $i = 0$;
repeat
    $\mathbf{q}_i \leftarrow \mathbf{A}\mathbf{p}_i$;
    $\alpha_i \leftarrow \mathbf{r}_i^{\mathrm{H}}\mathbf{r}_i/(\mathbf{p}_i^{\mathrm{H}}\mathbf{q}_i))$;
    $\mathbf{x}_{i+1} \leftarrow \mathbf{x}_i + \alpha_i\mathbf{p}_i$;
    $\mathbf{r}_{i+1} \leftarrow \mathbf{r}_i - \alpha_i\mathbf{q}_i$;
    $\mathbf{p}_{i+1} \leftarrow \mathbf{r}_{i+1} + \mathbf{r}_{i+1}^{\mathrm{H}}\mathbf{r}_{i+1}/(\mathbf{r}_i^{\mathrm{H}}\mathbf{r}_i)\mathbf{p}_i$;
    $i \leftarrow i + 1$;
until desired tolerance is reached;
return $\mathbf{x}_i$
```

Algorithm 2: Primal-Dual method for TGV undersampling reconstruction.
$\mathrm{proj}_{P^h}(p^h), \mathrm{proj}_{Q^h}(q^h)$ are the Euclidian projectors onto the convex sets P^h, Q^h;
$prox_2^{\sigma}(r^h)$ is the proximal map;
σ, τ are the step-sizes.

```
input: $\mathbf{s}^h, \mathbf{A}^h$ ;
Initialization: $\mathbf{x}^h, \overline{\mathbf{x}}^h \leftarrow 0, \nu^h, \overline{\nu}^h \leftarrow 0, p^h \leftarrow 0, q^h \leftarrow 0, r^h \leftarrow 0, \tau, \sigma > 0$;
repeat
    $p^h \leftarrow proj_{P^h}(p^h + \sigma(\nabla^h\overline{\mathbf{x}}^h - \overline{\nu}^h))$;
    $q^h \leftarrow proj_{Q^h}(q^h + \sigma\varepsilon^h\overline{\nu}^h)$;
    $r^h \leftarrow prox_2^{\sigma}(r^h + \sigma(\mathbf{A}^h\overline{\mathbf{x}}^h - \mathbf{s}^h))$;
    $\mathbf{x}_{old}^h \leftarrow \mathbf{x}^h$;
    $\mathbf{x}^h \leftarrow \mathbf{x}^h + \tau(\mathrm{div}_1^h p^h - (\mathbf{A}^h)^* r^h)$;
    $\overline{\mathbf{x}}^h \leftarrow 2\mathbf{x}^h - \mathbf{x}_{old}^h$;
    $\nu_{old}^h \leftarrow \nu^h$;
    $\nu^h \leftarrow \nu^h + \tau(p^h + \mathrm{div}_2^h q^h)$
    $\overline{\nu}^h \leftarrow 2\nu^h - \nu_{old}^h$
until convergence of $\mathbf{x}^h$;
return $\mathbf{x}^h$
```

Algorithm 3: Calculation of molarity, volumes of chemical reagents for experiment on a phantom.

```
given:
$M_{PyrInit}$ = 80 mmol;
$M_{PyrFin}$ = 5 mmol;
$M_{NADHFin}$ = 5 mmol;
$V_{Fin}$ = 1 mL;
$V_{LDHFin}$ = 0.2 mL;
$MW_{NADH}$ = 709.4 g/mol
$M_{LDH}$ = 500 units/mL;
$M_{LDHFin}$ = 100 units/mL
find: $M_{Pyr}$, $V_{Pyr}$, $M_{NADH}$, $V_{NADH}$, $m_{NADH}$, $V_{LDH}$
$M_{PyrFin} \cdot V_{Fin} = x \cdot (V_{Fin} - V_{Enzyme})$
$M_{Pyr}$ = 6.25 mmol
$M_{Pyr} \cdot V_{Pyr} = M_{PyrInit} \cdot 1mL$
$V_{Pyr}$ = 0.0781 mL
$V_{NADH} = (V_{Fin} - V_{Enzyme}) - V_{Pyr}$ = 0.7219 mL
$M_{NADHFin} \cdot V_{Fin} = M_{NADH} \cdot V_{NADH}$
$M_{NADH}$ = 6.9264 mmol
$m_{NADH} \cdot V_{Fin} = MW_{NADH} \cdot M_{NADH}$
$m_{NADH}$ = 4.9130 mg
$M_{LDH} \cdot V_{LDH} = M_{LDHFin} \cdot V_{Fin}$
$V_{LDH}$ = 0.2 mL
```

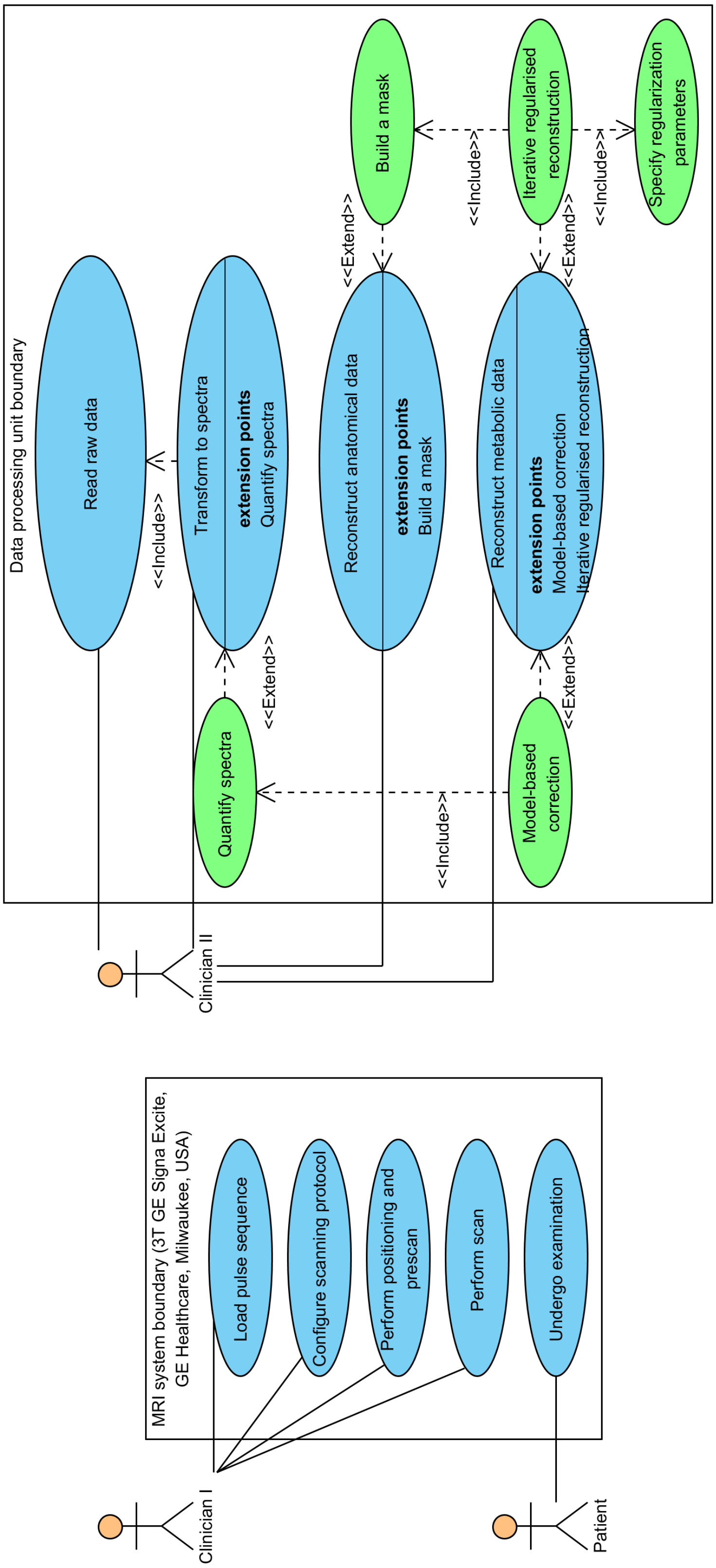

Figure A.1.: Use case diagram

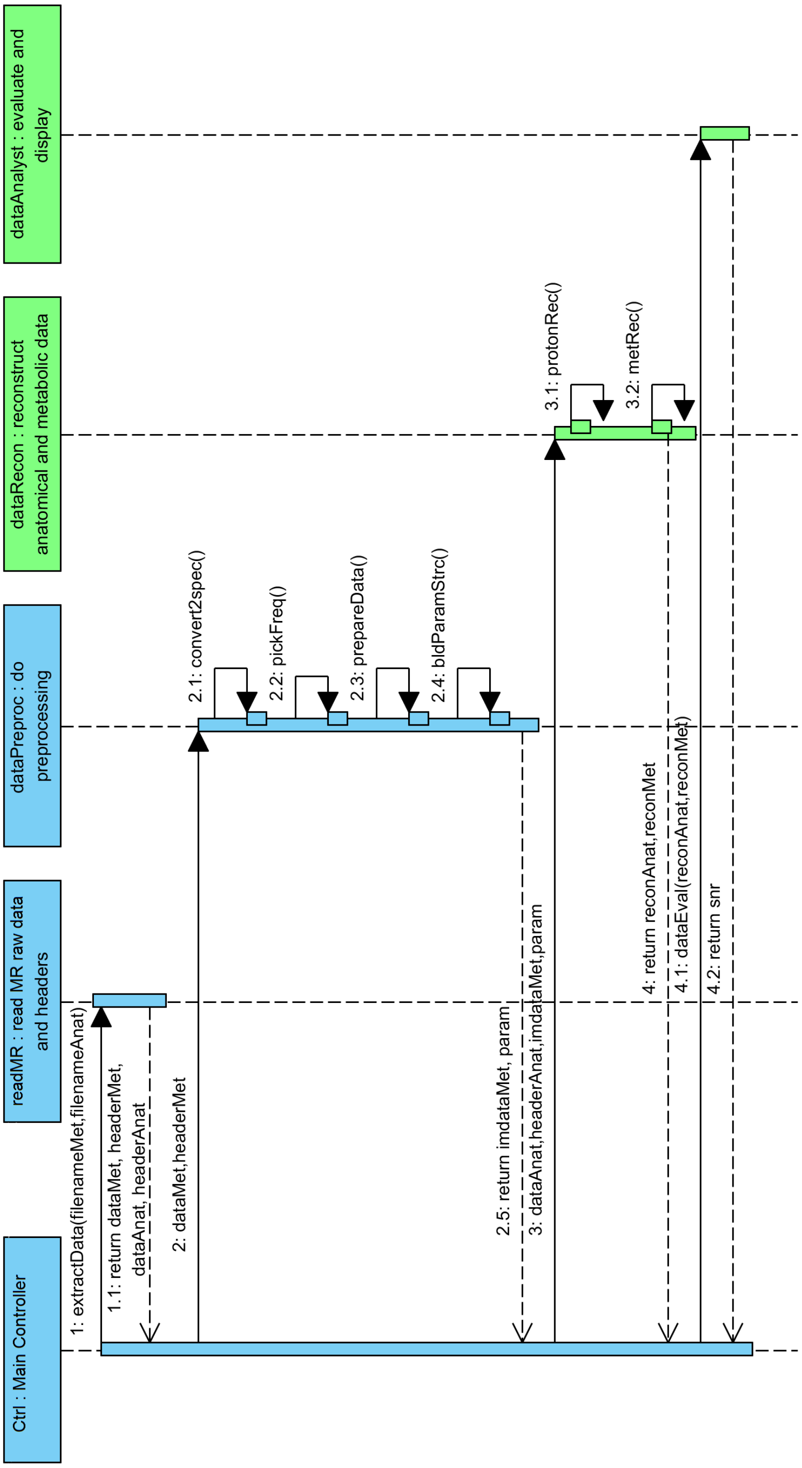

Figure A.2.: Sequence diagram

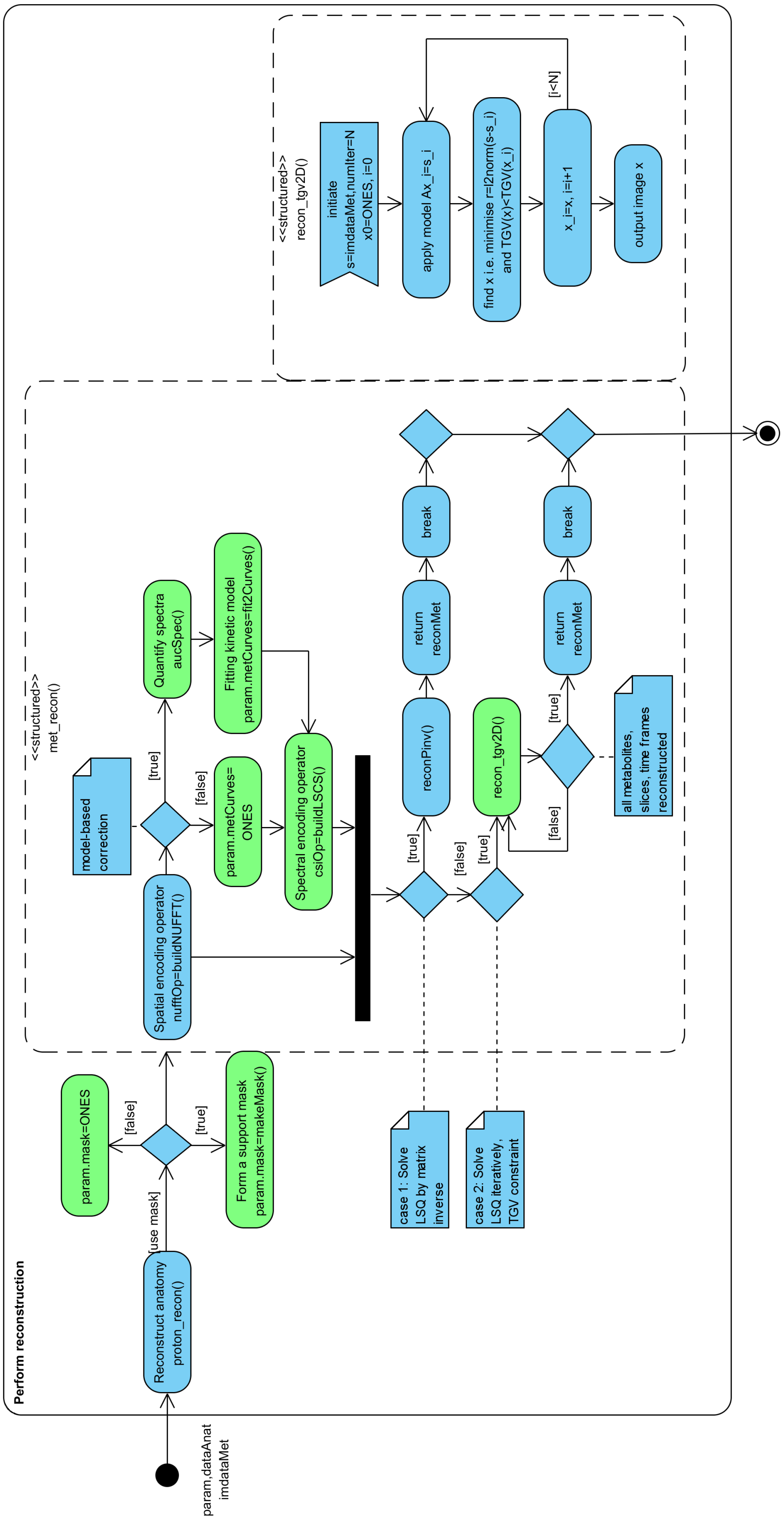

Figure A.3.: Activity diagram

Bibliography

[1] G. Adluru, C. Mcgann, P. Speier, E.G. Kholmovski, A. Shaaban, and E. Dibella. Acquisition and reconstruction of undersampled radial data for myocardial perfusion magnetic resonance imaging. *Journal of Magnetic Resonance Imaging*, pages 466–473, 2009.

[2] J.H. Ardenkjaer-Larsen, B. Fridlund, Gram A., G. Hansson, L. Hansson, M.H. Lerche, R. Servin, M. Thaning, and K. Golman. Increase in signal-to-noise ratio of gt; 10,000 times in liquid-state nmr. *National Academy of Sciences. Proceedings*, 100(18):10158–10163, 2003.

[3] B. Bai, Q. Li, and R. M. Leahy. Magnetic resonance-guided positron emission tomography image reconstruction. *Semin Nucl Med*, 43(1):30–44, Jan 2013.

[4] J. Besag. Spatial Interaction and the Statistical Analysis of Lattice Systems. *Journal of the Royal Statistical Society. Series B (Methodological)*, 36(2), 1974.

[5] R. Bitar, G. Leung, R. Perng, S. Tadros, A.R. Moody, J. Sarrazin, C. McGregor, M. Christakis, S. Symons, A. Nelson, and T.P. Roberts. Mr pulse sequences: what every radiologist wants to know but is afraid to ask. *Radiographics*, 26(2):513–37.

[6] K.T. Block, M. Uecker, and J. Frahm. Undersampled radial MRI with multiple coils. Iterative image reconstruction using a total variation constraint. *Magnetic Resonance in Medicine*, 57(6):1086–1098, 2007.

[7] K.T. Block, M. Uecker, and J. Frahm. Model-based iterative reconstruction for radial fast spin-echo mri. *IEEE Trans. Med. Imaging*, 28(11):1759–1769, 2009.

[8] L. Brateman. Chemical shift imaging: a review. *AJR Am J Roentgenol*, 146(5):971–80, 1986.

[9] K. Bredies, K. Kunisch, and T. Pock. Total generalized variation. *SIAM J. Imaging Sciences*, 3(3):492–526, 2010.

[10] P. Callaghan. Principles of nmr and mri. `http://www.magritek.com/support-videos`, 2012.

[11] E. J. Candes and M. B. Wakin. An Introduction To Compressive Sampling. *IEEE Signal Processing Magazine*, 25(2):21–30, March 2008.

[12] I. Carron. Compressive sensing: The big picture. `https://sites.google.com/site/igorcarron/Home`, June 2010. Accessed: 2010.

[13] Y. Censor. Finite Series-Expansion Reconstruction Methods. In *Proc. of the IEEE*, pages 409–419, March 1983.

[14] A. Chambolle and T. Pock. A first-order primal-dual algorithm for convex problems with applications to imaging. *J. Math. Imaging Vis.*, 40(1):120–145, May 2011.

[15] T.F. Chan, B. Yezrielev Sandberg, and L.A. Vese. Active contours without edges for vector-valued images. *Journal of Visual Communication and Image Representation*, 11:130–141, 2000.

[16] I.Y. Choi and R. Gruetter. *Neural Metabolism In Vivo*. Advances in Neurobiology. Springer, 2012.

[17] W.R. Crum, T. Hartkens, and D.L. Hill. Non-rigid image registration: theory and practice. *Br J Radiol*, 77 Spec No 2:S140–153, 2004.

[18] S.E. Day, M.I. Kettunen, F.A. Gallagher, D.E. Hu, M. Lerche, J. Wolber, K. Golman, J.H. Ardenkjaer-Larsen, and K.M. Brindle. Detecting tumor response to treatment using hyperpolarized 13c magnetic resonance imaging and spectroscopy. *Nat Med.*, 13(11):1382–1387, 2007.

[19] W. de Boer, M. Borghini, K. Morimoto, T. Niinikoski, and F. Udo. Dynamic polarization of protons, deuterons, and carbon-13 nuclei: thermal contact between nuclear spins and an electron spin-spin interaction reservoir. *J. Low Temp. Phys.*, 15(3-4):249–67, 1974.

[20] M.S. Dodd, V. Ball, R. Bray, H. Ashrafian, H. Watkins, K. Clarke, and D.J. Tyler. In vivo mouse cardiac hyperpolarized magnetic resonance spectroscopy. *Journal of Cardiovascular Magnetic Resonance*, 15(1):19, 2013.

[21] M. Durst. Fast spectroscopic magnetic resonance imaging of hyperpolarised 13c with spiral acquisition schemes. Diploma thesis, Technische Universität München, 2011.

[22] M. Durst, R.F. Schulte, F. Schilling, E. Weidl, O. Khegai, M.A. Janich, J.I. Sperl, U. Koellisch, F. Wiesinger, M. Schwaiger, and Haase A. Parallel spiral chemical shift imaging for metabolic imaging with hyperpolarised 13c. In *Proceedings of ISMRM 2011*, 2011.

[23] T. Eykyn, R. Southworth, and S. Kozerke. Dynamic nuclear polarization and mri for the study of cardiac metabolism. *Heart and Metabolism*, 55(55):13–17, 2012.

[24] J. Fessler. Model-Based Image Reconstruction for MRI. *IEEE Signal Processing Magazine*, 27(4):81–89, July 2010.

[25] J. Fessler. Model-Based Image Reconstruction for MRI. *IEEE Signal Processing Magazine*, 27(4):81–89, July 2010.

[26] J.A. Fessler. On NUFFT-based gridding for non-Cartesian MRI. *J. Magn. Reson.*, 188(2):191–195, Oct 2007.

[27] J.A. Fessler and B.P. Sutton. Nonuniform fast Fourier transforms using min-max interpolation. *Signal Processing, IEEE Transactions on*, 51(2):560–574, February 2003.

[28] E. Fieremans. Validation methods for diffusion weighted magnetic resonance imaging in brain white matter. page 182, 2008.

[29] R.D. Fierro, G.H Golub, P.C. Hansen, and Dianne P. O'Leary. Regularization by truncated total least squares. *SIAM Journal on Scientific Computing*, 18:1223 – 1241, 1997.

[30] B. Flemisch. Comparison of iterative solvers. `http://m2matlabdb.ma.tum.de/download.jsp?MC_ID=3&SC_ID=5&MP_ID=72`. Accessed: 2008-08-08.

[31] A.B. Gagoski. Spiral chemical shift imaging at 3T using 32 channel receive array and online reconstruction. *Prilozi*, 31(2):135–149, Dec 2010.

[32] F.A. Gallagher, M.I. Kettunen, S.E. Day, D. Hu, J.H. Ardenkjar-Larsen, R. Zandt, P.R. Jensen, M. Karlsson, K. Golman, M.H. Lerche, and K.M. Brindle. Magnetic resonance imaging of ph in vivo using hyperpolarized 13c-labelled bicarbonate. *Nature*, 453(7197):940–943, 2008.

[33] F.A. Gallagher, M.I. Kettunen, D.E. Hu, P.R. Jensen, R.K. Zandt, A. Gisselsson, S.K. Nelson, T.H. Witney, S.E. Bohndiek, G. Hansson, T. Peitersen, M.H. Lerche, and K.M. Brindle. Production of hyperpolarized [1,4-13c2] malate from [1,4-13c2]fumarate is a marker of cell necrosis and treatment response in tumors. *Proc Natl Acad Sci U S A*, 106(47):19801–6, 2009.

[34] S. Geman and D. Geman. Stochastic relaxation, gibbs distributions, and the bayesian restoration of images. *IEEE Transactions on Pattern Analysis and Machine Intelligence*, 6(6):721–741, 1984.

[35] C. Gnahm, M. Bock, P. Bachert, W. Semmler, N. G. Behl, and A. M. Nagel. Iterative 3D projection reconstruction of (23) Na data with an (1) H MRI constraint. *Magn Reson Med*, Jun 2013.

[36] K. Golman, J.S. Petersen, P. Magnusson, E. Johansson, P. Akeson, C.M. Chai, G. Hansson, and S. Mansson. Cardiac metabolism measured noninvasively by hyperpolarized 13c mri. *Magnetic Resonance medicine*, 59(5):1005–1013, 2008.

[37] K. Golman and S.J. Petersson. Metabolic Imaging and Other Applications of Hyperpolarized 13C1. *Academic Radiology*, 13(8):932–942, August 2006.

[38] K. Golman, R.I. Zandt, M. Lerche, R. Pehrson, and J.H. Ardenkjaer-Larsen. Metabolic imaging by hyperpolarized 13c magnetic resonance imaging for in vivo tumor diagnosis. *Cancer Res*, 66(22):10855–10860, 2006.

[39] I.F. Gorodnitsky and D.R. Bhaskar. Sparse signal reconstruction from limited data using focuss: A re-weighted minimum norm algorithm. *IEEE Trans. Signal Processing*, pages 600–616, 1997.

[40] M. Guerquin-Kern. *Wavelet-Based Reconstruction for Magnetic Resonance Imaging*. EPFL thesis no. 5361 (2012), 137 p., Swiss Federal Institute of Technology Lausanne (EPFL), July 6, 2012.

[41] W.W. Hager and H. Zhang. A survey of nonlinear conjugate gradient methods. *Pacific journal of Optimization*, 2(1):35–58, 2006.

[42] T. Harris, G. Eliyahu, L. Frydman, and H. Degani. Kinetics of hyperpolarized 13C1-pyruvate transport and metabolism in living human breast cancer cells. *Proceedings of the National Academy of Sciences of the United States of America*, 106(43):18131–18136, October 2009.

[43] M.R. Hestenes and E. Stiefel. Methods of Conjugate Gradients for Solving Linear Systems. *Journal of Research of the National Bureau of Standards*, 49:409–436, December 1952.

[44] S. Hu, M. Lustig, A. P. Chen, J. Crane, A. Kerr, D. A. Kelley, R. Hurd, J. Kurhanewicz, S. J. Nelson, J. M. Pauly, and D. B. Vigneron. Compressed sensing for resolution enhancement of hyperpolarized 13C flyback 3D-MRSI. *J. Magn. Reson.*, 192(2):258–264, Jun 2008.

[45] X. Hu, M. Patel, and K. Urbil. A new strategy for spectroscopic imaging. *J Magn Reson B*, 103(1):30–38, Jan 1994.

[46] S. Josan, R. Hurd, J. M. Park, Y. F. Yen, R. Watkins, A. Pfefferbaum, D. Spielman, and D. Mayer. Dynamic metabolic imaging of hyperpolarized [2-(13) C]pyruvate using spiral chemical shift imaging with alternating spectral band excitation. *Magn Reson Med*, Jul 2013.

[47] A.C. Kak, M. Slaney, IEEE Engineering in Medicine, and Biology Society. *Principles of Computerized Tomographic Imaging*. IEEE Engineering in Medicine and Biology Society, 1988.

[48] S. Klein, M. Staring, K. Murphy, M. A. Viergever, and J. P. Pluim. elastix: a toolbox for intensity-based medical image registration. *IEEE Trans Med Imaging*, 29(1):196–205, Jan 2010.

[49] F. Knoll, K. Bredies, T. Pock, and R. Stollberger. Second order total generalized variation (TGV) for MRI. *Magn. Reson. Med.*, 65(2):480–491, 2011.

[50] F. Knoll, C. Clason, K. Bredies, M. Uecker, and R. Stollberger. Parallel imaging with nonlinear reconstruction using variational penalties. *Magn Reson Med*, 67(1):34–41, Jan 2012.

[51] G. Krestin, B. van Beers, C. Blanco, R. abd Cuenod, T. Helbich, P. Parizel, and F.) Sardanelli. Medical imaging in personalised medicine: a white paper of the research committee of the European Society of Radiology (ESR). *Insights Imaging*, 2(6):621–630, Dec 2011.

[52] R. Larson, B.H. Edwards, and D.C. Falvo. *Elementary Linear Algebra*. Houghton Mifflin Harcourt Publishing Company, 2003.

[53] X. Li. Nonlocal Regularized Algebraic Reconstruction Techniques for MRI: An Experimental Study. *Mathematical Problems in Engineering*, 1(1):1–11, May 2013.

[54] Z.P. Liang and P.C. Lauterbur. A generalized series approach to MR spectroscopic imaging. *IEEE Trans Med Imaging*, 10(2):132–137, 1991.

[55] R. Loffler, R. Sauter, H. Kolem, A. Haase, and M. von Kienlin. Localized spectroscopy from anatomically matched compartments: improved sensitivity and localization for cardiac 31P MRS in humans. *J. Magn. Reson.*, 134(2):287–299, Oct 1998.

[56] M. Lustig. Michael Lustig Home Page - SparseMRI V0.2. *http://www.stanford.edu/˜mlustig/*.

[57] M. Lustig, D. Donoho, and J. M. Pauly. Sparse MRI: The application of compressed sensing for rapid MR imaging. *Magn Reson Med*, 58(6):1182–1195, Dec 2007.

[58] M. Lustig, D. L. Donoho, J. M. Santos, and J. M. Pauly. Compressed Sensing MRI. *Signal Processing Magazine, IEEE*, 25(2):72–82, March 2008.

[59] D. Mayer, Y. Yen, A. Takahashi, S. Josan, J. Tropp, B.K. Rutt, R.E. Hurd, D.M. Spielman, and A. Pfefferbaum. Dynamic and high-resolution metabolic imaging of hyperpolarized [1-13c]-pyruvate in the rat brain using a high-performance gradient insert. *Magn Reson Med*, 65(5):1228–33, 2011.

[60] M.I. Menzel, E.V. Farrell, M.A. Janich, O. Khegai, F. Wiesinger, S. Nekolla, A.M. Otto, A. Haase, R.F. Schulte, and M. Schwaiger. Multimodal assessment of in vivo metabolism with hyperpolarized [1-13C]MR spectroscopy and 18F-FDG PET imaging in hepatocellular carcinoma tumor-bearing rats. *J. Nucl. Med.*, 54(7):1113–1119, Jul 2013.

[61] E. Moser, A. Stadlbauer, C. Windischberger, H. Quick, and M. Ladd. Magnetic resonance imaging methodology. *European Journal of Nuclear Medicine and Molecular Imaging*.

[62] M. Neeman, J.M. Provenzale, and M.W. Dewhirst. Magnetic resonance imaging applications in the evaluation of tumor angiogenesis. *Semin Radiat Oncol*, 11(1):70–82, Jan 2001.

[63] J. Oakley, J. Missimer, and G. Szekely. Magnetic resonance imaging based correction and reconstruction of positron emission tomography images. In Edwin R. Hancock and Marcello Pelillo, editors, *EMMCVPR*, volume 1654 of *Lecture Notes in Computer Science*, pages 301–316. Springer, 1999.

[64] C.C. Paige and M.A. Saunders. Lsqr: An algorithm for sparse linear equations and sparse least squares. *ACM Trans. Math. Softw.*, 8(1):43–71, March 1982.

[65] H. Pedersen, S. Kozerke, S. Ringgaard, K. Nehrke, and W. Y. Kim. k-t PCA: temporally constrained k-t BLAST reconstruction using principal component analysis. *Magn Reson Med*, 62(3):706–716, Sep 2009.

[66] H. PerChristian. The truncatedsvd as a method for regularization. *BIT Numerical Mathematics*, 27(4):534–553, 1987.

[67] B.J. Pichler, A. Kolb, T. Nagele, and H.P. Schlemmer. PET/MRI: paving the way for the next generation of clinical multimodality imaging applications. *J. Nucl. Med.*, 51(3):333–336, Mar 2010.

[68] M.D. Plumbley, T. Blumensath, L. Daudet, R. Gribonval, and M.E. Davies. Sparse Representations in Audio and Music: From Coding to Source Separation. *Proceedings of the IEEE*, 98(6):995–1005, June 2010.

[69] M. Poole. Improved Equipment and Techniques for Dynamic Shimming in High Field MRI. *http://itee.uq.edu.au/ uqmpool2/html*$_thesis/$, 2007.

[70] J.M. Provenzale, S. Mukundan, and D.P. Barboriak. Diffusion-weighted and perfusion MR imaging for brain tumor characterization and assessment of treatment response. *Radiology*, 239(3):632–649, Jun 2006.

[71] P.P. Provenzano, C.T. Rueden, S.M. Trier, L. Yan, S.M. Ponik, D.R. Inman, P.J. Keely, and K.W. Eliceiri. Nonlinear optical imaging and spectral-lifetime computational analysis of endogenous and exogenous fluorophores in breast cancer. *J Biomed Opt*, 13(3):031220, 2008.

[72] S.B. Reeder, J.H. Brittain, T.M. Grist, and Y.F. Yen. Least-squares chemical shift separation for (13)C metabolic imaging. 26(4):1145–52+, 2007.

[73] S.B. Reeder, Z. Wen, H. Yu, A.R. Pineda, G.E. Gold, M. Markl, and N.J. Pelc. Multicoil Dixon chemical species separation with an iterative least squares estimation method. *Magn Reson Med*, 51:35–45, 2004.

[74] C. Rischpler, S.G. Nekolla, I. Dregely, and M. Schwaiger. Hybrid PET/MR imaging of the heart: potential, initial experiences, and future prospects. *J. Nucl. Med.*, 54(3):402–415, Mar 2013.

[75] B.D. Ross, P. Bhattacharya, S. Wagner, Tran T., and Sailasuta N. Hyperpolarized MR Imaging: Neurologic Applications of Hyperpolarized Metabolism. *American Journal of Neuroradiology*, 31:24–33, 2010.

[76] L.I. Rudin, S. Osher, and E. Fatemi. Nonlinear Total Variation Based Noise Removal Algorithms. *Physica D*, 60:259–268, 1992.

[77] S. Sarkar, K. Heberlein, and X. Hu. Truncation artifact reduction in spectroscopic imaging using a dual-density spiral k-space trajectory. *Magn Reson Imaging*, 20(10):743–57, 2002.

[78] L.A. Shepp and Y. Vardi. Maximum Likelihood Reconstruction for Emission Tomography. *Medical Imaging, IEEE Transactions on*, 1(2):113–122, October 1982.

[79] G. Shou, L. Xia, and M. Jiang. Total variation regularization in electrocardiographic mapping. In Kang Li, Li Jia, Xin Sun, Minrui Fei, and George W. Irwin, editors, *LSMS/ICSEE*, volume 6330 of *Lecture Notes in Computer Science*, pages 51–59. Springer, 2010.

[80] A. Sigfridsson, K. Weiss, and S. Kozerke. Hybrid proton/carbon constrained image reconstruction for hyperpolarized metabolic imaging. In *Proceedings of ISMRM 2012*, 2012.

[81] S.W. Smith. *The Scientist & Engineer's Guide to Digital Signal Processing*. California Technical Pub, first edition, 1997.

[82] S. Somayajula, A. Rangarajan, and R.M. Leahy. Pet image reconstruction using anatomical information through mutual information based priors: A scale space approach. In *ISBI*, pages 165–168. IEEE, 2007.

[83] P. Storey, R. Otazo, R.P. Lim, S. Kim, L. Fleysher, N. Oesingmann, V.S. Lee, and D.K. Sodickson. Exploiting sparsity to accelerate noncontrast MR angiography in the context of parallel imaging. *Magn Reson Med*, 67(5):1391–1400, May 2012.

[84] B.P. Sutton, D.C. Noll, and J.A. Fessler. Fast, iterative image reconstruction for mri in the presence of field inhomogeneities. *IEEE TRANS. MED. IMAGING*, 22(2):178–188, 2003.

[85] J. Tang, B.M. Tsui, and A. Rahmim. Bayesian pet image reconstruction incorporating anato-functional joint entropy. In *ISBI*, pages 1043–1046. IEEE, 2008.

[86] J. Tsao and P. Boesiger. k-t BLAST and k-t SENSE: dynamic MRI with high frame rate exploiting spatiotemporal correlations. *Magnetic Resonance in Medecine*, 50(5):1031–1042, November 2003.

[87] D.B. Twieg. The k-trajectory formulation of the NMR imaging process with applications in analysis and synthesis of imaging methods. *Med Phys*, 10(5):610–621, 1983.

[88] M. Uecker, T. Hohage, K.T. Block, and J. Frahm. Image reconstruction by regularized nonlinear inversionâJoint estimation of coil sensitivities and image content. *Magn. Reson. Med.*, 60(3):674–682, September 2008.

[89] M. Usman, D. Atkinson, F. Odille, C. Kolbitsch, G. Vaillant, T. Schaeffter, P. G. Batchelor, and C. Prieto. Motion corrected compressed sensing for free-breathing dynamic cardiac MRI. *Magn Reson Med*, 70(2):504–516, Aug 2013.

[90] P. Veit-Haibach, F. P. Kuhn, F. Wiesinger, G. Delso, and G. von Schulthess. PET-MR imaging using a tri-modality PET/CT-MR system with a dedicated shuttle in clinical routine. *MAGMA*, 26(1):25–35, Feb 2013.

[91] Z. Wang. Comparison between two gradient algorithms on a simple 1d energy curve. `http://en.wikipedia.org/wiki/File:Minimizationcomp.JPG`, 2008. Accessed: 2008-03-27.

[92] Z. Wang, Z. Wang, and A.C. Bovik. Why is image quality assessment so difficult? In *in Proc. IEEE Int. Conf. Acoust., Speech, and Signal Processing*, pages 3313–3316, 2002.

[93] K. Weiss, A. Sigfridsson, L. Wissmann, J. Busch, M. Batel, M. Krajewski, M. Ernst, and S. Kozerke. Accelerating hyperpolarized metabolic imaging of the heart by exploiting spatiotemporal correlations. *NMR Biomed*, Apr 2013.

[94] F. Wiesinger, E. Weidl, M.I. Menzel, M.A. Janich, O. Khegai, S.J. Glaser, A. Haase, M. Schwaiger, and R.F. Schulte. Ideal spiral csi for dynamic metabolic mr imaging of hyperpolarized [1-(13) c]pyruvate. *Magn Reson Med*, 2011.

[95] J.P. Wijnen, J.J. van Asten, D.W. Klomp, T.E. Sjobakk, I.S. Gribbestad, T.W. Scheenen, and A. Heerschap. Short echo time 1H MRSI of the human brain at 3T with adiabatic slice-selective refocusing pulses; reproducibility and variance in a dual center setting. *J Magn Reson Imaging*, 31(1):61–70, Jan 2010.

[96] Y. Wu, Y.J. Zhu, Q.Y. Tang, C. Zou, W. Liu, R.B. Dai, X. Liu, E.X. Wu, L. Ying, and D. Liang. Accelerated MR diffusion tensor imaging using distributed compressed sensing. *Magn Reson Med*, Mar 2013.

[97] J. Yang, J. Wright, Y. Ma, and T. Huang. Image Super-Resolution as Sparse Representation of Raw Image Patches. *IEEE Conference on Computer Vision and Pattern Recognition (CVPR), 2008*.

[98] Y. Yen, S.J. Kohler, A.P. Chen, J. Tropp, R. Bok, J. Wolber, M.J. Albers, K.A. Gram, M.L. Zierhut, I. Park, V. Zhang, S. Hu, S.J. Nelson, D.B. Vigneron, J. Kurhanewicz, H.A.A.M. Dirven, and R.E. Hurd. Imaging considerations for in vivo 13c metabolic mapping using hyperpolarized 13c-pyruvate. *Magn Reson Med*, 62(1):1–10, 2009.

[99] L. Ying, D. Xu, and Z. P. Liang. On Tikhonov regularization for image reconstruction in parallel MRI. *Conf Proc IEEE Eng Med Biol Soc*, 2:1056–1059, 2004.

[100] Y.X. Yuan. Trust region algorithms for constrained optimization. *Math. Prog*, 47:53–63, 1990.

[101] H. Zhang, Y. Zhang, and T.S. Huang. Exploiting structured sparsity for image deblurring. In *Proceedings of the 2012 IEEE International Conference on Multimedia and Expo*, ICME '12, pages 616–621, Washington, DC, USA, 2012. IEEE Computer Society.

[102] M.L. Zierhut, Y.F. Yen, A.P. Chen, R. Bok, M.J. Albers, V. Zhang, J. Tropp, I. Park, D.B. Vigneron, J. Kurhanewicz, R.E. Hurd, and S.J. Nelson. Kinetic modeling of hyperpolarized 13C1-pyruvate metabolism in normal rats and TRAMP mice. *J. Magn. Reson.*, 202(1):85–92, Jan 2010.